UNIL | Université de Lausanne
Faculté des géosciences
et de l'environnement

Evaluation of the potential for seismic investigation of subglacial bed conditions and near-surface ice properties for an Alpine temperate glacier

Boris Ouvry

Director : Prof. Dr. Stuart Lane

Co-director : Dr. James Irving

Expert : Dr. Ludovic Baron

Cover picture
Otemma Glacier

View since a drone flight near the site 10
Boris Ouvry - August 19, 2019

Evaluation of the potential for seismic investigation of subglacial bed conditions and near-surface ice properties for an Alpine temperate glacier

Boris OUVRY
Under the direction of
Prof. Dr. Stuart N. LANE
and with as co-director
Dr. James Irving

Faculty of Geosciences and Environmental Sciences
University of Lausanne

Abstract

The active seismic method offers a recognized, efficient, and constantly developing potential for investigation in glaciology. The objective of this work is to investigate and understand subglacial and supraglacial processes that might impact the dynamics of an Alpine temperate glacier, Glacier d'Otemma, located in the Val de Bagne, Switzerland, using of an Electrodynamic Vibrator System, ElViS. The sledgehammer is proposed as a comparative and alternative source. A P-wave analysis is considered in order to determine the extent and quality of the till at the glacier bed, via seismic reflection, as well as to determine the influence of ice properties on the P-waves propagation velocity at the glacier near-surface, via seismic refraction. The results of the reflection experiment, although promising, did not meet the desired objectives. This is probably due to the ice properties of the ablation zone of this Alpine temperate glacier, the period for which the measurements were made and the supra- and subglacial meltwater influence which favoured the presence of persistent noise during processing. However, the sledgehammer seismic profile observations showed satisfactory refraction wave quality and thus allowed a travel time tomographic inversion to study the near-surface of the glacier. The results obtained showed two-layered system of P-wave propagation velocities, in the first five metres layers of the near-surface. The hypothesis that the ice properties of the near surface could justify these variations in velocity between these two layers could therefore be verified. We therefore concluded that the ice properties, in the ablation zone of an Alpine temperate glacier, have an impact on the P-wave propagation velocity at the near surface, during the melting period. This conclusion also justifies how the ice properties may have interacted with the measurements and influenced the reflection data. Finally, ElViS is probably not a suitable source for supra- and sub-glacial seismic exploration in the ablation zone of an Alpine temperate glacier. It does not allow to determine the transport mechanisms of sub-glacial sediments, that influence the structural evolution of the sub-glacial drainage system, during the melting period.

Évaluation du potentiel d'investigation sismique des conditions du lit sous-glaciaire et des propriétés de la glace à la surface d'un glacier tempéré alpin

Boris OUVRY
Sous la direction de
Prof. Dr. Stuart N. LANE
et avec comme co-directeur
Dr. James Irving

Faculté des Géosciences et Sciences de l'Environnement
Université de Lausanne

Résumé

La méthode sismique active offre un potentiel reconnu, efficace et en développement constant dans l'investigation glaciologique. L'objectif de ce travail est d'étudier et de comprendre les processus supra- et sous-glaciaires qui pourraient avoir un impact sur la dynamique d'un glacier tempéré alpin, le Glacier d'Otemma, situé dans le Val de Bagne, en Suisse, en utilisant un système de vibration électrodynamique, ElViS. Le sledgehammer est proposé comme source comparative et alternative. Une analyse de l'onde P est effectuée afin de déterminer l'étendue et la qualité du till au lit du glacier, par la réflexion sismique, ainsi que pour déterminer les propriétés de la glace à la surface du glacier, par la réfraction sismique. Les résultats de l'expérience de réflexion, bien que prometteurs, n'ont pas atteint les objectifs souhaités. Cela est probablement dû aux propriétés de la glace de la zone d'ablation de ce glacier tempéré, à la période pour laquelle les mesures ont été effectuées et à l'influence des eaux de fonte supra et sous-glaciaires qui ont favorisé la présence d'un bruit persistant pendant le traitement. Cependant, les observations du profil sismique au sledgehammer ont démontré une qualité satisfaisante des ondes de réfraction et ont donc permis une étude par tomographie à ondes P à la surface du glacier. Les résultats obtenus ont montré un système à deux couches de vitesses de propagation des ondes-P, dans les cinq premiers mètres de la surface du glacier. L'hypothèse que les propriétés de la glace de la surface du glacier pourraient justifier ces variations de vitesses, entre ces deux couches, a donc pu être vérifiée. Nous avons donc conclu que les propriétés de la glace, pour la zone d'ablation d'un glacier tempéré alpin, ont un impact sur la vitesse de propagation de l'onde-P à la surface du glacier, pendant la période de fonte. Cette conclusion permet également de justifier en quoi les propriétés de la glace ont pu interagir avec les mesures effectués et influencer les données de réflexion. Enfin, l'ElViS n'est probablement pas une source appropriée pour la prospection sismique supra- et sous-glaciaire, sur la zone d'ablation d'un glacier tempéré alpin. Il ne permet pas de déterminer les mécanismes de transport des sédiments sous-glaciaires, qui influencent l'évolution structurelle du système de drainage sous-glaciaire, pendant la période de fonte.

Acknowledgements

Table of contents

List of figures

List of tables

Introduction and background

Introduction and background
First tests

View of Petit Mont-Collon (3555 m.a.s.l.) from the site 2. Sites 1 and 2 were mainly used as test sites for the implementation of the cross spread.
Thomas Tscharner - July 19, 2019

1. Introduction

Sediment input from glaciers is linked to complex process interactions involving ice flux, basal erosion, and sediment transfer to subglacial and proglacial streams (Perolo et al., 2019). Glacier surface velocities can show a dynamic response to increasing air temperature, particularly during melting periods, when meltwater from the surface reaches the ice/bed interface, causing high subglacial water pressures, lubricating the glacier bed, which will improve the basal movement, and accentuate the retreat of the glacier (Clason et al., 2012). This phenomenon is leading to an increase in meltwater input from subglacial channels, thus increasing sediment transport capacities and making sediments more dependent on sediment availability (Lane et al., 2017). These sediments influence mountain streams and can lead to a decrease in hydroelectric power generation, sediment accumulation in dam retention basins or in water intakes, or modifications, positive and negative, of the morphology and ecology of mountain streams and river valleys (Gabbud & Lane, 2016). The climate change influence, particularly permafrost melting and glacier retreat, could accelerate sediment deposition in valleys (Buteau et al., ,in ways that, whilst uncertain, may accelerate (Lane et al., 2017). Subglacial erosion is known to be a primary sediment source, but it is difficult to say whether or not this till can be removed from the subglacial system (Herman et al., 2015).

Boundaries between bedrock, deformable till and the rigid part of the glacier are not easily definable, but their interactions influence shear stress at the glacier bed (Thorsteinsson & Raymond, 2000). Slipping at this interface, between till and ice, is the dominant mechanism of basal movement, thus regulating the ice deformation rate (Truffer et al., 2001). The plasticity of subglacial material influences basal movement of glaciers and is explained by variations, sometimes significant, in the movement rate of the glacier. Considering that the shear strength of the till does not depend on the deformation rate, but rather increases linearly with effective pressure, pseudo-viscous shear strength can be caused by the expansion of consolidated till (Iverson, 2010). This can result in a decrease in pore pressure in subglacial networks and therefore a decrease in flow during the slip. Shear resistance on a bed with easily erodible and viscous till are processes rooted in subglacial hydrology. However, two interesting studies question some approaches to the relationship between shear strength and till deformation. Turrin et al. (2013) show that *pulses*, "a type of unstable ice flow intermediate between normal flow and surging", can occur and seem to be related to the deformation of the subglacial till. The cyclical nature of these *pulses* has been interpreted as being due to a porous till layer, which does not drain sufficiently between the *pulses*. This meltwater recharge in the till also increases its expansion, and thus its ability to deform. Halberstadt et al. (2018) point to simultaneous processes, rather than deformation and/or till deposition, acting at the glacier bed level. According to their research, the porous spaces of the till, water saturated, would lead to a basal shift by piping the meltwater and not by deforming the till. With these observations, this study challenges the hypothesis that low shear strength is systematically associated with high till deformation. It is true that Halberstadt et al. (2018) is conducted on the Antarctic continental shelf, but this is in contradiction to Turrin et al. (2013), who studied the Ruth Glacier, Alaska.

The presence of till on the bed can be a reliable indicator of a situation where sediment supply (from upstream or from local erosion) is greater than the local capacity of subglacial discharges to evacuate that sediment (Truffer et al., 2001). Till also represents a "cover effect", so reducing the extent to which a glacier is able to erode its bed as long as till is present. If the till is deformable, it is therefore more brittle and easily transportable and will feed into glacier sliding and hence erosion, (a "tool" effect) unlike a more rigid till. It is for these reasons that it is interesting to know whether and what kind of till is present at the bed. In addition, knowing the ice properties of the glacier near-surface could allow a better understanding of the supraglacial dynamics of the ablation zone, and finally the evaluation of the impact of surface meltwater on the glacial and subglacial hydraulic processes of temperate glaciers.

Seismometry applications in glaciology have led to major advances in the understanding of fundamental processes related to the cryosphere, by increasing our knowledge of the physical structure of ice masses, supraglacial and subglacial hydrology, basal movements, and glacier dynamics (Podolskiy & Walter, 2016). The potential of the active seismic method will be evaluated, in particular the reflective and refractive seismic method, in seismic prospecting of an Alpine temperate glacier. This work is an experimental study in the active seismics field, in order to estimate the presence of till on the glacier bed and the near-surface ice properties, and to improve understanding of the sub- and supraglacial dynamics of Alpine temperate glaciers. This Master thesis has two primary objectives: (1) analysis of the glacier bed by studying the extent and quality of the till cover at the bedrock surface and (2) analysis of the influence of ice properties on the P-waves propagation velocity at the glacier near-surface. The articles studied generally refer to explosives as a seismic source. However, logistics, legislation, and supply, as well as associated risks made this solution inappropriate. Measurements on the Glacier d'Otemma were carried out by means of a small vibroseis: the Electrodynamic Vibrator System (ElViS) and following from these objectives, a third considers the potential contribution of ElViS for active seismic surveys on a temperate glacier. This memoire proposes three hypotheses: (1) the active seismic method, using ElViS, could allow the analysis of till in the subglacial bed, and the near-surface ice properties of the ablation zone; (2) the reflection seismic method allows quantification of the influence of the subglacial sediment transport mechanisms in the structure evolution of the subglacial drainage system, during the melting period; and (3) the refractive seismic method allows identification of a layers system, with variable P-wave propagation velocities, making it possible to highlight the influence of ice properties on P-wave propagation on the glacier near-surface, and therefore, meltwater flows impact on the supraglacial dynamics.

2. Background

The background study will include literary references on previous studies, history and current information related to this work, through four topics: (1) the history of seismic methods, studies that have contributed to its evolution over time and the development of active seismic methods; (2) the methodological principles related to active seismic methods and more specifically to seismic reflection and refraction; (3) the ice crystal properties that influence the glaciological environment; and (4) the supraglacial ice properties in terms of structure and meltwater influences on the glacier surface.

2.1. The seismic method in glaciology

2.1.1. Seismic method history

Seismic wave propagation within the Earth has been studied by many scientists since the early 1900s (e.g., Knott, 1899, 1920; Wiechert, 1920; Jeffreys, 1926; Bouasse, 1927; Sieberg & Gutenberg, 1923; Gutenberg et al., 1932; Gutenberg & Richter, 1939; Dana & Salisbury, 1944). In 1917, L. Mintrop, a German scientist, used the seismic refraction method, which he finally patented during the First World War, to locate the position of heavy pieces of artillery using a portable field seismograph (Hübscher & Gohl, 2014). In 1919, the seismic refraction method became commercial and was used to locate salt domes in northern Germany. In 1921, Canadian engineer, R. Fessenden, developed a sound imaging system, the ancestor of Sound Navigation and Ranging (Sonar) to find icebergs to secure crossings in the North Atlantic (Roden, 2005; Hübscher & Gohl, 2014). The expansion of land-based seismic exploration began during the 1929 economic crisis, with an increase in oil prices, prompting entrepreneurs to invest in the search for oil deposits on Texas soil (Dragoset, 2005; Hübscher & Gohl, 2014).

One of the first seismic measurements for scientific purposes was made in the Whale Bay area during the Antarctic Byrd expedition from 1933 to 1935 (Robin, 1953). The objective of these measurements was to determine the ice thickness present in this region. Estimates varied from a hundred to a few thousand metres and the interpretations seemed uncertain. An expedition led by the Norwegian-Swedish-British Council to Antarctica, between 1949 and 1952, took over these thickness measurements, which were ultimately more conclusive (Robin, 1953). The desire to detect geological origin of structural shapes on the glacier bed followed in the mid-1950s. Between 1956 and 1957, during a Canadian expedition to the Salmon Glacier, British Columbia, a research group used seismic measurements to determine the form of the glacier bed (Doell, 1962). The use of a dozen high-resolution geophone lines, during this expedition, allowed major advances in the reception, calculation and understanding of P-wave velocities. The results were partial, but it was found that the glacier bed was V-shaped, like a narrow valley. The use of seismic method, and more specifically P-wave velocity analysis, permitted definition of the influence of temperature on seismic waves in ice (Thyssen, 1968; Kohnen, 1974), detection of glacier movement (VanWormer & Berg, 1973) and estimation of variations in ice density (Kirchner, 1979).

2.1.2. Active seismic studies

Active seismic methods in glaciology provide solid results in investigating a glacier's structural properties. Early studies using this method focused on measurements of ice thickness and wave propagation rates in temperate (Röthlisberger, 1955) and polar (Hobson, 1962; Kohnen & Bentley, 1973) glacier ice. These studies also aimed to find relationships between wave velocity and glacier depth, as well as between wave velocity and glacier orientation, but without any concrete results. Comparisons with data from 1958, at another Byrd glacier station site, Antarctica, had shown that the propagation rates were too high and inconsistent. This was probably due to a difference in ice formation resulting from a difference in snow/firn accumulation speed between these two sites. Studies related to seismic reflection techniques have also been undertaken to understand the interactions between the glacier bed, the presence of subglacial water in the shear stress, as well as mechanical strength processes at glacier beds. Richards (1988) compared P-waves from the deepest part of Variegated Glacier's bed with the shallowest ones during a surge between 1982 and 1983. P-wave phase inversion disrupted the observations, probably due to a fluidized debris layer during the glacier surge, which acted as a seismic wave absorber, thus biasing the results. Nolan & Echelmeyer (1999) demonstrated the feasibility of measuring changes at the base of Black Rapids Glacier, Alaska, on hourly time scales, to demonstrate the correlation between subglacial drainage of supraglacial marginal lakes and increases in glacier basal motion. According to numerous articles on the subject (Röthlisberger, 1955; Bose et al., 1971; Kohnen & Bentley, 1973; Richards, 1988; Nolan et al., 1999; King et al. 2008; Hilbich et al., 2010; Kim et al. 2010; Scapozza et al., 2011; Zechmann et al. 2018 and Church et al. 2019), the P-wave velocities in ice is estimated to range from 3100 to 4500 m/s (Fig. 1).
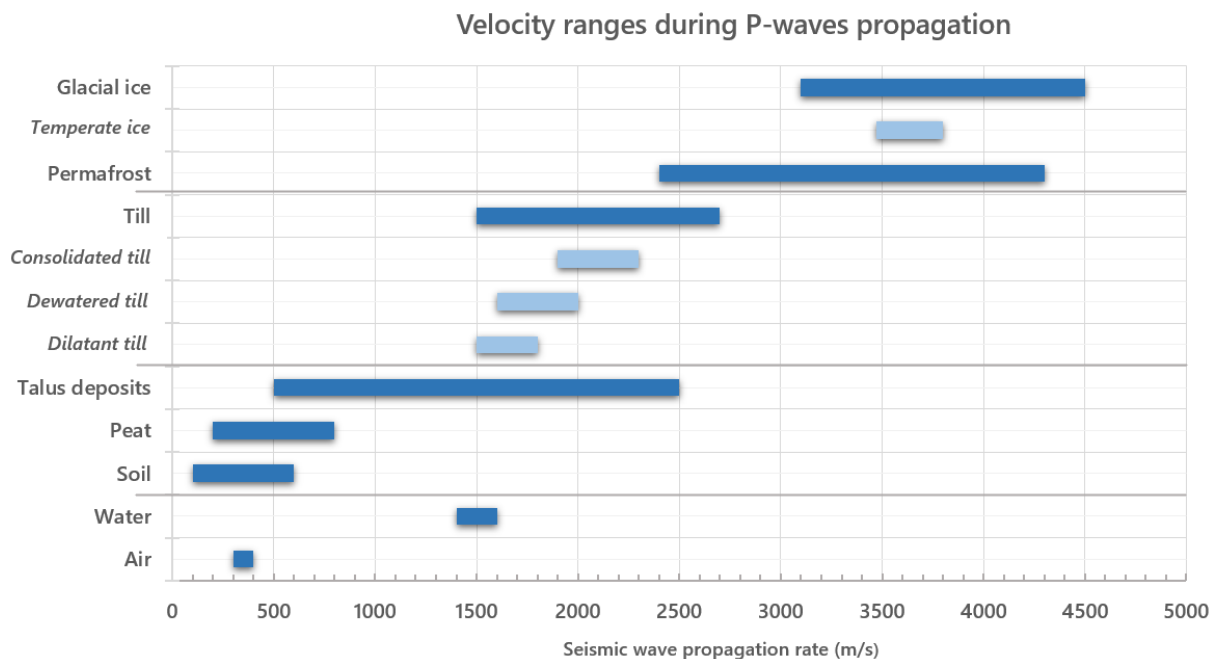
Figure 1. *Velocity ranges during P-waves propagation*
The values of P-wave propagation velocities (m/s), for different type of materials.
Source: *Bose et al., 1971; Kohnen & Bentley, 1973; Richards, 1988; Nolan et al., 1999; King et al. 2008; Hilbich et al., 2010; Kim al. 2010; Scapozza et al., 2011; Christianson et al., 2014; Hofstede et al., 2018; Zechmann et al. 2018 and Church et al. 2019.*

Are & Bentley (1993) studied the P-wave reflection phase at the glacier ice base, on the Ross Ice Shelf's temperate glaciers, West Antarctic, and proposed a propagation velocity in the ice estimated at 3630 ± 30 m/s. King et al. (2008) characterized the glacier bed state and the physical properties of the material beneath, by comparing the measured reflection coefficient and the energy emitted by the primary and multiple reflections, at the beds of polythermal glaciers, in Svalbard. They determined the acoustic impedance of glacier bed materials as $6.78\pm1.53\cdot10^6$ kg·m^{-2}·s^{-1} and estimated ice P-wave velocities of 3750 ± 50 m/s, for a 915 ± 5 kg·m^{-3} ice density. Kim et al. (2010) carried out seismic surveys on the Fourcade Glacier (a polythermal glacier), on King George Island, Antarctica, to estimate the P-wave average velocity in ice of 3466 m/s with a 920 kg·m^{-3} wet ice density, between 5.1% to 3.2% water content, as well as a 6.925 GPa and 3.119 GPa ice incompressibility and rigidity. For temperate glaciers, P-wave velocities between 3470 m/s to 3740 m/s (Kim et al., 2010; Christianson et al., 2014; Hofstede et al., 2018), up to 3795 m/s (Paterson, 1981; Cuffey and Paterson, 2010; Bradford et al., 2013) have been observed.

Methodological advances and knowledge of the seismic wave propagation mechanism through glaciers have led many researchers to investigate more closely glacier thickness and bedrock composition. The use of a vibroseis in glaciological studies is mainly concentrated in polar glaciers. Studies have focused mainly on truck-mounted vibroseis, travelling through certain areas in Antarctica and Greenland, in order to analyse subglacial geology, ice-shelf cavity and sea-bed strata (Eiken et al., 1989; Eisen et al., 2010, 2015). The use of an ElViS on glaciers is referenced in three studies: (1) Diez et al. (2013), (2) Polom et al. (2014) and (3) Smith et al. (in press). These two first studies were carried out at Colle Gnifetti (4554 m.a.s.l.), on the Italian side of Monte Rosa. In this study area, the physical properties of ice are comparable to polar conditions. Diez et al. (2013) focused mainly on a comparison between an explosive source and a vibrating source, as well as ice properties in the field. The vibroseis technique produced coherent reflective waves and provided relevant information on ice stratigraphy, density, and Crystal-Oriented Fabric (COF). Polom et al. (2014) obtained similar results and conclusions to Diez et al. (2013), highlighting that this method could provide new knowledge on the internal structure of ice masses and open a promising new investigation method for subglacial structures and their properties, such as basal sediments. However, they highlight the difficulties encountered, the errors discovered and certain inconsistencies results, but also the probable causes of these flaws. A recent study by Smith et al. (in press), on the Kongsvegen (a polythermal glacier), Svalbard, was recently presented at European Geosciences Union (EGU) 2020. These studies sought to verify ElViS reliability in seismic surveys of polar and polythermal glaciers, to detect the bed and/or subglacial forms. Their results were a success and brought more confidence in the feasibility of such a methodology in our study.

2.2. Principles of the active seismic method

2.2.1 Overview

A cross-measurement technique, *cross-spread*, was used during field measurements (Fig. 2). A seismic source located on the glacier surface emits seismic waves that propagate through the glacier. These are

reflected back towards the surface or refracted at locations across which the seismic impedance of the ice changes (e.g., bedrock interface). The reflected and refracted waves are then eventually detected by geophones on the glacier surface, where they are digitized and recorded by an acquisition computer for subsequent processing.
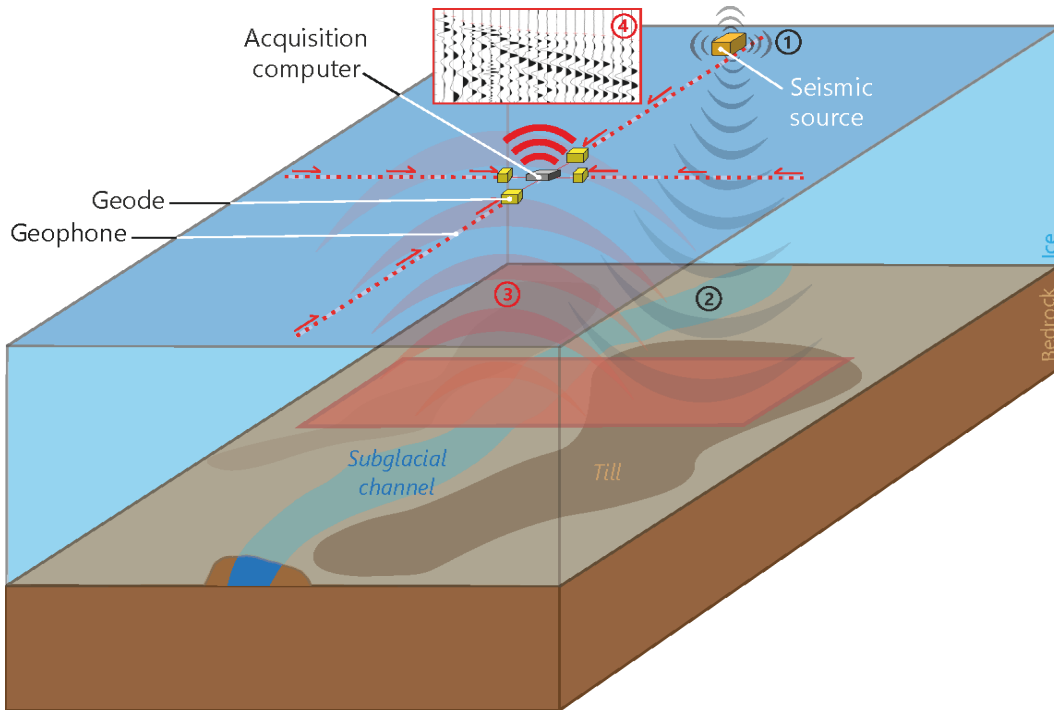
Figure 2. *Diagram of active seismic methodology*
(1) A seismic source located on the glacier surface emits seismic waves that (2) propagate through the glacier; (3) These are reflected back towards the surface or refracted at locations across which the seismic impedance of the ice changes; (4) The reflected and refracted waves are then eventually detected by geophones on the glacier surface, where they are digitized and recorded by an acquisition computer for subsequent processing.

2.2.2. Seismic reflection and refraction

Seismic reflection and refraction (Fig. 3) record the propagation of elastic waves front along a profile equipped with geophones (Bitri et al., 1996). When a seismic P-wave arrives at a subsurface interface, part of the wave energy will be transmitted, and part will be reflected back towards the surface. The seismic reflection is based on two fundamental principles: (1) the wave propagates in the same medium and incidence plane, and (2) at an incidence angle θ_i, relative to *normal* at the impact point on a surface, where the wave is reflected (in absolute terms) at a reflection angle θ_{re}. The normal incidence reflection coefficient k is defined as the ratio between the reflected wave amplitude A_{re} and the incidence wave amplitude A_i, given by (1; Bitri et al., 1996):

$$k = \frac{A_{re}}{A_i} = \frac{Z_2 - Z_1}{Z_2 + Z_1}, \tag{1}$$

where Z_1 is the acoustic impedance (product of P-wave velocity and density), in the upper *medium 1*, and Z_2 is the acoustic impedance in the lower *medium 2*. Till and bedrock have different acoustic impedances which may allow distinguishing these regions based on the reflected wave characteristics.

For seismic refraction, when the seismic impedance changes, the refracted wave propagates at a different velocity and at a refraction angle θ_{ra}. The repartition of this energy depends on the contrast in acoustic impedance at the interface (Fig. 4). Note that the reflection coefficient can be positive or negative and depends on the relative impedance values on either side of the interface under investigation (Bitri et al., 1996; Mari, 2002).
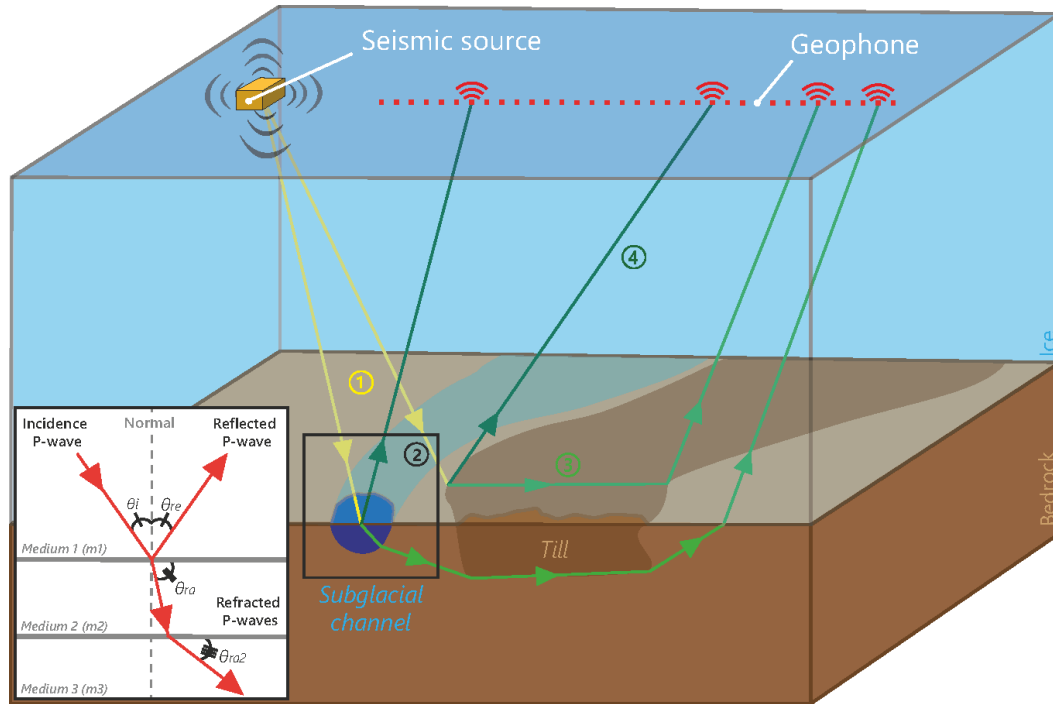
Figure 3. **P-waves reflection and refraction**
(1) The wave propagates in the same medium m1 and incidence plane, and (2) at an incidence angle θ_i, relative to normal at the impact point on a surface, where the wave is reflected (in absolute terms) at a reflection angle θ_{re}. When a seismic P-wave arrives at a subsurface interface, (3) a part is refracted and is propagated at a different velocity, as well as a refraction angle θ_{ra}, and (4) a part is reflected back towards the surface.
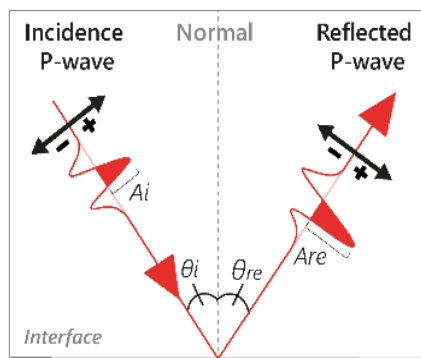
Figure 4. **Amplitude of reflection**
Representation of P-wave reflection, in terms of amplitude, represents reflected A_{re} P-wave amplitude when an incident P-wave A_i contacts an interface separating two different acoustic impedances mediums. Reflection coefficients at positive (+) and negative (-) signal are represented by the incidence angle θ_i, the reflection angle θ_{re}.
Source: *Bitri et al., 1996.*

Reflectivity also varies with angle and can sometimes be used to obtain information on seismic properties, on either side of an interface, by evaluating the reflected amplitudes and comparing them to the angle of incidence (Zechmann et al., 2018). Zechmann et al. (2018) proposed strategies and limitations in the active seismic method and defined series of diagnostic curves, relative to the AVA, comparing the reflectivity and the angle of incidence (Fig. 5). They listed the main reference values for the analysis of the seismic reflection velocities in relation to subglacial sedimentology (Tab. 1). For these reference values (Tab. 1), the velocity of the compressional waves α depends on the strength of the sediment and its water content. The shear wave velocity β also depends on the sediment strength and is more sensitive to water content than α. Finally, the sediment density ρ is also a good indicator of the water content of till.
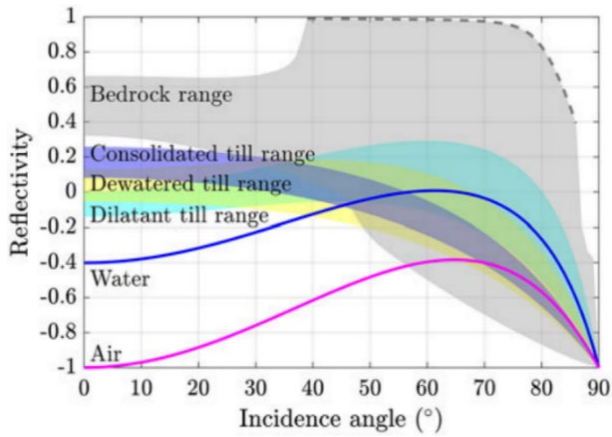
Figure 5. Reflectivity curves for interfaces between glacier ice and various materials
Seismic parameters used to produce the ranges for till are listed in Table 1.
Source: *Zechmann et al., 2018.*

Zechmann et al. (2018) proposed methodological alternatives, by changes in some of reference variables (4), to bedrock investigation relative to the AVA: (1) an inverting for source amplitude, which consists performing AVA without the bed reflection multiple; (2) a reflectivity crossing angle analysis (Fig. 5); (3) a characterization of till parameters combinations α, β and ρ in the AVA analysis (Tab. 1); and (4) an acoustic impedance which would result in the search for significant results between the parameters α, β and ρ, expressed as acoustic impedance Z compared to the parameters β (Z would be equal to αρ).

AVA/AVO methods are widely used in hydrocarbon reservoir characterisation (Anwer et al., 2017). The only practical difference between these two methods lies mainly in the seismic analysis. AVO analysis is performed on offset clusters or partial offset stacks, and AVA analysis on angle clusters or partial angle stacks. Seismic amplitude analysis of

Table 1. Values used to produce the curves in Figure 5
Established by the studies carried out by Morgan, 1969; Hamilton, 1976; Clarke et al., 2008; Christianson et al., 2014. Reference seismic parameters for this work.
Source: *Zechmann et al., 2018.*

Material	α (m·s⁻¹)	β (m/s⁻¹)	ρ (kg/m⁻³)
Dilatant till	1500-1800	0-500	1700-2000
Dewatered till	1600-2000	400-1100	1900-2200
Consolidated till	1900-2300	1000-1200	2100-2500

reflected waves could therefore be used to determine subglacial material properties. In glaciology, AVA would make it possible to distinguish rigid tills from deformable tills, according to models applies to field measurements (Anandakrishnan, 2003; Zechmann et al., 2018). The recorded amplitude is then a function of the incidence angle and the elastic properties of the interface separating the two investigated media, i.e. the seismic wave density and velocity ratio (Church et al., 2019). In theory, AVA analysis could allow the presence or absence of till on the bedrock to be distinguished, over a specifically measured area, and perhaps even to differentiate the quality of the till in terms of permeability and plasticity.

2.2.3.   Seismic wave propagation

Elastic media, such as glaciers, are assumed to be isotropic, although anisotropic glacier ice has previously been observed in seismic studies (Robertson & Bentley, 1990; Horgan et al., 2008; Hofstede et al., 2013; Diez et al., 2014). Taking into consideration that the shear or rigidity modulus μ is given by (2; Schlegel et al., 2019):

$$\mu = V_s{}^2 \rho, \tag{2}$$

where ρ is density and V_s corresponds to the phase velocity of the S-wave, as well as the bulk modulus κ, we then obtain the velocity of propagation of the P-wave V_p (3; Schlegel et al., 2019):

$$V_p = \sqrt{(\kappa + \frac{4}{3}\mu)/\rho}. \tag{3}$$

The mass modulus κ represents the proportionality relationship between the pressure and the rate of change in the volume of a medium (McNaught, 1997). It is sensitive to the compressibility of fluids, making P-waves dependent on the fluid content of a medium (Xie, 2015). This dependence, together with the shear modulus μ, which is used to measure the stiffness of materials (i.e. the ratio of shear stress to shear strain), allows P-waves to propagate in solids and liquids (McNaught, 1997).

2.3. Ice crystal properties

The physics of ice crystals and their behaviour are greatly influenced by the glaciological environment. Rigsby (1960) was one of the first to study ice deformation and recrystallization in the laboratory. He compared the optical axes of ice crystals between polar and temperate glaciers and found that the optical axes were generally perpendicular to the foliation planes (alternating air bubbles and clear ice plane structures) for polar glaciers, highlighting an orderly crystal arrangement. The crystal optical axes for temperate glaciers formed three or four maxima with respect to the foliation planes, making the all the crystals whole disorganised. This experiment showed that after crystal deformation and then melting (in the laboratory), large crystals recrystallised into many smaller ones, while fine-grained ice recrystallised into a few large crystals with different orientations. Raymond & Harrison (1975) showed that glacier polycrystalline ice, when it is at the melting point, can be considered as a two-phase aqueous mixture that can be located (1) within the crystal interstices and (2) at the boundaries of grain channels. These liquid water flows strongly influence the plastic deformation rate of crystals at the microscopic scale (Duval, 1977; 1979). However, plastic deformation of other polycrystalline systems can greatly limit liquid water flows (Duval et al., 1983).

2.4. Supraglacial ice properties

A glacier surface is naturally sensitive to air temperature, and more specifically to the surface energy heat flux F, supply of energy for ice melt Q_m and a heat flux on the glacier surface G, expressed by the following equation (4; Machguth et al., 2006; Sicart et al., 2008) :

$$F = Q_m + G = S_{in} - S_{out} + L_{in} - L_{out} + Q_h + Q_l \qquad (4)$$

Surface energy heat flux F depends on six main phenomena: (1) incoming shortwave radiation S_{in}, related to the sunshine; (2) outgoing shortwave radiation S_{out}, related to the albedo; (3) incoming longwave radiation L_{in} subtracted from (4) outgoing longwave radiation L_{out}, related to the cloudiness (i.e. air temperature and humidity), favouring the presence (if clear) or absence (if covered) of frost on the glacier surface; (5) the sensible heat flux Q_h, as a function of the temperature gradient and wind speed; and (6) the latent heat flux Q_l, as a function of the vapour pressure gradient and also wind speed. All of these phenomena greatly influence the ice surface and, during the melting period, could make field measurements ineffective or even exhausting. There are three other factors that must be taken into account in order to complete the energy balance of the glacier surface: (1) the heat supplied by rain, (2) the precipitation in snow form and (3) the snow accumulation or removal due to wind or avalanches (Machguth et al., 2006; Sicart et al., 2008).

Porous *weathering crustal* ice layers, which represent the shallow porous layer (typically 0.01 to 2 m) of glacier surfaces develop as a function of three factors (Stevens et al., 2018): (1) subsurface melting caused by incident solar radiation, (2) heat flow in interstitial spaces which decreases ice crystal cohesion and (3) the kinetic energy, caused by heat transfer, which is related to the water friction through the interstitial flow pathways. Cooper et al. (2017), over an ablation zone near Kangerlussuaq, on the southwest Greenland Ice Sheet, determined using piezometers that water-saturated ice remained to a depth of at least 1.1 m below the ice sheet surface. Ice density data from ice cores, at depths between 0.9 and 1.1 m, suggested a 15 to 22 cm average of liquid meltwater storage in this low-density ice (between 474 and 725 kg m^{-3}).

The presence of pools of water and glacial channels on the ice surface in the ablation zone indicates a relative ice impermeability (Fountain & Walder, 1998). Ice permeability is related to meltwater transport, during the melting season, in the veins along grain boundaries, which are enlarged by solar radiation. This process is limited to a few tens centimetres at the surface, due to limited shortwave solar radiation penetration (Brandt & Warren, 1993). Young et al. (2010), during seismic prospecting at the Fourcade Glacier, showed that the lowest values of P-wave propagation velocity were observed between the glacier surface and down to about 20 m depth indicating warmer ice at this surface level, probably caused by surface melting during the summer season. Similar observations had also been made on the Johnson Glacier (temperate and polythermal glacier), on Livingston Island, Antarctica, for the first 2.5 metres of the glacier surface (Benjumea et al., 2003). This study had shown that near-surface conditions have a strong influence on the elastic and electromagnetic waves propagation, reducing the accuracy of velocity measurements and estimates of ice water content.

Tsanfleuron Glacier observations, using a GPR and drilling video cameras, revealed the presence of small channels, voids and cracks through different layers at the glacier depth, allowing infiltration by capillarisation (Pohjola, 1994; Murray et al., 2000; Fountain et al., 2005). The radar wave velocities passing through ice are not only conditioned by intracrystalline water, on a microscopic scale, but also by larger water bodies, from a few centimetres to a few decimetre (Murray et al., 2000, 2007; Gusmeroli et al., 2008). A fairly marked variation in radar and seismic wave propagation velocities has been observed in the first five metres of the surface of temperate glaciers. Refraction tomography was carried out and allowed ice properties interpretations in the top five metres of the upper part on the Falljökull ablation zone, Iceland (Murray et al., 2000, 2007). The velocity propagation varies greatly depending on the proportion of pores filled with air and water (Murray et al., 2007). Wet, water-saturated ice layers remained in air-rich ice.

Methodology and field measurements

3. Methodology

This work seeks evaluates ElViS as a tool for studying Alpine temperate glaciers. Our experimentation is based on the comparison of the vibroseis with the sledgehammer. The seismic reflection method, via AVA, was carried out to allow the analysis of subglacial materials. The seismic refraction method, via the travel time tomographic inversion, was also carried out to study the P-wave propagation velocity at the near-surface. Below we discuss: (1) the study area, (2) our measurement technique, with the different equipment used and protocol implemented in the field, and (3) the reflection and refraction processing.

3.1. Study area

The study area (Fig. 6) is located in the ablation zone of the Glacier d'Otemma, in the Val de Bagnes, Valais Alps, Switzerland. This glacier has very intense subglacial hydrological activity during melting periods and is the subject of much research (Gabbi et al., 2012; Sala, 2019; Egli et al., 2020). In summer 2019, the glacier front was located at around 2511 m.a.s.l. with a prominent front that is difficult to access, linked to an ice surface subsidence over a subglacial cavity, making the logistics of this work complex. In 2009, the Glacier d'Otemma had an area of 15.74 km^2 (Gabbi et al., 2012). An approximation of the current glacier surface area was carried out manually via old maps, ground measurements and aerial photographs, as well as satellite images on © Swisstopo (App. 1).
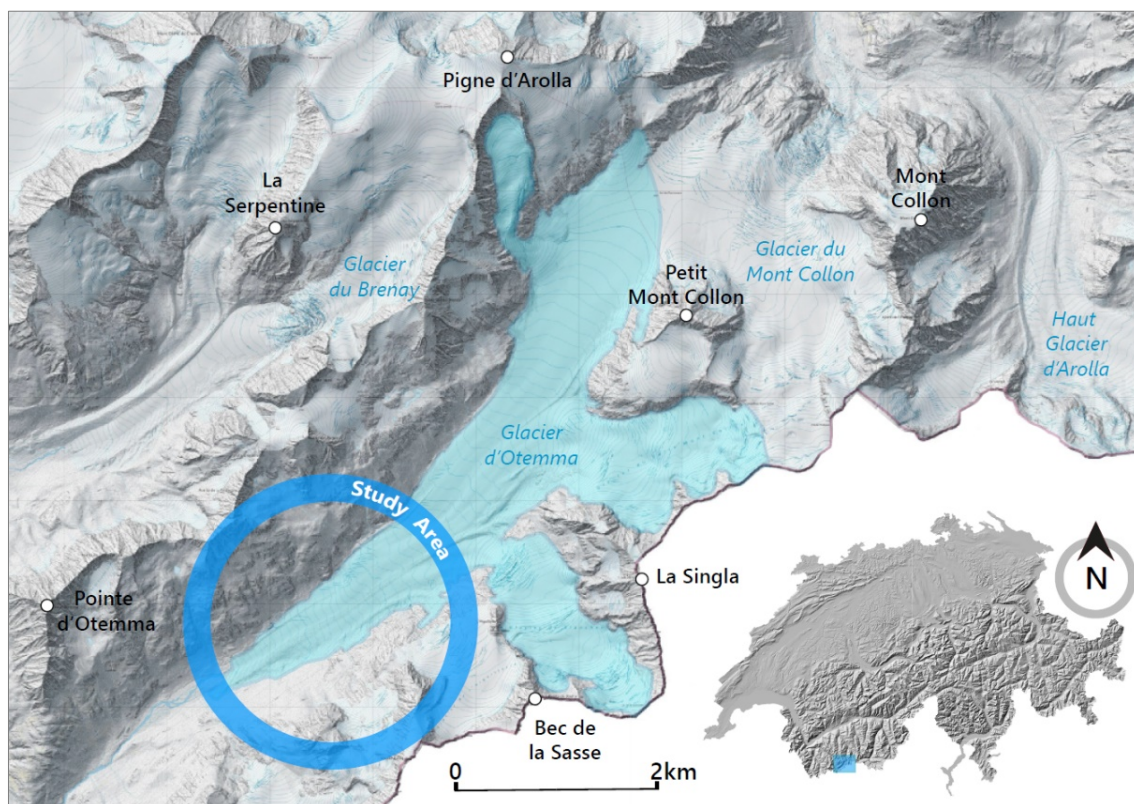
Figure 6. **Study area representation**
Glacier d'Otemma, shown in the blue frame on the relief representation of Switzerland (via the Swissalti3D model). The current measurement of the Glacier d'Otemma (in light blue) has been estimated at 9.66 m^2, according to estimates made on © Swisstopo in 2017. The study area is located about 1.25 km distance from the front of the glacier tongue.

After observations of period maps, terrestrial and aerial photographs, and satellite images, the perimeter of the glacier was drawn by hand in 2017. The current glacier surface area is estimated to be about 9.66 km^2 (Fig. 6). Glacier de Blanchen (between Bec de la Sasse and La Singla) and Glacier du Petit Mont Collon (between La Singla and Petit Mont Collon) should be included in representations of Glacier d'Otemma, as their connections influence the dynamics of the latter. The boundaries with the Glacier du Mont Collon are linked to two passes: (1) the Col de Charmotane at the north of the Petit Mont Collon and (2) the Col du Petit Mont Collon at the south of it. From observations collected from © SwissTopo (App. 1) and the measurements carried out in the field (Fig. 7), the retreat has gone through different phases over different periods. The retreat increased considerably from the late 1960s to the late 1970s. A short reduction in the rate of glacial retreat occurred in the early 1980s, linked to a period when average temperatures were lower than previously (NCCS, 2018), before becoming irregular, with high temperature periods (1996, 2003, 2006 and 2016).

Glacier d'Otemma length changes between 1881 and 2016
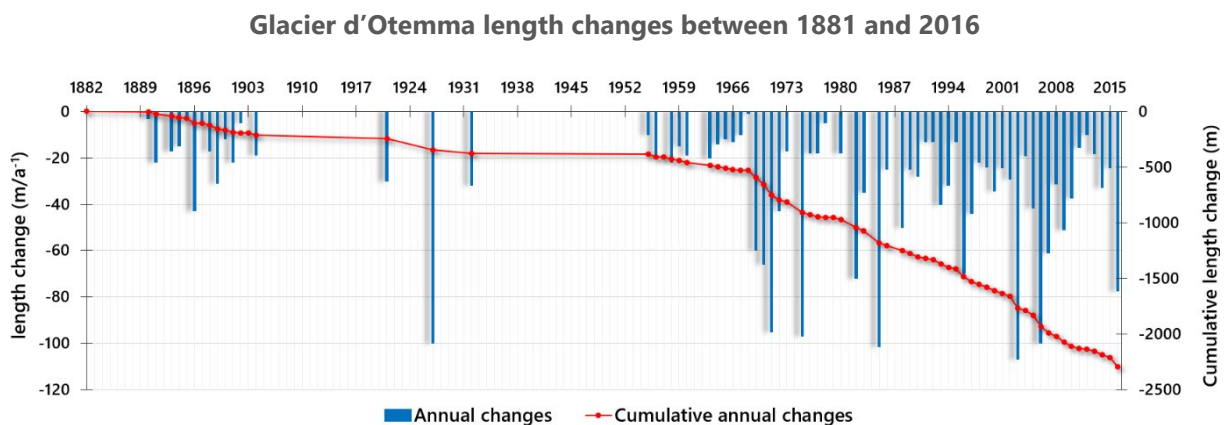
Figure 7. Glacier d'Otemma length changes between 1881 and 2016
Graph showing the length changes made during the monitoring of the Glacier d'Otemma between 1881 and 2016, through the GLAMOS programme, which is a Swiss glacier monitoring network. The no data for some years is due to a measurement lack.
Source: GLAMOS Programme, Eidgenössische Technische Hochschule Zürich, ETHZ, 2019.

Ice ablation measurements (App. 2), carried out in the field in 2019, were undertaken using ablation stakes distributed over the surface of the glacier tongue. Ten stakes were placed on the lateral and middle parts of the glacier. Ice surface loss was about 7 cm per day, for thirteen days in July 2019, and about 5.7 cm per day, for seventeen days in August 2019. The total ice surface loss was about 1.90 m over thirty days. According to GeoCover®, vector data from © SwissTopo, the lithology of the valley, is mainly composed of loose rocks, such as till and scree with undifferentiated lithology. The northern slope is mainly composed of Permian granodiorite, and the southern slope, of gneiss. Granodiorite is a plutonic magmatic rock close to granite and is mainly composed of quartz (rocks.comparenature.com, 2015). It is an intrusive coarse-grained igneous rock containing quartz and plagioclase, and has the composition between granite and diorite, very resistant to erosion, unlike gneiss, which is a much more rigid metamorphic rock. Gneiss is a common and widely distributed type of rock formed by regional metamorphic processes from pre-existing formations that were originally either igneous or sedimentary rocks. Granodiorite is more prone to chemical weathering, frequently linked to glacial erosion, while gneiss is more prone to mechanical and biological weathering.

3.2. Field measurements

3.2.1. Overview

Previously studies using active seismics have used a methodology based on longitudinal and transversal glacier profiles to identify certain subglacial features, such as glacier thickness, sediments, and ice quality (King et al., 2008; Zechmann et al., 2018; Church et al., 2019). Polom et al. (2014) proposed the *cross spread* method to perform simultaneous recording of the transversal and longitudinal profiles. In theory, this technique provides wave velocities and reflectivity as function of angle and could improve the interpretation of bedrock characteristics. The sites distribution (Fig. 8) was designed to provide an investigation area greater than one kilometre to analyse bedrock composition across the entire glacier.
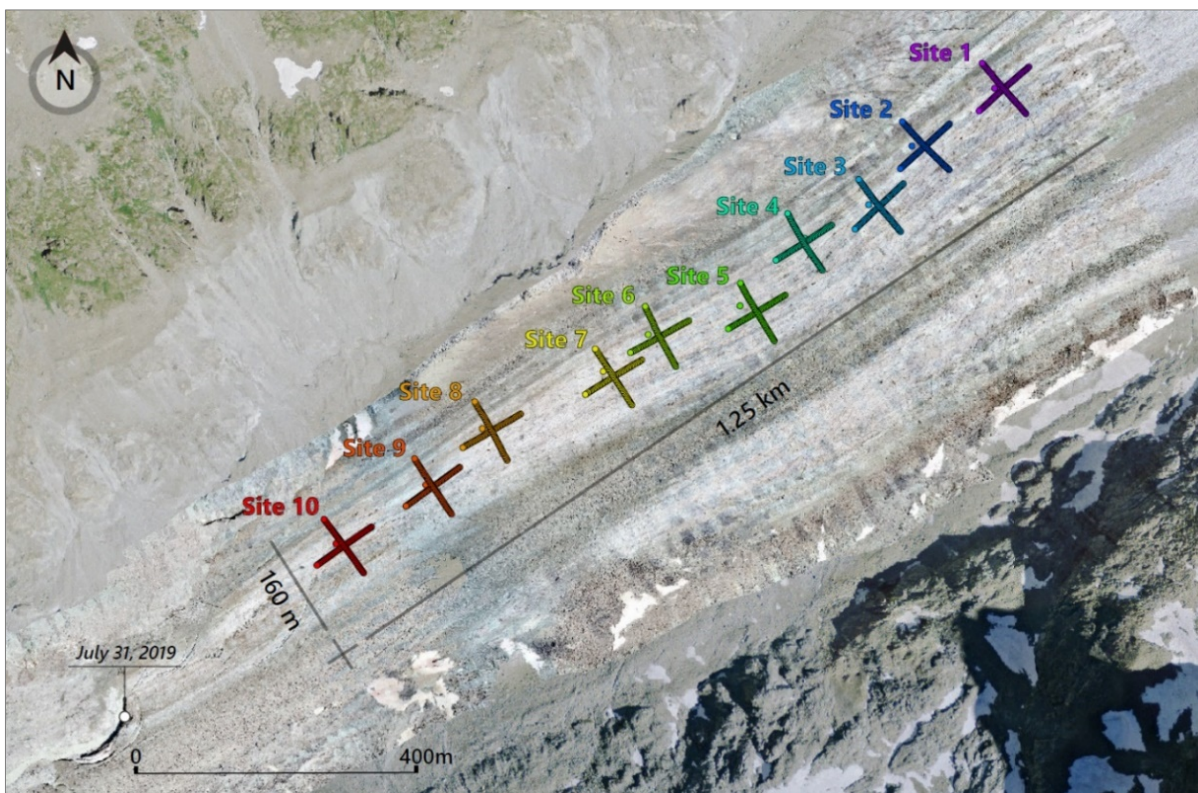
Figure 8. 10 study sites
10 study sites representation on the Glacier d'Otemma, July 31st, 2019, since a Digital Elevation Model (DEM), for the cross-measurement technique. The front was then at 2511 m.a.s.l. Each site did 96m x 96m and composed of 96 geophones spaced every two meters, 4 seismic recorder geodes in the center of the cross, a trigger, an acquisition computer, the sources, and accessory material. The entire study area covers about 1.25 km along the glacier, over about 160 m width.

The south-western part of the glacier was preferred for three reasons : (1) this glacier area has been extensively studied by other researchers (Sala, 2019; Egli et al., 2020) using GPR, (2) it has important subglacial activity and (3) it was easier to access for active seismic measurements. Factors that have determined the spatial distribution of the sites are related to (1) the assumed direction of subglacial flow, (2) the absence of debris-cover on the glacier surface, and (3) the absence or partial presence of supraglacial forms (crevasses, active glacial moulins and supraglacial channels). Each site was about 150 to 220 m distant from each other, from the *cross spread* centre.

3.2.2. Equipment

ElViS (Fig. 9) generate P- or S-waves sweep signals (© Geosym, 2019). The Geosym GmbH® ElViS III P8 has a movable mass driven by a linear cascade motor powered by a 12 V battery pack. It emits sinusoidal waves in the form of vertical micro-tremors on the surface, over a specific time and frequency range. An amplifier regulates the amplitude of the waves emitted from the *vibrator pot* under the wheelbarrow chassis. The 35 kg *vibrator pot* has at its base a vibratory plate, directly placed on the ice surface, which will transmit the vibrations in the ice. Adjustable air suspension ensures that seismic energy potential on the surface is optimised. The system is calibrated, and also parameterized, by a signal

Figure 9. *ElViS during measurements*
View from the laboratory, with ElViS during measurements. During the shot, it is necessary to have a person on the source in order to create a greater load on the vibroseis and to allow a better adhesion of the plate, under the vibratory pot at the wheel.
Source: *Thomas Tscharner, 2019.*

generator, the *trigger*, used with a programmable microchip which allows definition of the desired frequency range, but also the emission distribution over a given time. The frequency range that can be performed by the vibration source is between 20 and 400 Hz. The *trigger* and ElViS are connected by an electric cable.

Figure 10. *Sledgehammer during measurements*
View from the laboratory, at the site crosspoint, with sledgehammer during the measurements. When impacting against the plate, it is important that the plate remains in place, anchored in the ice, so as not to have any rebound that could interfere with potential reflector during processing
Source: *Thomas Tscharner, 2019.*

To create our impulsive seismic source, a 9.1 kg sledgehammer (Fig. 10) is used to strike a 5-cm-thick hard plastic plate located on the ice surface. It consists of cables equipped of two electrical wires with two male tips, taped against the handle and connected to an electrical reel whose tip fits the *trigger* connector of the *pilot geode*. This geode serves as an intermediary between the information received by the geophones, stored by the geodes, and the acquisition computer. With the shock effect between the mass and plate, the two male tips collide to activate the *trigger*, and thus allow the recording of measurements.

Ninety-six 30 Hz geophones were deployed and © Geometrics Geodes were used with a 20 kHz resolution (i.e. an 8 to 0.02 m·s^{-1} sampling rate), near-zero distortion (0.0005%), low noise (0.2 uV) and 1/32 sampling interval (© Geometrics, 2018). Four geodes were used to acquire and to record information received by the geophones, i.e. one geode per line of 24 geophones. In the *cross spread*

system, the geodes are in the site crosspoint, at the *laboratory*, so that they can themselves be connected to an acquisition computer that will collect the data.

A differential Global Positioning System (dGPS) was used to calculate the exact coordinates of each measurement point (i.e. 960 points). It transmits the difference between the positions indicated by the satellites and the known positions on the ground. The use of a drone enabled acquisition of Digital Elevation Models (DEMs). The coordinates acquired and the DEMs were needed in order to map the position of each measurement site, as well as the geophone positions (Fig. 8), but also to collect monitoring data concerning the Glacier d'Otemma. In order to facilitate efficient equipment transport between each study site, two metal sleds (*rescue sleds*) specially designed for transporting heavy objects and people were used. Two 2000 W mobile generators, four 12 V external batteries and two 10 A battery chargers were used to provide the energy supply for the system.

3.2.3. Measurement protocol

Daily data collection, over a 24-hour period for each study site, involved four main steps: (1) equipment preparation, (2) geophone stabilization, (3) seismic measurement and (4) moving equipment. The equipment was placed on site in the late afternoon/early evening, the day before the measurements. During this period, the melting is less marked than during the day and this allows the geophone to remain more stable thanks to overnight refreezing. *Cross spread* (Fig. 11), for a single site, is composed of four 50 m long seismic flutes cables of which is connected 24 geophones with 2 m interfaces. The distance between geophones determined the data spatial resolution.
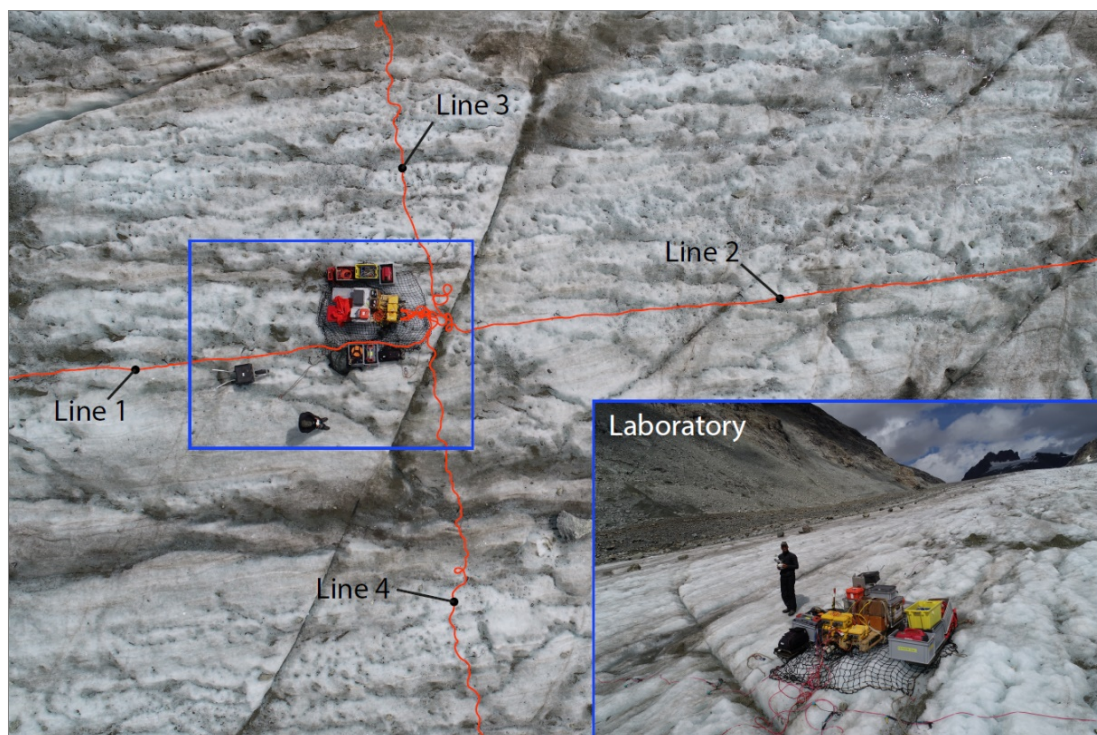
Figure 11. *Cross spread*
At the crossing of these four 50 m geophone cable lines (flute), the laboratory, where all the sources and material for recording, storage and previewing the data collected during the measurements are grouped together.

The four lines (Fig. 11) had to be set up in order to ensure consistency in data collection. *Line 1*, to the East of the system, and *line 2*, to the West, were deployed parallel to the glacier flow direction. *Line 3*, to the South of the system, and *Line 4*, to the North, were deployed perpendicular to the glacier flow direction. The geophones were implanted perpendicular in the ice, as close as possible to the geophone and flute tip, in order to improve its reception efficiency. To stabilize geophones on the glacier surface, the ice was drilled about 5 to 7 cm depth before the metal tip was inserted. A percussion drill was used to avoid fracturing the ice around the geophone, which would make it unstable. Geophone organisation during the measurements was carried out via the acquisition computer. *Line 1* consisted of the geophones from 1 to 24 and from 49 to 72 for the *Line 3,* outside to inside of the system. *Line 2* consisted of the geophones from 25 to 48 and from 73 to 96 for the *Line 4*, inside to outside of the system.

The *laboratory* installation (Fig. 12) was necessary in order to have all the measuring material available at the centre of the system, in case of system failure, and then for practical and organisational purposes. The lines were each connected to a geode. The geodes were connected to an external 12 V battery and each other, via network cables. The order of these connections was important. The geode of the *line 1* (*geode 1*) was connected to the geode of the *line 2* (*geode 2*), *geode 2* to the geode of the *line 3* (*geode 3*) then *geode 3* to the geode of the *line 4* (*geode 4*). However, a fifth geode was required during measurements: the *pilot geode* was connected to *geode 4*, by a network cable, and to the *sweep*, through the line connector.
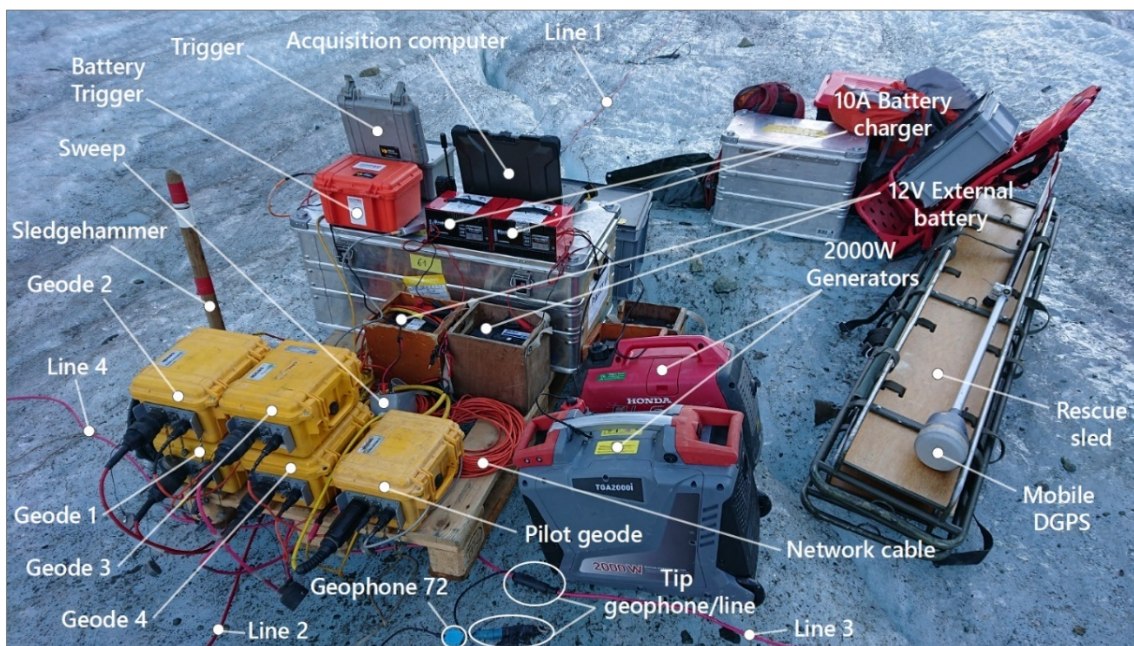
Figure 12. The laboratory with the seismic and complementary material

The *sweep* defines the frequency range duration and linearity set in the system, between the start and stop frequency, and was connected to the *trigger*. The *trigger* was used to switch on the vibrator, via an electric cable, and is connected to an external battery to be powered. The source duration was 10 s over the 20 to 240 Hz frequency range for the vibroseis. For the sledgehammer, the pulse waves emitted

depended on the shot power. For both, the recording time was adjusted to 8 s, for 2 s listening time, taking into consideration that the wave velocities in the ice is between 3100 to 4500 m/s and between 1500 to 2300 m/s in the till (Hilbich et al., 2010; Kim et al., 2010; Scapozza et al., 2011; Bradford et al., 2013; Hofstede et al., 2018). The time interval in the data collection was estimated at 1 ms, in order to have enough data to process during the processing. Parameters were the same for each measurement, in order to maintain a consistent protocol for data analysis.

The source was at a distance between 10 to 60 cm from the geophone, for each measurement, i.e. 192 measurements per site. The first plane of the series was not correlated to the whole system, only on the *pilot geode*, in order to be able to observe the regularity of the sinusoidal curve of the *pilot trace*. If it was regular, symmetrical and if the trace amplitude decreases as a function of travel time, the whole system was operational. If it was not, it was because there was still a defect in the system. This could be due to the source, *trigger*, vibroseis amplifier or cable connections. For the ElViS, combinations of two stacks were carried out, because the vibrator did not always have the same power required during the shot, which could reduce the data quality on some geophones. The assistant moving the vibrator sat on it in order to add mass to the vibrator and improve the *vibrator pot* contact against the ice surface, to limit bounces. For the sledgehammer, several shots were carried out in order to be sure that there was a shot that met the criteria (legibility, presence of potential traces, no bouncing of the plate, etc.).

3.3. Processing and analysis

3.3.1. Reflection seismic processing

Given the nature of the ice, located in the ablation zone, there was no fresh snow, snowpack or firn on the glacier surface. For the sake of simplification, and as recommended in Zechmann et al. (2018), we will assume a uniform P-wave propagation velocity over the entire glacial structure and the subglacial material, so that thin layer effects do not distort the wavelets reflection (Widess, 1973; Zechmann et al., 2018). The basic codes obtained for the reflection processing, proposed in this work, come from the Consortium for Research in Elastic Wave Exploration Seismology (CREWES), an applied geophysical research group at the University of Calgary that shares certain open-source data acquisition and analysis resources. These codes were modified by Ludovic Baron in order to be adapted to this work.

The *Data Importation* (Fig. 13) began by importing the seismic data under four seismic profiles: (1) a longitudinal profile of the vibroseis (*line 1* and *line 2*); (2) a transversal profile of the vibroseis (*line 3* and *line 4*); (3) a longitudinal profile of the sledgehammer (*line 1* and *line 2*); and (4) a transversal profile of the sledgehammer (*line 3* and *line 4*). The *Assign Geometry & Editing Traces* (Fig. 13) consisted of the transcription of the field distribution of the geophones (1 to 48 for the longitudinal profiles and 49 to 96 for the transversal profiles), the interface between geophones (2 m), recording time (2 s), and involves the transcription of four parameters reproducing the geometry of the data: (1) the sources, (2) the receivers, (3) the Common Depth Point (CDP) and (4) the offsets. In our case, CDP represents the midpoint between the source and receiver.
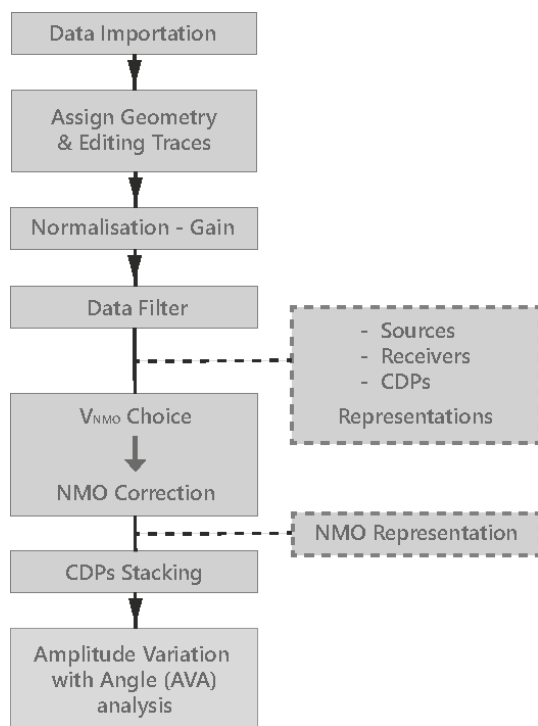
Figure 13. *Reflection seismic processing workflow*
The diagram describes the reflection processing workflow. Solid line frames represent the main processing steps and dashed line frames represent the secondary steps for data analysis.

Assigning a geometry to the seismic data means that, for each trace, the source position, receiver position, midpoint, and offset are obtained. The emission source number consisted of 48 sources and 48 receivers, with a 2 m interval distance between each source and each receiver. The essential data to obtain offset and CDPs is linked to point sources and receivers. For a source and receiver position, according to a given trace, these are represented by a given source and receiver as a function of the interval between sources and receivers. The CDPs, at a certain point position, is thus this distance divided by two, because it lies vertically between these two points. The offset represents the horizontal distance between the source and receiver position. These values imported from the acquisition data thus form the geometry spreadsheet, corresponding to four profiles: (1) longitudinal profile of the vibroseis (*Long_Vib*); (2) transversal profile of the vibroseis (*Trans_Vib*); (3) longitudinal profile of the sledgehammer (*Long_Ham*); (4) transversal profile of the sledgehammer (*Trans_Ham*).

In order to be able to easily observe certain traces in a section, it was necessary to apply a certain level of gain (Shan & Kailath, 1988). Large amplitude samples close to relatively small amplitude events can sometimes reduce the traces legibility of the seismic section. The *Normalisation* (Fig. 13) of trace amplitudes, via a *Gain* control method (Fig. 13), allows time windows on these traces to be examined and the event amplitudes in this window to be adjusted with respect to a selected standard. This helps correct for amplitude losses in time due to the geometrical spreading of energy and attenuation losses (Feagin, 1981; Lumley & Bowman, 1987). On CREWES codes, the gain correction is applied automatically by an Automatic Gain Control (AGC). However, it is necessary to set a *correction indicator* ranging from 1 to 2000 in the profile to be processed. The higher the indicator, the more the selected profile appears with a corrected gain.

The *Data Filter* (Fig. 13) is used to attenuate the seismic signals components or noises, between a lower and a higher cut-off frequency (Mousa & Al-Shuhail, 2011). The CREWES highlights the Butterworth filter band-pass, suitable for high frequency filtering, which requires the introduction of five variables: (1) the time taken by the descending wave between source and receiver, (2) the sampling frequency (1000 Hz), (3) the lower cut-off frequency (70 Hz), (4) the higher cut-off frequency (250 Hz) and (5) the number of profiles analysed (4).

The *Representations* (Fig. 13) are proposed to plot the data from three perspectives (Fig. 14): (1) *Sources* (vibroseis), (2) *Receivers* (geophones) and (3) *CDPs*. These different representations make it possible to visualise the seismic sections, to analyse the traces, to observe possible reflectors and to make

adjustments in the event of errors or inconsistencies (shift in the data, axis inversion, coding errors, etc.). If the set is correctly aligned, between the first propagation point and the CDP number, then the geometry is theoretically correct. The representations of seismic profiles in this work have been set up in order to guarantee a constructive legibility of the traces. The travel time (ms) for the visualisation has been set at 150 ms. At 100 ms, the representation of the profile prevented a clear visualisation of the potential traces. At 200 ms, the lower part of the section did not bring any added value in the analysis of the profile traces to be represented. CDP data will be considered in the next step of the methodology, in order to be able to build the Normal Moveout (NMO).
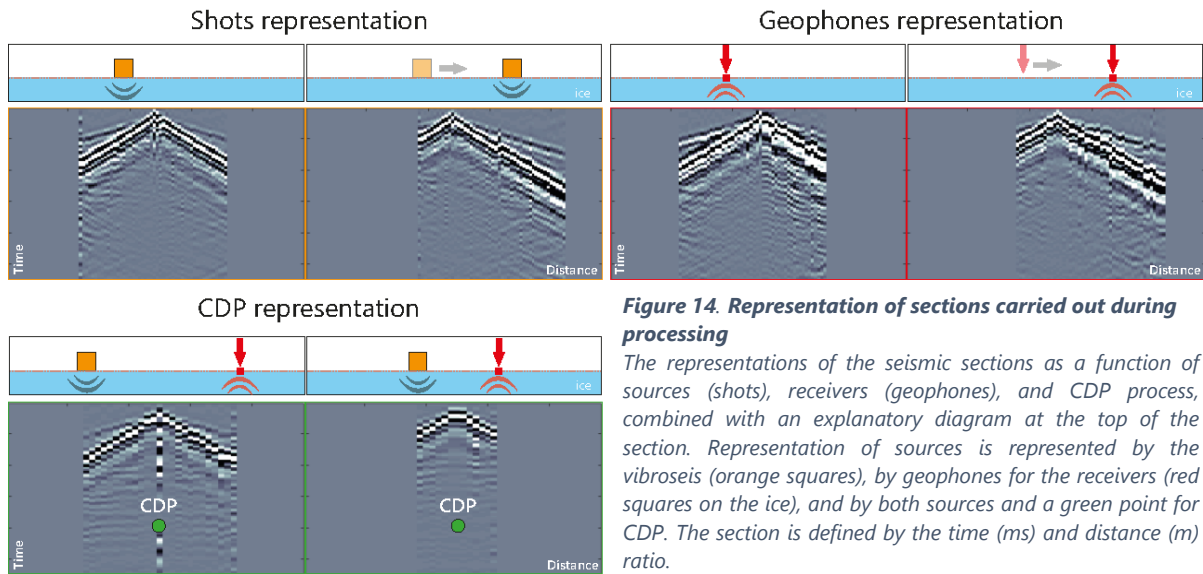
Figure 14. Representation of sections carried out during processing
The representations of the seismic sections as a function of sources (shots), receivers (geophones), and CDP process, combined with an explanatory diagram at the top of the section. Representation of sources is represented by the vibroseis (orange squares), by geophones for the receivers (red squares on the ice), and by both sources and a green point for CDP. The section is defined by the time (ms) and distance (m) ratio.

The *VNMO choice* (Fig. 13) allows insertion of a velocity value to remove the moveout effect on travel times for a flat interface. The NMO velocity is determined by observing the velocity at various times down the record that results in the flattening of the hyperbolas of the subsurface reflector in each event (Onajite, 2013). This allows dynamic correction of the profile by compensating for the hyperbolic trajectories effect, to reduce the potential reflectors arrival times to those of zero offset tracks (Yilamz, 2001): the *NMO correction* (Fig. 13). This step depends on the velocity over the reflector, the source-receiver offset time, the reflector dip, and the source-receiver azimuth relative to the dip direction. In order to find the optimum velocity, several velocities tests were realised to have the best flattening of the reflection hyperbolas via the *NMO Representation* (Fig. 13). If the velocity is wrong, then the reflector will either go up or down as a function of offset. After NMO correction, the traces can be stacked to improve the signal-to-noise ratio and be displayed as a seismic profile image with flattened reflectors (Yilamz, 2001): the *CDPs stacking* (Fig. 13). The whole NMO process described in this paragraph can be expressed through this equation (5; Kearey et al., 2013):

$$\frac{2z}{v_1}\left(1 + \left(\frac{x}{2z}\right)^2\right)^{\frac{1}{2}} - T_0 = T_{Reflected} - T_0 = \frac{1}{2}\left(\frac{x^2}{v_1^2 T_0}\right), \tag{5}$$

where x represents a particular offset between a source and receiver, with an interval velocity v_1 and a wave propagation depth z, we obtain a travel time of the reflected wave $T_{Reflected}$, which we will subtract

from the time at zero offset T_0, to arrive at the process for obtaining the NMO. Henry (1997) and Verney (2009) propose criteria for efficiently identifying reflector traces in a section. The reflector is assumed to be horizontal, parallel and have chronological relationships with neighbouring reflectors to demonstrate that it is part of a reflection sequence.

Briefly, it is possible to perform two additional steps, not covered in this work: (1) deconvolution and/or (2) the migration. Deconvolution is used to get rid effect of the seismic wavelet. This process will contract the pulse emitted by the source, in order to bring it back as a short pulse (spike-type impulse), with a low number of oscillations, to make it more perceptible (Lavergne, 1986). Migration is about reducing distortions in order to obtain a clear picture of the data and has the effect of: (1) accentuating dips by moving the reflectors on the rise side of the stack, (2) increasing spatial resolution and (3) focusing diffraction (Bitri et al., 1996). During standard seismic reflection processing, stack migration is carried out before more complex analyses (AVA, propagation veloicty depth, etc.). These two steps were not carried out because they did not add value to the data quality.

3.3.2. Near-surface refraction seismic processing
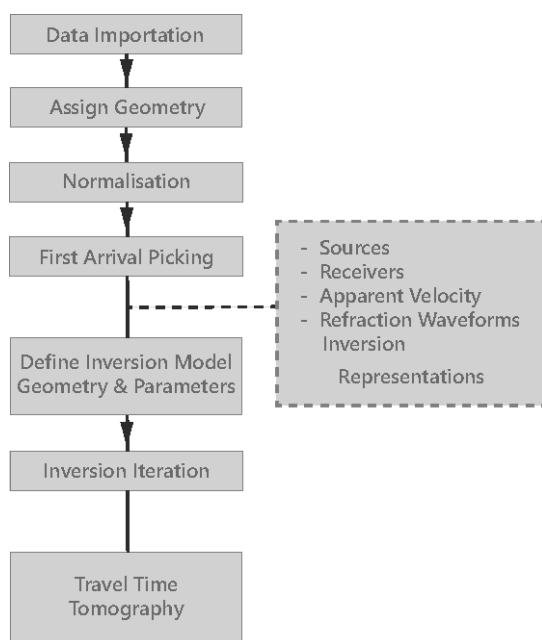
Figure 15. **Near-surface refraction processing workflow**
The diagram describes the common workflow for the refraction near-surface processing. Solid line frames represent the main processing steps and dashed line frames represent the secondary steps for data analysis.

The spatial distribution of the P-wave velocity will be estimated by the travel time tomography. The basic codes obtained for the refraction tomography and the integrated parameters, proposed in this work, were written by James Irving and Ludovic Baron, based on previous research/work. Processing of refracted arrivals in the seismic data was carried out using travel time tomographic inversion. This consists of inverting a large number of travel times for non-coincident sources and receivers located on a surface, in order to determine the spatial distribution of wave velocity distribution in the subsurface and to find a velocity model which minimizes the error energy between the measured and predicted travel times (Zhang et al., 1998).

The *Data Importation* (Fig. 15) according to the same principle as in the part on the *Reflection seismic processing*, mentioned in Section 3.3.1., i.e. 2 m source and receiver interface, defined by the 48 positions in the longitudinal line and 48 positions in the transversal line.

The *Assign Geometry* and *Normalisation* (Fig. 15) involve, for each seismic trace acquired, the acquisition of the source and receiver position along the profile on a 2D matrix (X, Y). Only sledgehammer data related to sources and receivers are used to carry out the travel time tomographic inversion. This inversion used a constant starting model having a slowness value of 3200 m/s. After performing the data

normalisation, it is necessary to pick the time of the first arrival on each trace. For this study, the *First Arrival Picking* (Fig. 15) were picked manually. The first arrival for refraction studies is mainly related to the structure close to the surface, the type of source used and the conditions in the signal-to-noise ratio (Senkaya & Karsli, 2011). This relies mainly on the amplitude intensity and changes in waveforms, as well as the data quality. In order to facilitate and improve the accuracy of the first arrival picking, four graphical applications have been plotted: representations of seismic profiles for (1) each source and (2) receiver, in order to visually identify the refraction wave, (3) evaluations of the apparent velocity between the sources and receivers and (4) observations of the inverted curve of the refraction wave, constructed from the picking carried out, via the profile linked to the receivers. The travel time (ms) was set to 30 ms for the refraction wave curve and 50 ms for the seismic profiles. These travel times allow a sufficiently detailed display for the most accurate picking possible. Apparent velocity is the wavefront velocity moving along of geophones line on the surface of a medium. Negative values for apparent velocity reflect the fact that arrival times become shorter and shorter as the pick moves away from the source, and vice versa for positive values (Magnin & Bertrand, 2005).

The *Define Inversion Model Geometry & Parameters* (Fig. 15) involve determining the coordinates (X, Z) of model cell to define the inversion grid, with regard to geometry. The parameters are defined by the number of outer nonlinear tomographic iterations (25). The other additional parameters like the weight of the model smallness and the model smoothness, in the XZ-direction, as well as the starting velocity of the slowness model (0.3125 s/m), have been selected arbitrarily, in a logic of adapting the velocity towards a greater continuity in the X-direction than in the Z-direction. The *Inversion Iteration* (Fig. 15) will therefore make it possible to reach the minimum of the inversion objective function. This is done by calculating the new Jacobian derivative at each iteration (Shanno, 1970; Weisstein, 2004; Tarantola, 2005; Huang et al., 2017). For the *Travel time Tomography* (Fig. 15), the 25th iteration will be represented over an analysis velocity range established between 1000 and 4000 m/s, taking into consideration the reference values of P-wave propagation velocities in different types of materials (Fig. 1; Hilbich et al., 2010; Kim et al., 2010; Scapozza et al., 2011; Bradford et al., 2013; Hofstede et al., 2018).

Results and discussion

Results and discussion
Clouds dance

Arrival of clouds and warm air from the Haut Val de Bagnes valley. View from the site 5. In the background, Mont Gelé (3518 m.a.s.l.) in the center and Pointes du Jardin des Chamois (3260 m.a.s.l.) on the right.
Boris Ouvry – July 31, 2019

4. Results

The results did not live up to expectations and certain steps of processing could not be carried out. We will show the results obtained during the data processing and will highlight them through: (1) a summary of the acquisition parameters, in order to have an overall view of the measurements acquired on the field. (2) the results related to the seismic reflection process carried out, for each step of the process, and (3) the results related to the seismic refraction process, through the different steps carried out.

4.1.   Data acquisition parameters

***Table 2**. Seismic acquisition parameters and measurement dates*
Tables containing information on the acquisition parameters carried out in the field, as well as information related to the dates when the measurements were carried out according to the site number, for seismic data related to ElViS and sledgehammer.

P-wave acquisition sheet			Site n°	Date
	ElViS	Sledgehammer		
Instrument	Geometrics Geode 96		1	18.07
Sample interval	1 ms		2	19.07
Record length	2 s		3	23.07
Record type	SM24 - 14 Hz		4	25.07
Record space	2 m		5	02.08
Source type	Vibratory	Pulse	6	04.08
Source space	2 m		7	06.08
Sweep type	20 - 240Hz	unknown HZ	8	09.08
Recording	8 s		9	11.08
Vert. stack	2 (same polarity)	1	10	14.08
CMP-fold	95			

The parameters of the acquisition carried out (Tab. 2) include a 20 to 240 Hz range frequency recorded over 8 s, with a 1 ms time interval and a 2 s recording length. All the sites measured were processed for the seismic reflection. The representations of the CDP stacks, for each sites, can be seen in the appendix (App. 3 to 7). Site 4 and 6 served as a reference in the description of the various processing steps performed during the seismic reflection and were the only sites treated for seismic refraction. These sites have the most representative characteristics in terms of data quality.

For the part related to the reflection processing, seismic profiles of different parameterised values, with descriptions of the visual characteristics for each of these values, will be presented, as well as a final representation of CDP stacking from the site 6. For the part devoted to refraction processing, graphical representations in connection with the data picking, as well as travel time tomographic models of P-wave propagation velocities from the site 4 and 6, will be proposed.

4.2.   Results from reflection processing

4.2.1.   Processing: the geometry, gain and data filtering steps

The CDP 48 of the longitudinal sections (Fig. 16) has been selected, for comparative purposes between the vibroseis (Fig. 16A) and the sledgehammer (Fig. 16B). They are representative of the transversal section in terms of gain processing, as well as for the source and receiver representations made during processing. The gain correction in this phase of normalisation of the seismic profile is progressive from the centre to the lateral parts of the profile and proportional according to a *correction indicator*. When there is almost no gain correction (*Gain 1*), it is possible to distinguish characteristic traces between the

vibroseis and sledgehammer profiles. The profile of the sledgehammer is characterised by trace-to-trace frequencies that are more intense than vibroseis, which, combined with a high amplitude of the traces, completely covers the profile without it being possible to distinguish reflective and refractive forms. For vibroseis, it is possible to partially observe the refracted waves and direct wavelets, but also, possible short-path multiples. Note the presence of noises in the centre of the vibroseis profile, where the source is located. The gain correction visible is similar between the 100 to 2000 indicator.
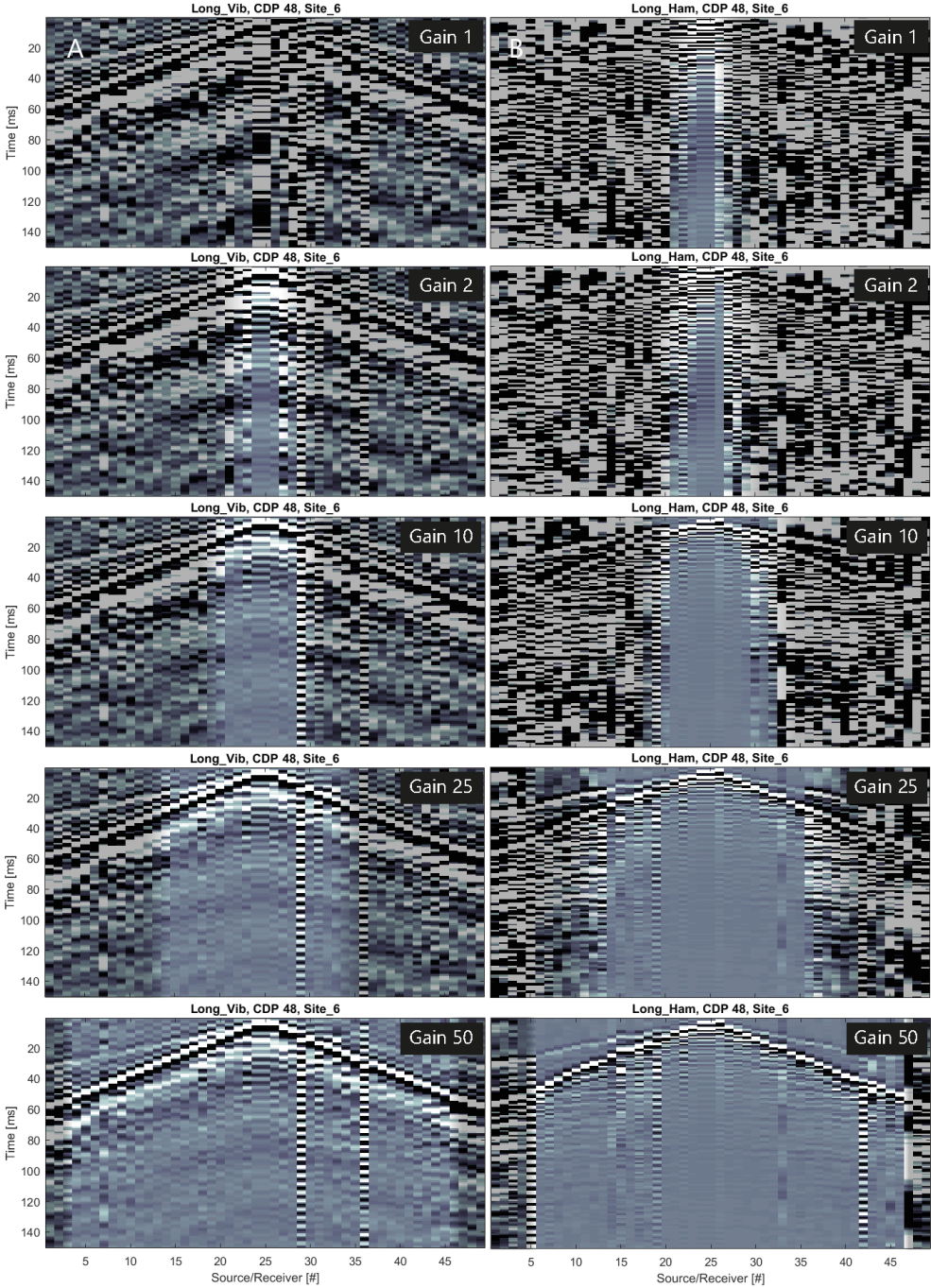
Figure 16. CDPs representations based on gain correction, for the longitudinal section, at site 6
Comparison of longitudinal seismic profiles (Long_) at CDP 48 and without data filter, between ElViS (Vib_; A) and sledgehammer (Ham_; B), according to the indicator of the gain correction applied during processing: 1, 2, 10, 25 and 50. These data depend on the relationship between the time (ms) and distance (m). The part in transparent black represents the parts of the profile that cannot be used. Note that it is not possible to have a 0 indicator, and the Gain 100, without filter, will be shown in the next figure (17).

The attenuation by the decrease of the traces amplitude is much more evenly distributed through the profiles linked to the sledgehammer and therefore much more efficient than for the vibroseis. The data filter setting up, represented by the transversal section (Fig. 17), has been set up with different frequency ranges, in order to find the most suitable range to achieve the sharpest possible profiles visualisation.
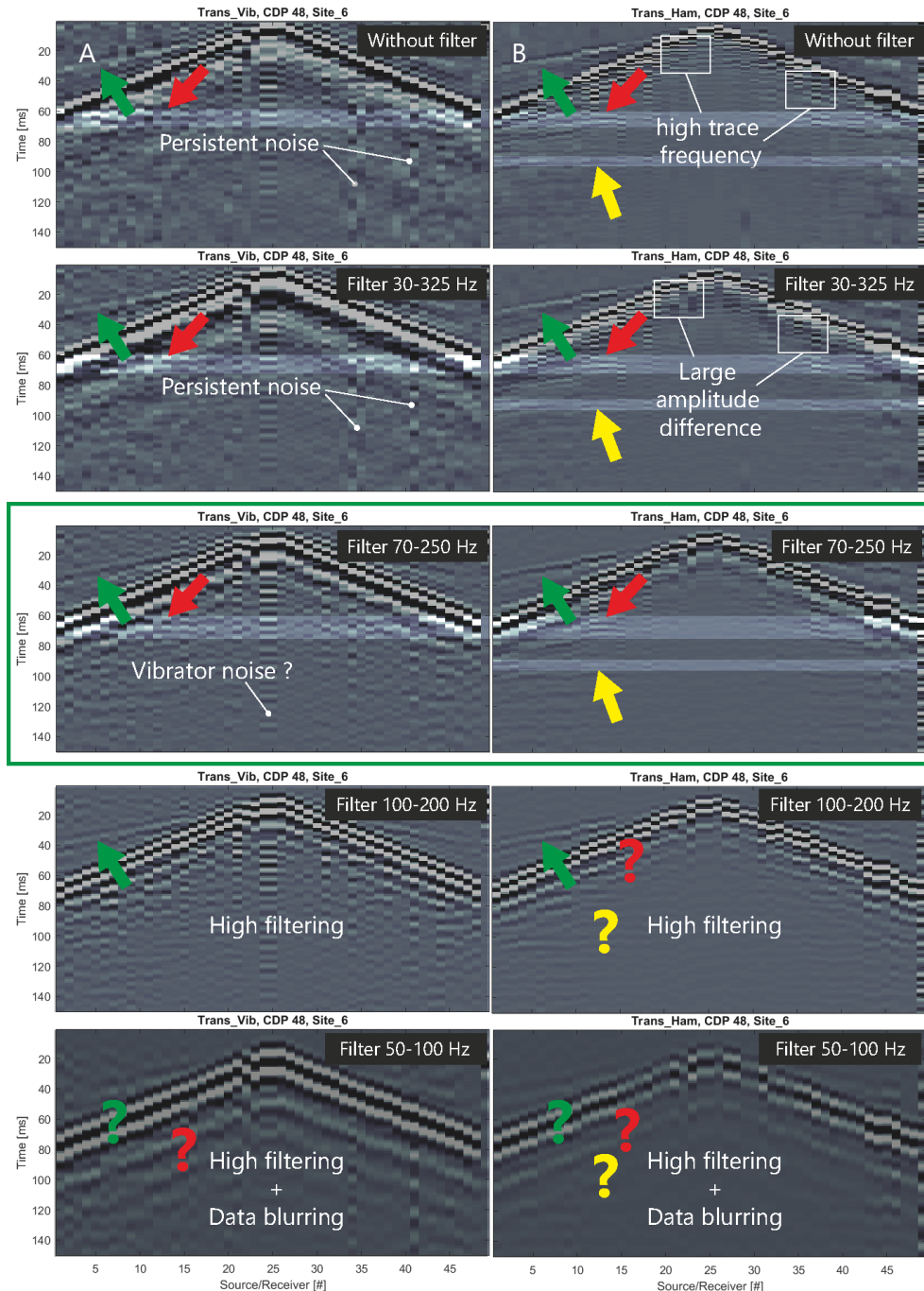
Figure 17. CDP 48 representations based on the filtered data set, for the transversal section, at site 6

Comparison of transversal seismic profiles (Trans_) at CDP 48 with a Gain 100, between ElViS (A; Vib_) and sledgehammer (B; Ham_), according to specific frequency range : without filter, 30 to 325 Hz, 70 to 250 Hz, 100 to 200 Hz and 50 to 100 Hz. The yellow arrows represent reflection traces, to compare the different filters between the sledgehammer profiles. The yellow question marks represent them but are no longer visible. The red arrows represent reflection traces, to compare vibroseis and sledgehammer profiles against a selected filter. The red question marks represent them that are no longer visible. The green arrows represent the visible refracted waves of the profile and the green question marks when it is not visible anymore in the profile. The white markings represent the main defect/noise visible on the profile. These data depend on the relationship between the time (ms) and distance (m).

At gain correction with 100 indicator and without filter (Fig. 17), there remains a completely satisfactory sharpness and legibility of the traces for sledgehammer-related profiles (red and yellow arrows), thus demonstrating the effectiveness of the normalisation step. Note the relatively correct resolution of the data without the filter. However, the signal-to-noise ratio is not sufficiently balanced, with a high frequency of traces along the direct wavelet (at a slightly later in the travel time), which confuses the data and makes legibility less comfortable, and justify the application of a data filter.

Frequency ranges (Fig. 17) that are too wide, e.g. between 30 to 325 Hz for example, are not sufficient to obtain a signal-to-noise ratio that allows comfortable legibility of the data, especially along the direct wavelet (later in the travel time), where there is still a large difference in wave amplitude obstructing the legibility of certain traces. This observation is much more pronounced for the sledgehammer profile, that for the vibroseis profile. There are not concrete changes compared to unfiltered data. Frequency ranges that are too narrow tend to eliminate potential reflectors, making them blurred, as if the pixel density of the trace was reduced. Note the similarity in the loss of time resolution, during the process, between those related to vibroseis and those related to sledgehammer. Initially, between 100 to 200 Hz for example, a decrease in the legibility of the refraction wave and the appearance of the first noises appear. In a second time, between 50 and 100 Hz for example, these observations are even more accentuated, with a disappearance of all potential reflective traces, as well as refracted, but also a significant increase in noises and blurring of the data. The direct wavelet is also visually coarser, with an excess of amplitude. The 70 to 250 Hz frequency range was chosen as a compromise between noise reduction and clearly being able to see the refracted wave arrival, which is necessary for in the glacier surface tomography. The steps related to data normalisation, gain, and data filtering, have shown two visual characteristics that are not conducive to sufficiently constructive processing: (1) a significant presence of noise, more marked on the ElViS profiles, and (2) an excessively high traces amplitude, mainly also on the ElViS profiles.

4.2.2.   Representations sub-step processing

Some potential reflectors can be observed and interpreted on the profiles of the site 6 and show that the data could provide interesting observations. These traces correctly meet the criteria proposed by Henry (1997) and Verney (2009), mentioned in section 3.3.1, on the criteria for detecting potential reflectors on a seismic profile. The representations of the sources and receivers (Fig. 18) allowed a first visual analysis in order to optimise the parameters related to the gain, as well as the frequency range of the data filter.

For seismic profiles linked to source number 20 and 32 (Fig. 18A), from the longitudinal section of the site 6, fine reflection traces on the side parts of the profile emerge. These mainly appear around 40 ms (yellow arrows) and more distinctly around 70 ms (red arrows). Potential reflectors around 70 ms are visible for the vibroseis, as for the sledgehammer, which accentuates a little more significantly the certainty of a reflector of interest. For the seismic profiles linked to receiver number 26 and 9 (Fig. 18B), from the longitudinal and transversal sections of the site 6, the data linked to the vibroseis are totally illegible. On the profile of receiver number 26, traces appear beyond the refracted wave, which is

inconsistent with what can be observed on a seismic profile. On the profile of receiver number 9, a surface or refraction wave trace appears in an illogical geometric form with an unsuitable angle. Parameter setting or writing errors, related to measurements or processing, could be the cause of this incoherence. There are still very fine and imprecise reflection traces, in the seismic profiles linked to sledgehammer (Fig. 18B), but they are close to what has been observed previously (Fig. 18A). All the sledgehammer profiles represented allow a completely satisfactory observation of the refracted waves (green arrows), mainly the profiles linked to the sources (Fig. 18A), which are much sharper, in relation to the transversal profiles of the vibroseis, where discordant reflection traces can be observed before the refracted wave. The results obtained allowed the visual detection of potential reflectors. These observations are positive in the context of seismic refraction and the study of the glacier near-surface.
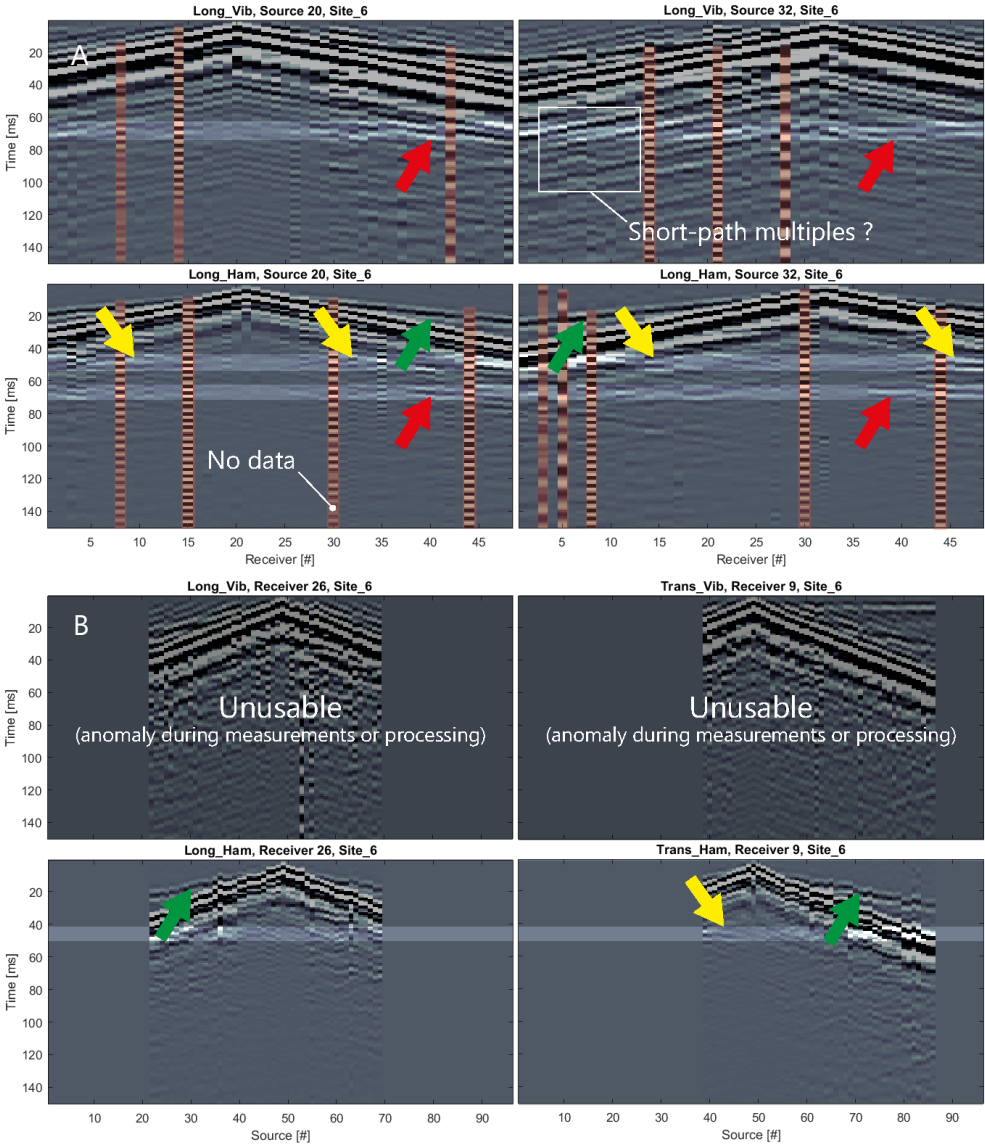
Figure 18. Source and receiver representations from the site 6 data set

Transversal (Trans_) and longitudinal (Long_) seismic profiles comparison, between ElViS (Vib_) and sledgehammer (Ham_), related to source (A) and receiver (B) representations. The yellow arrows represent potential reflectors at around 40 ms and the red arrows represent potential reflectors at around 70 ms. The green arrows represent refraction waves. The vertical lines on a transparent red background represent no data. On a black background, parts of the profile without interesting or unusable traces. These data depend on the relationship between the time (ms) and the source number (#).

On the whole, with regard to the representations of site 6 (Fig. 18), there are too many gaps in terms of the resolution and amplitude of the traces, as well as in terms of presence of noises. The profiles show too few traces that can be sufficiently exploited for constructive seismic reflection processing.

Some perceptible defects on the profiles (Fig. 18A), resulting from difficulties in permanently stabilising the geophones during measurements on the glacier surface, are visible as "no data" (in red). They are visible by a vertical succession of traces of varying amplitude (in black and white). Furthermore, as the depth of such a seismic source, such as ElViS, is usually more than one wavelength below the glacier surface, short-path multiples are commonly present in the data recorded (Polom et al., 2014). In the context of this study, we could suggest the possibility that these shapes are also present on seismic profiles related to vibroseis. They form like multiples parallel to the direct wavelet.

4.2.3. NMO and CDPs stacking processing

CDP stacking attenuates coherent noise such and improve overall data quality, because the reflected signal and coherent noise generally have different stacking velocity. The representations of the NMO velocities (Fig. 19A), that have been tested and parameterised, are proposed, with his representation in the form of a CDPs stack (Fig. 19B), to visualise of the gross contribution of the NMO velocities.

The velocities are too low, at 1000, 2000 and 2400 m/s. At 1000 m/s, it is only possible to observe the top of the direct wavelet (Fig. 19A), which is insufficient if potential reflectors, at a travel time of more than 50 ms, are to be observed more precisely. At 2000 m/s, two potentials reflectors appear (Fig. 19B) between 70 to 100 ms, at distances between approx. 4 to 40 m and approx. 60 to 85 m. However, the horizontality of the traces is not completely acquired at this velocity (Fig. 19A). At 2400 m/s, the two previously observed potentials reflector appear slightly more visible and seem to converge more horizontally from each other (Fig. 19B). The advantage of this velocity (2400 m/s) is that it does not let the impact of the energy, released by the direct wavelet, to influence the legibility of the profile (Fig. 19B), making it more comfortable. Nevertheless, the horizontality of the traces is not yet fully acquired at this velocity (Fig. 19A).

At 3300 m/s, all the criteria proposed by Henry (1997) and Verney (2009) seem to be met. The potential reflector, observed in previous NMO velocity representations, is located (Fig 21B) at a travel time between approx. 80 to 100 ms and at a distance between approx. 5 to 90 m. Note the impact of the energy of the direct wavelet on the stack, which increases a little more at 4000 m/s (performed but not shown), as well as at 5000 m/s, where any observation of the CDPs stack is much more uncomfortable. NMO velocities between 2400 to 5000 m/s, offering relatively good legibility, could also have been used as an NMO velocity parameter in the further processing.

However, the NMO velocity of 3300 m/s was chosen because it remains balanced and favours a good compromise between reducing the amplitudes of the traces, linked to the energetic influence of wave propagation in the glacier, at the approach of the direct wavelet (over the first 100 milliseconds), and maintaining a clear and precise visualisation of the reflector that can be observed.
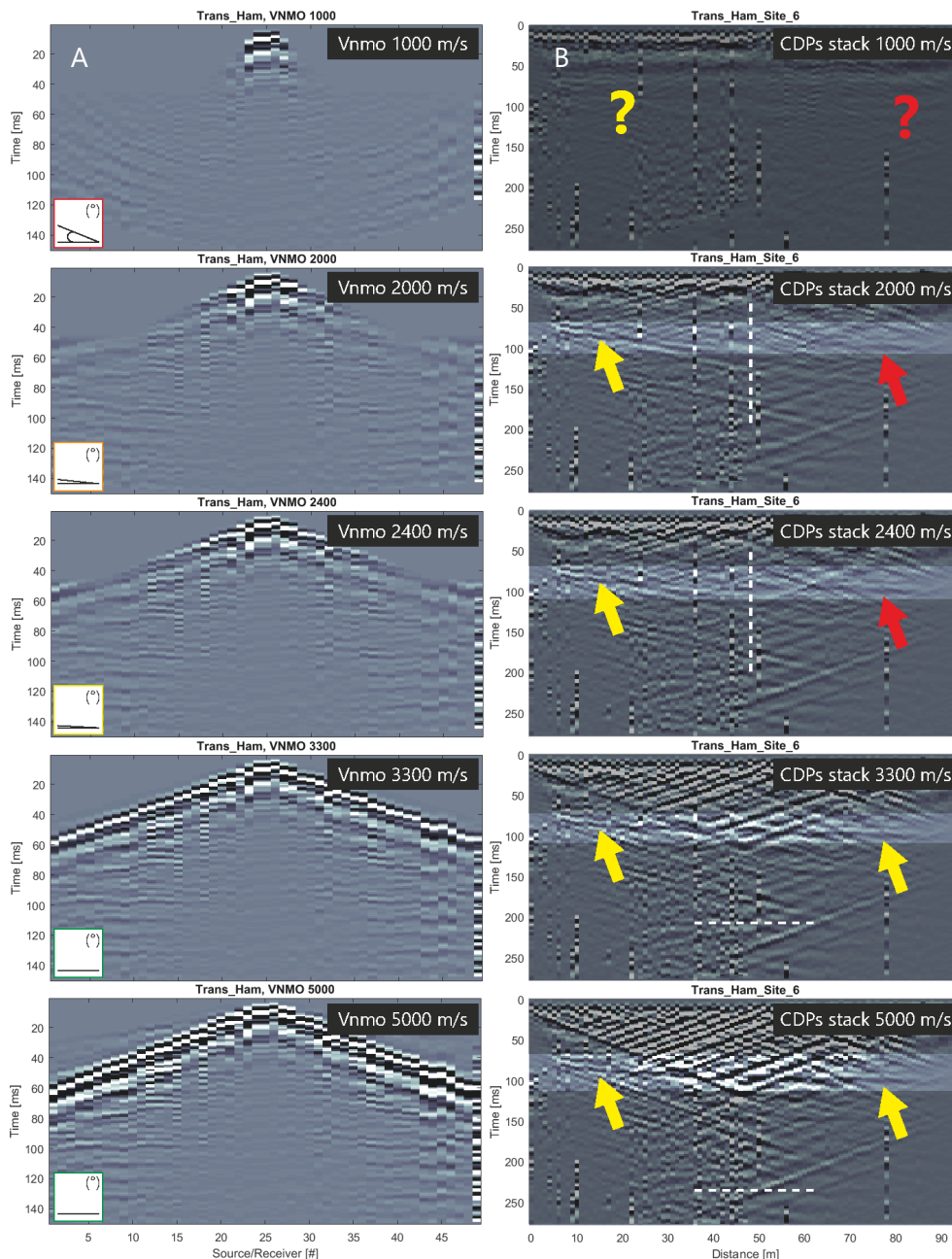
Figure 19*. **CDPs representations and stacking, with different NMO velocity, from the transversal section at site 6***
Transversal profiles (Trans_) presentation linked to the sledgehammer (Ham_), having undergone NMO correction, and CDPs stacking (B) for a selected NMO velocity (Vnmo; A), for comparative purposes in terms of traces legibility on the stacks. The NMO velocity represented are 1000 m/s, 2000 m/s, 2400 m/s, 3300 m/s and 5000 m/s. The frame in the lower left-hand corner (A) represents the quality of the curvature of the traces observed, from red (not usable) to green (usable). The yellow and red arrows (B) represent observable reflectors as a function of the NMO velocity shown: these are separately distinguishable (vertical white dotted line), then commonly distinguishable (horizontal white dotted line), or indistinguishable (question marks). The CDPs profiles depend on the relationship between time (ms), and source (#) and receiver number (#). For CDP stacks, it is a function of the distance (m).

The CDP stacks performed (Fig. 20) at the processing end confirm the results are not sufficient to perform an AVA analysis. First of all, the two stacked CDPs, representing the longitudinal section, all sites combined, are unusable and will not be evoked afterwards. For the transversal section, the vibroseis profiles, all sites combined, are not conclusive in terms of seismic reflection quality. The CDPs stack of the vibroseis (Fig. 20A) shows a marked intensity of the trace amplitude, mainly over travel times of less than 120 ms. This phenomenon thus covers potential reflectors, diminishing the possibility of concrete

observation of the representation and thus limiting any analysis. The CDPs stack of the sledgehammer is much more conclusive (Fig. 20B). As explained above, a good reflector is observable at a travel time from approx. 80 to 100 ms over a distance from approx. 5 to 90 m.
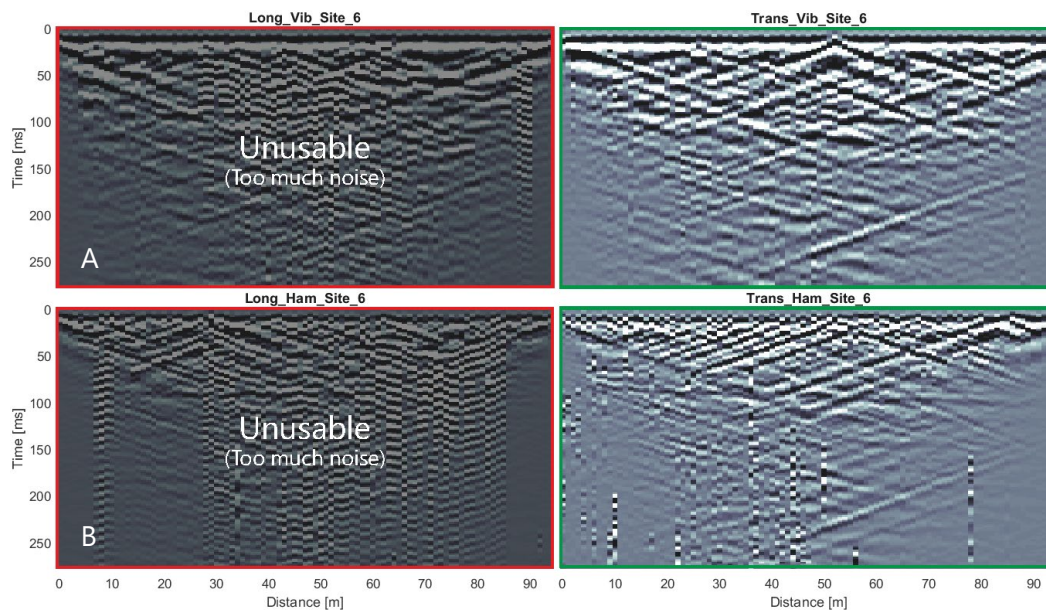
Figure 20. CDPs stacking, from the site 6 data set
Transversal (Trans_), as well as longitudinal (Long_) seismic profiles representation, between ElViS (Vib_) and sledgehammer (Ham_), with a complete gain correction (100), 70 to 250 Hz filter frequency range and 3300 m/s NMO velocity. The CDPs stacks is the relationship between time (ms) and the distance (m). The "unusable" data for the longitudinal stack (red box) could not be analysed contrarily to the transversal stack (green box). Only the data of the transversal section will be presented and discussed.

The direct wavelet amplitudes, present on the stack surface (Fig. 20), are different between the two sources, being more marked for the ElViS. It is possible to identify traces stacked on the surface, like a rolling form on the ice surface. For these two sources, the probable presence of diffractions is quite recurrent. Typically, diffraction refers to the spatial distribution of seismic wave intensity resulting from the presence of a topographic feature (Liu, 2011). The stacks at site 6, as for all the stacked sites (App. 3 to 7), also show this omnipresent type of event in the seismic profiles.

However, despite the reflective quality of the observed reflector, there is still far too much noises (diffractions and noises) over the first 120 milliseconds. Since the probability of analysing reflectors of interest for this study is most likely to be in this range of travel time, any further process and analysis seems complicated to perform with these data. The AVA analysis is therefore not a reliable step to perform with regard to the CDP stack representations.

4.3.   Results from near-surface refraction processing

4.3.1.   Processing: the geometry, normalisation and picking steps

For seismic refraction, only sledgehammer data was used. A global view of the selections was made (Fig. 21 and 22), in order to limit interpretation errors as to the first arrival real time of the refracted wave, and to favour the visual legibility of the proposed seismic profile. The representation of the inverted

shape of the picked refracted wave (A) corresponds to the picking carried out on the seismic profiles linked to the receivers (D). Seismic profiles, linked to the source (C), complete picking work. A graph related to the apparent velocity (B) is also proposed and defined by an indicator between 0 and 1. The 0 value shows a wave front velocity closest, and the 1 value furthest, from the geophone network. It is essential to play on these graphs to have a balanced and plausible picking between the observations linked to the sources and those linked to the receivers. The representations of the seismic profiles for the source 40 and receiver 10 situation, definable by the cross visible on them, was carried out to compare purposes between the sites 4 and 6 longitudinal (Fig. 21) and transversal (Fig. 22) section.
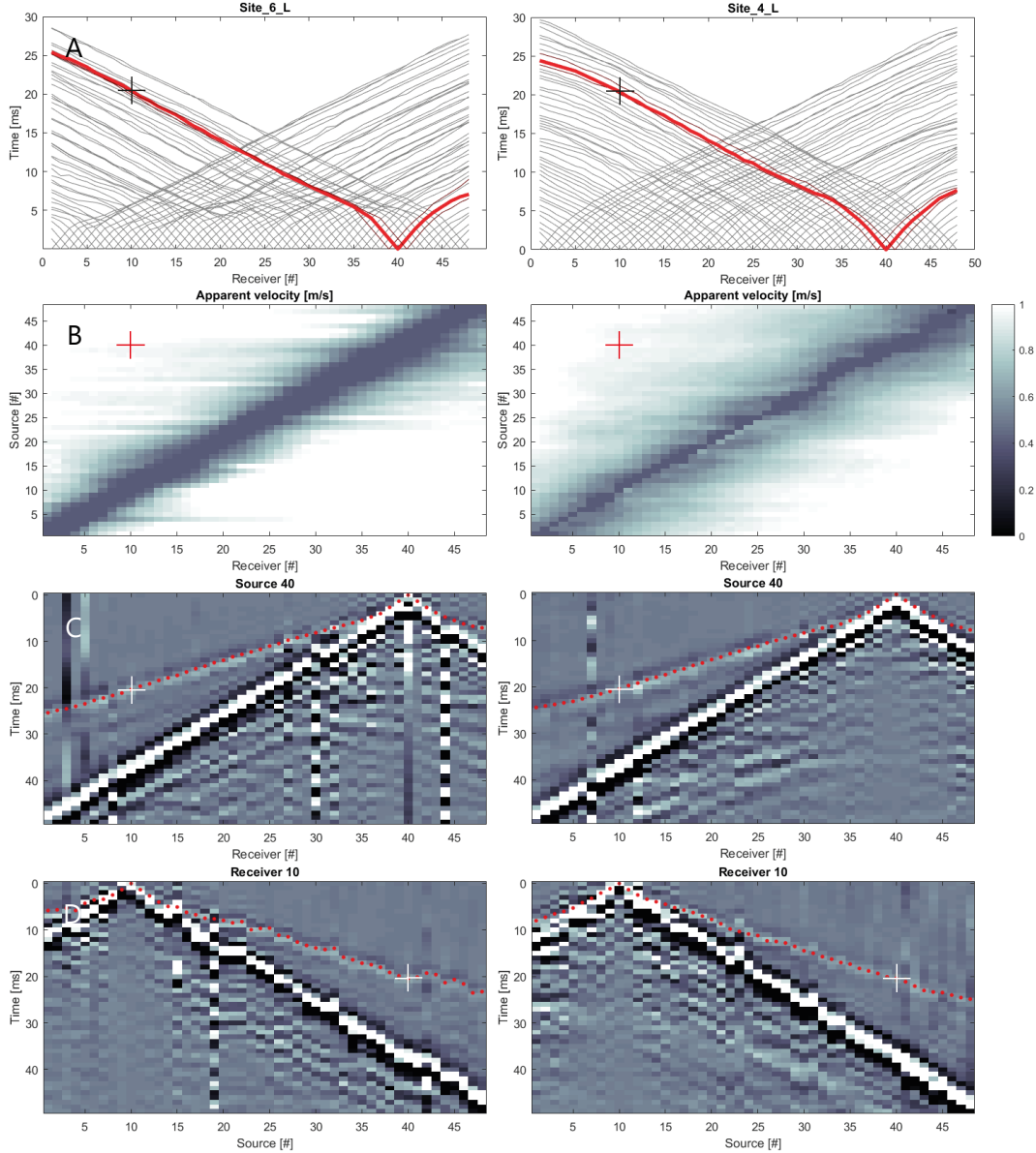
Figure 21. First arrivals picking for the longitudinal sections from the site 6 and 4
Comparison of graphic representations useful at the first arrivals picking step for the longitudinal sections, between site 6 and 4. Four parameters have been taken into consideration: (A) the inverted shape of the picked refracted wave, from the picking linked to the receiver 10, as a function of arrival time inversed (ms); (B) the apparent velocity (m/s) between the sources and receivers, represented by an indicator between 0 and 1; (C) the source 40 and (D) the receiver 10, as a function of the travel time (ms). The curve in red (A) represents the picked first arrivals of receiver 10. The crosses represent the spatial situation for source 40 in relation to receiver 10. The red dots represent the first arrivals (C and D).
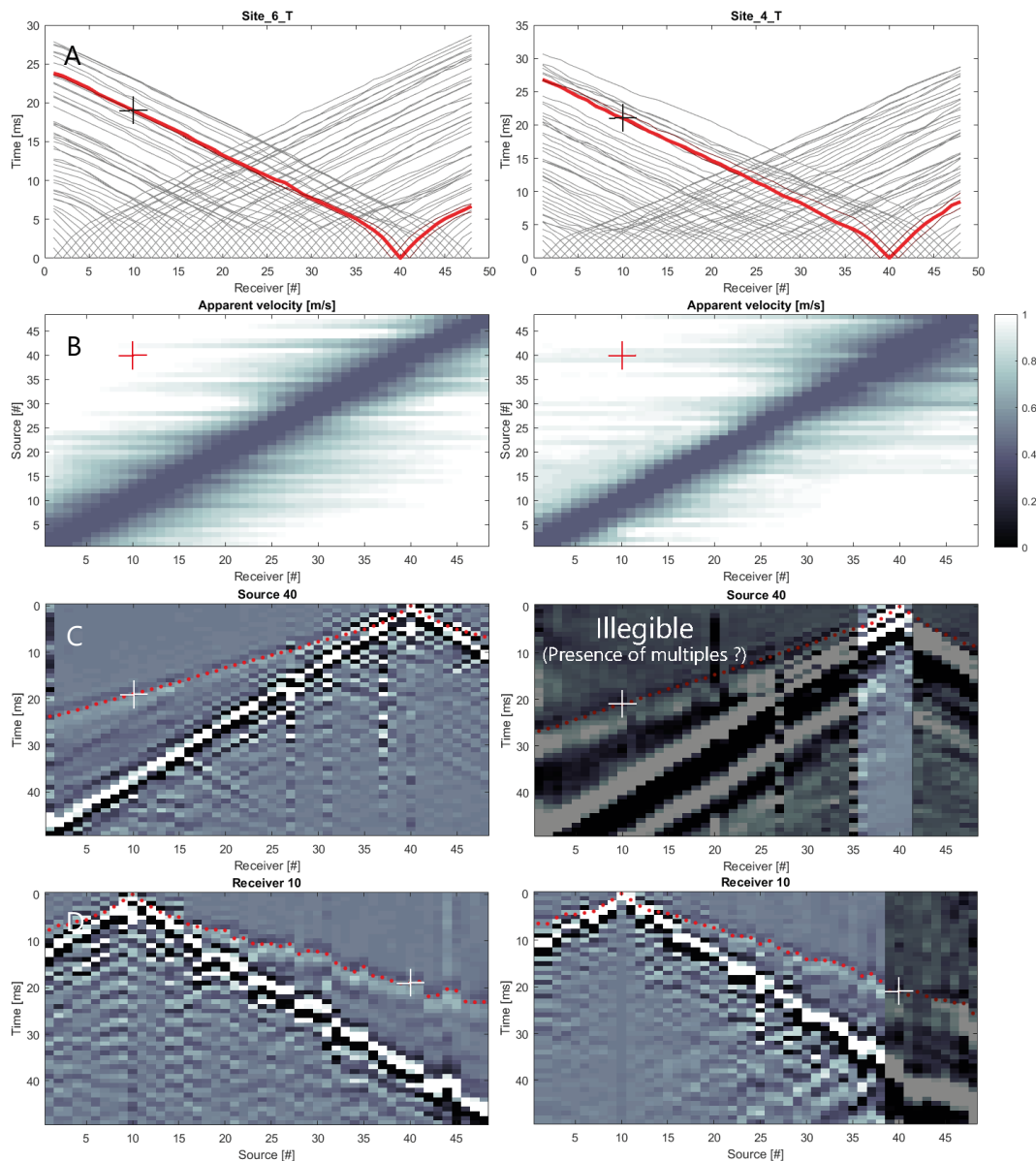
Figure 22. First arrivals picking step for the transversal section from the site 6 and 4

Comparison of graphic representations useful at the first arrivals picking step for the transversal sections, between site 6 and 4. Four parameters have been taken into consideration: (A) the inverted shape of the picked refracted wave, from the picking linked to the receiver 10, as a function of arrival time inversed (ms); (B) the apparent velocity (m/s), between the sources and receivers, represented by an indicator between 0 and 1; (C) the source 40 and (D) the receiver 10, as a function of the travel time (ms). The curve in red (A) represents the picked first arrivals of receiver 10. The crosses represent the spatial situation for source 40 in relation to receiver 10. The red dots represent the first arrivals (C and D). On a black background, parts of the profile illegible.

For the longitudinal section (Fig. 21), the red curves for the first arrivals (Fig. 21A) appear to be much more scattered, less regular and flatter at around 5 ms travel times, with slightly shorter travel times in general for site 6, than for site 4. As for the apparent velocity (Fig. 21B), the contrast is much more pronounced at two levels: (1) the velocities reflecting a certain proximity between source and receiver, either equal or close to 0, are more scattered at site 6 than at site 4; (2) there remains a much more balanced progression of velocity at site 4 than at site 6, along the first arrivals. As far as the seismic profiles are concerned, there is no marked difference between the two sites, and the refraction waves are still quite acceptable and satisfactory for picking. Only the refracted arrivals, observable on the profiles linked to the receivers (Fig. 21D), were more difficult to pick because the first arrivals were often

less legible and more disparate than on the profiles linked to the sources (Fig. 21C). As far as the sites 4 and 6 transversal section are concerned (Fig. 22), the findings that can be made are the opposite of what was highlighted previously. The graphs in relation to the first arrival curves (Fig. 22A) and the apparent velocities (Fig. 22B), seem to be relatively similar to each other and fairly close to the observations made for the longitudinal section at site 6 (Fig. 21). The two notable differences are mainly related to (1) a slightly higher first arrival curves travel time for site 4 (Fig. 22A) and (2) a more apparent velocities progression balanced for site 6 (Fig. 22B). The most striking differences are representative of most of the data available for this work and are clearly visible in site 4 (Fig. 22C and D). The seismic profiles of the transversal section at site 4 are very poorly legible with the constant noises, and in particularly, the probable presence of multiples, which influences the precision of the potential first arrivals sampling.

4.3.2. Travel time tomographic inversion step processing

The plots represent the slowness model (A), showing the inverted velocity model (m/s), and the raypath density (B), showing the times number for each cell in the model was hit by a ray (#), for the longitudinal (L) and transversal (T) profiles at site 4 (Fig. 23) and site 6 (Fig. 24). When there are no raypaths passing through certain areas, close to 0, these areas are called "no raypaths area". They are a consequence of the ray tracing through the velocity model. The raypath hit density highlights the iterations number (25), as does the slowness model, also offers the root-mean-square travel time residual (RMS residual). It represents the RMS error between the observed vector, with picked first arrival travel times, and the predicted vector of first arrival times, based on numerical modeling through the inverted velocity model, for a specific iteration (25th). The more this travel time tends towards 0, the better the accuracy of the model.

The results from site 4 (Fig. 23) are quite acceptable, despite the presence of "no raypaths area" (Fig. 23B) on the transversal section (T) between 60 to 75 m and 80 to 96 m distance. Only a few "no data" cells remain on the two sections (Fig. 23A). The maximum depth of the travel time tomography is between 5 to 6 m deep. A gradual increase (Fig. 23A) in represented velocity, going deeper between the interfaces, can be distinguished on two distinct levels: (1) the upper, between the surface (0 m) and 2 to 3 m deep, with velocities between approx. 1800 to 2700 m/s; (2) the lower, between 2 to 3 m and 5 to 6 m deep, with velocities between approx. 2700 m/s to 3800 m/s. Note, well demarcated concentration of inverted velocity cells of the same value ("streaks") at the upper level of the section (Fig. 23A), with velocities between approx. 1400 to 1700 m/s, as well as at the lower level, with velocities close to 4000 m/s. These "streaks" are very common and represent artefacts. In the tomographic images, they are aligned with the rays that were traced in the imaging procedure. The slowness model graphs (Fig. 23A), for le 25th iteration, are at about ±0.44 ms residual RMS for the longitudinal profile (L), and about ±0.54 ms for the transversal profile (T), which is satisfactory. The graphs related to raypath hit density (Fig. 23B) clearly show a higher raypath density at a 4 m deep for the longitudinal profile (L) and between 3 to 5 m deep for the transversal profile (T), at the raypaths propagation base level. A visible difference in depth at the raypath base (in yellowish colour), going between 4 to 6 m deep, appears on 36 m (between 60 to 96 m distance) on the right part of the transversal section (T).
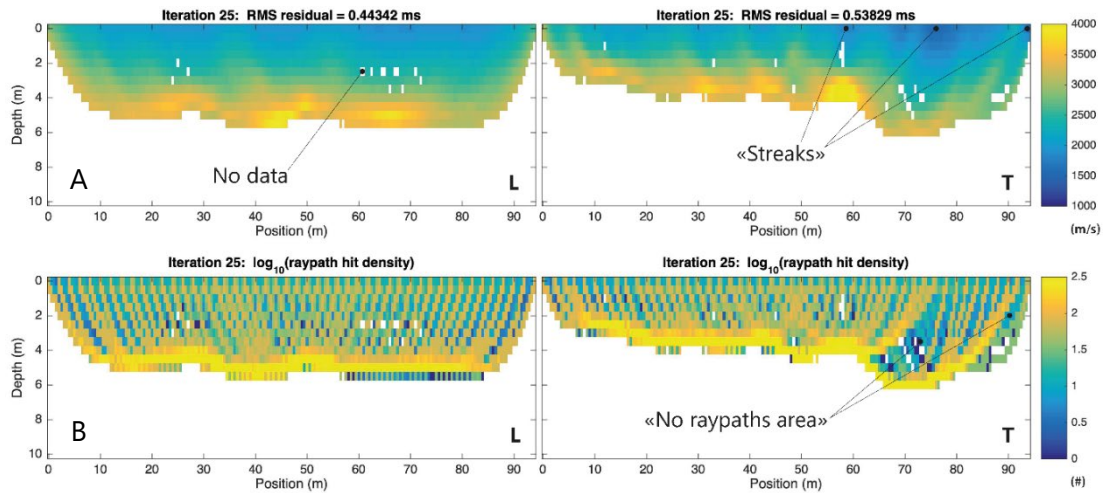
Figure 23. Travel time tomographic inversion for the site 4
Representation of the 25th iteration of the slowness model (A), showing modelled inverted velocities (m/s) and raypaths hit density (B), showing the times number each cell in the model was touched by a ray (#), for site 4 longitudinal (L) and transversal (T) profiles.

Site 6 (Fig. 24) show marked "no raypaths area" (Fig. 24B) on both sections, between 80 to 96 m distance on the longitudinal section (L), and between 75 to 96 m distance on transversal profiles (T), but less for the longitudinal profile (L). The maximum depth of the travel time tomography is between 3 to 5 m deep. Like site 4, a gradual increase (Fig. 24A) in the represented velocities as you go deeper, with two distinct levels also observable: (1) the upper, between the surface (0 m) and 2 to 3 m deep, with velocities between approx. 1900 to 2700 m/s; (2) the lower, between 2 to 3 m and 4 to 5 m deep, with velocities between approx. 2700 to 3700 m/s. The "streaks" at the upper level of the profile have velocities between approx. 1500 to 1800 m/s, and at the lower, close to 3800 m/s. The slowness model graphs (Fig. 24A), for the 25th iteration, are at about ±0.69 ms residual RMS for the longitudinal profile (L), and about ±0.60 ms for the transversal profile (T), this which is less satisfactory than for site 4. The graphs relating to raypath hit density (Fig. 24B) include a higher raypath density at 3 to 4 m deep for the longitudinal profile (L) and around 4 m for the transversal profile (T), at the raypaths propagation base level.
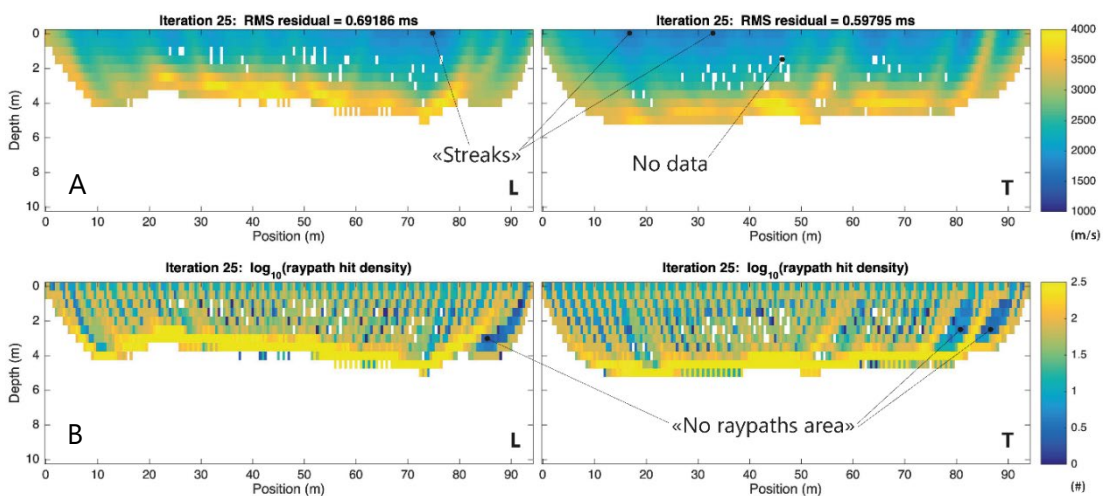
Figure 24. Travel time tomographic inversion for the site 6
Representation of the 25th iteration of the slowness model (A), showing modelled inverted velocities (m/s) and raypaths hit density (B), showing the times number each cell in the model was touched by a ray (#), for site 6 longitudinal (L) and transversal (T) profiles.

5. Discussion

In this discussion, we will address observations and criticisms about this work, but also strategies for future projects related to the active seismic field in glaciological environments. First, we will discuss the field data collection related to measurements and the limits related to the Alpine and glaciological environment studied. Second, we will highlight the data collected limits in the field and the seismic data processing phase. Third, we will evoke opportunities and potential for near-surface refraction study.

5.1. Data quality

Despite a rigorously executed field methodology, reflection processing did not prove to be conclusive compared to what refraction processing could bring. The first refraction P-wave arrivals are satisfactory (Fig. 25), with a relatively precise legibility for all sites. The observation and analysis of these refracted waves, during the phase of the reflective process, made it possible to glimpse the possibility of analysing the near-surface part of the Glacier d'Otemma.
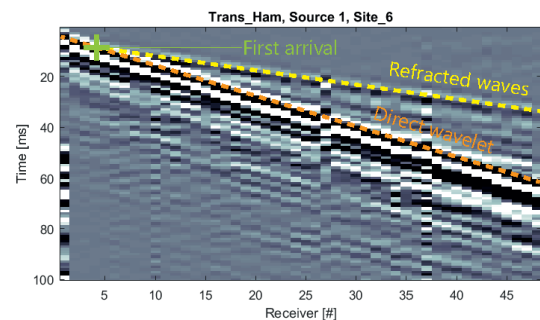
Figure 25. Seismic profile characteristic
First arrival (in green) represents the junction between the refracted wave (in yellow) with the direct wavelet (in red).
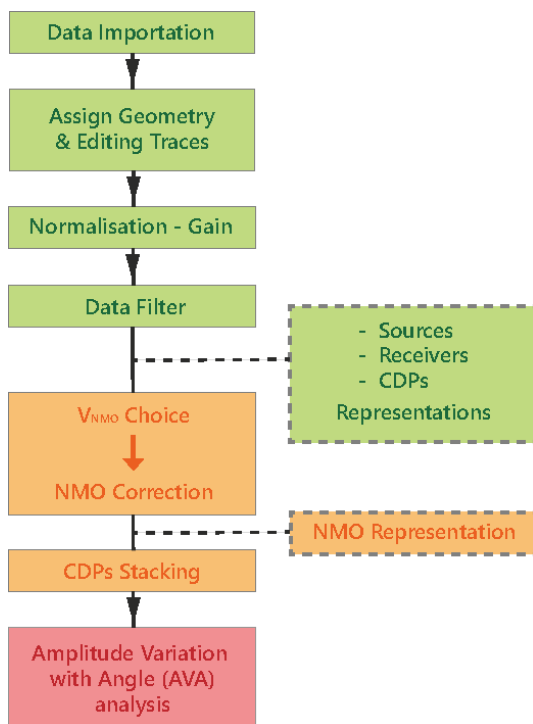
Figure 26. Reflection processing workflow results
The diagram describes the reflection processing workflow results. Solid line frames are main processing steps and dashed line frames are secondary steps for data analysis. The steps in green correspond to the steps successful, in orange, the steps worked but with some difficulties or approximations, and in red, the steps that did not work.

For the reflection processing workflow (Fig. 26), on site 6, the final steps did not work to meet expectations, compromising the success of the processing. The *Assign Geometry & editing traces*, the *Normalisation – Gain* and *Data Filter* (Fig. 26) were successful in its implementation. The data could be parameterised without technical problems and the code proposed by the CREWES showed a satisfactory efficiency. The gain correction, with 100 indicator, was naturally the most suitable standard value and the 70 to 250 Hz frequency range of the data filter proved to be balanced between the sharpness of the observed traces and the presence of noise on the seismic profiles. The *CDP representations* showed the presence of partially visible reflectors, but nevertheless insufficient to be exploitable in later steps. Although the processing functioned satisfactorily during the *NMO Correction* and the *CDPs Stacking* (Fig. 26), it did not prove to be constructive because the presence of noises in the first 100 milliseconds made it difficult to make any observations, making *AVA analysis* (Fig. 26) impractical. The data resolution is not satisfactory for a potential

reflector's analysis. The deconvolution and migration steps has not been carried out because the stacked traces are not satisfactory enough and the migration tends to further reduce more the quality of these traces (Mari, 2002).
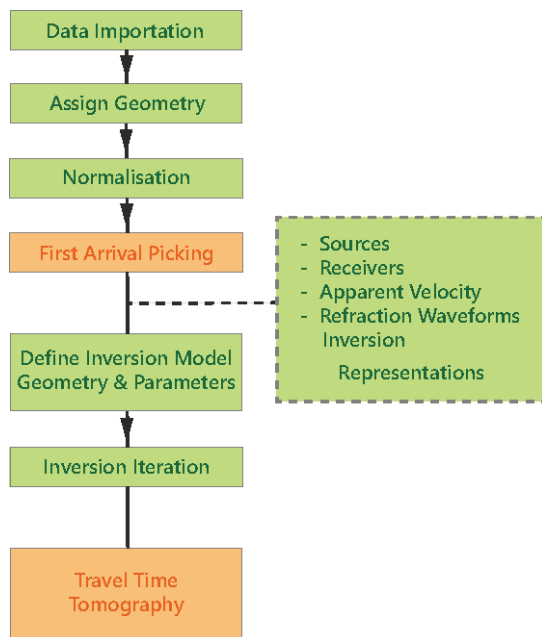
Figure 27. Near-surface refraction processing workflow results

The diagram describes the refraction processing workflow results. Solid line frames are main processing steps and dashed line frames are secondary steps for data analysis. The steps in green correspond to the steps successful and, in orange, the steps worked but with some difficulties or approximations.

The near-surface refraction processing (Fig. 27) was carried out on sites 4 and 6 and involves a construction of the travel time tomography. Each processing step has proven to be productive and constructive in terms of results. Even if some profiles are difficult to read, the refraction processing allowed observation of marked velocity differences on the travel time tomography, facilitating the interpretations concerning the near-surface ice properties. The *Assign Geometry* and *Normalisation* (Fig. 27) was successful. Complementary applications allowing a global view of the selections with the representations of the inverted shape of the picked refracted wave (*Refraction Waveforms Inversion*), seismic profiles of the sources and receivers, and the apparent velocity, have been beneficial for performing the picking on the refracted waves. *First Arrival Picking* (Fig. 27) was subject to possible errors and inaccuracies but was a constructive step. The characteristic linear shape of first arrivals may be misleading because the human eye with a tendency has worked in this direction. Despite good filtering, first low-energy amplitude arrivals have variable waveforms compared to other traces present in the processed data. In the steps, *Define Inversion Model Geometry & Parameters,* and *Inversion Iteration* (Fig. 27), the code proposed by James Irving and Ludovic Baron was also a success and made it possible to go to the last step of the processing. *Travel time Tomography* worked relatively well, but uncertainties about picking accuracy could call into question the reliability of this final stage.

5.2. Global limits

The active seismic method is still an effective geophysical investigation method, but it has its limitations, which can be seen in the field as well as during processing. The melting season was probably not a suitable period for seismic measurements on the ablation zone of an Alpine temperate glacier. The ice temperature at this period of the year is close to or above the melting point, favouring the presence of meltwater in the entire glacier structure. Observations made during the processing have shown that the data quality are affected by noise from wave backscattering caused by the presence of subglacial or englacial conduits, crevasses, active glacial moulins or supra glacial channels too close to the measurement area. These physical phenomena can interfere with the use of the source, the methodology and the data processing.

5.3. Limitations related to the measurements

Field measurements were effective, much more than expected. On site 1, for the parameterisation of the ElViS, an attempt to emit 30 to 360 Hz frequency range was tested, but without being convincing. This tested frequency range did not facilitate pre-analysed data legibility on the acquisition computer. For this reason, the frequency range chosen was from 20 to 240 Hz. The number of sites measured, and therefore the data available for the glacier area studied, remains significant. Few technical problems were noted, which made the measurements straightforward. However, some constraints have been identified, some of which could be avoided, mainly through technical and technological improvement.

With regard to the actual practice of this method on the ice, the period of the day when the measurements are made must not be ignored. If the glacier surface is smooth and/or slippery, incised and/or irregular, with supraglacial forms, may have a significant influence on the vibroseis handling. The source weight and handling were a challenge, but its effectiveness even as a measuring source during shooting is undisputed, with regard to the reference and recent studies (Diez et al., 2013; Polom et al., 2014; Smith et al., in press). Measurements were preferred in the morning, in order to have an ice surface with little influence of melt and heat flow, as well as to have satisfactory visual conditions. The surface close to night-time conditions, without surface water flow, was ideal for measurements with vibroseis, in order to limit natural ambient noise. The presence of long-range lighting could have been the solution, but with such energy-intensive equipment, the installed generators would have created seismic waves, which would probably have influenced the measured data.

The vibroseis has proved to be a low-complexity source in terms of use, as there are few manipulations to be carried out and the equipment making up the device is few in number, making it possible to remedy a technical failure effectively. Due to its weight (130 kg), restricted mobility and the geographical location of the field, a source such as this requires motorised and air transport. The difficulty of mobilising the source efficiently, as well as for additional weight (equivalent to a human), in order to have an optimal *vibrator pot* adherence on the ice during the vibration, adds an additional dependence in terms of manpower. The wheelbarrow system is not practical on frozen or snowy, smooth, and sloping surfaces, and by its weight, it could be dangerous to handle in fall case. Smith et al. (in press), during the field measurements, was modified the ElViS to be adapted to a snow-covered surface. They had installed a blade at the front to spread the snow and a central skid to slide more easily, instead of the wheel, reducing the effort required to push the vibrator source.

During sledgehammer measurements, the ice surface was ideal for this source. Indeed, an ice surface compact and smooth remained a constraint, as the repeated bouncing of the plate against the ice meant that the shots had to be repeated on the same geophone, favouring late measures. Ice, that deforms under the mass weight during the shot, causes the plate to sink into the ice at the impact time, reducing the rebounds and number of shots. The recording of a single shot per geophone was sufficient. Unlike vibroseis, it would be possible to do the measurements alone with the sledgehammer, because it is possible to move between the shot area and the laboratory, in order to analyse the shot results on the acquisition computer. However, the presence of an assistant is therefore necessary to be more efficient.

This source is ideal for cryoseismologic research because it is simple to use, does not need a battery (therefore no energy recharge), is easily transported, and remains logistically more straightforward. A resume of the limits in the use of the ElViS and sledgehammer on an Alpine temperate glacier ablation zone is proposed (Table 3).

Table 3. Resume of the limits in the use of the ElViS and sledgehammer on an ablation zone of an Alpine temperate glacier
Two measurement sources used (ElViS and Sledgehammer) were compared in terms of (1) ease of use, (2) their effectiveness in the field, (3) the logistics involved, and (4) their mobility. The green colour shows ease with many advantages; the orange colour shows relative ease with some disadvantages; the red colour shows difficulties symbolised by many disadvantages.

	ElViS	Sledgehammer
Use	🟩	🟩
Efficiency	🟩	🟧
Logistics	🟥	🟩
Mobility	🟥	🟩

The results showed the probable presence of multiples, which are probably due to the plate rebounds on the ice surface. In the case of the sledgehammer, these bounces can be detected during visualisations on the acquisition computer. The measurements can be repeated if the measured shot was insufficient. For the vibroseis, the observation of these noises directly on the acquisition computer is difficult, because these bounces are probably finer, with time intervals too short to be perceived before data processing. This remains hypothetical, but could justify the multiples presence, much more visible via the seismic profiles of the ElViS.

The C*ross-spread* system methods performed well and remain promising in seismic analysis. However, the system proved to be long to set up, with constraints during the field, and uses a lot of energy. The geodes, the *trigger*, the acquisition computer and especially the vibroseis, are large energy consumers. The use of conventional external batteries proved to be inefficient in the long term. Mainly due to the cold and humidity, the batteries tend to have a shorter lifespan as they are used, discharging quicker. In addition, it was impossible to recharge the external batteries during the measurements because of vibrations. A more autonomous solar energy system connected directly to the battery would be a real benefit in increasing the measurement productivity and efficiency.
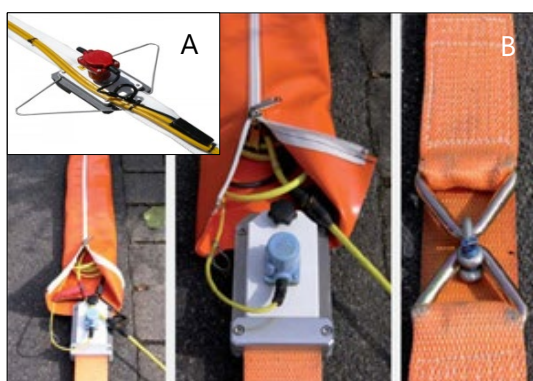
Figure 28. "Geophon-plates"
The pictures show a geophone mounted on a flat metal bracket (A), which can be supported by straps and can be fitted with a "cable bag with end-to-end zip" to protect it from the frost and cold (B).
Source: *Geosym GmbH®, 2019.*

The geophone efficiency on the glacier depends on their stability on the ice. Geophone destabilisation, on the ice surface can cause measurement absences ("no data") on some geophones. It was observed that night-time temperatures could have an influence on measurement timings. At night, when the surface temperature was close to or above the melting point, the ice did not crystallize sufficiently to stabilise geophones in the ice. Even with favourable weather conditions allowing measurements to be carried out theoretically without hindrance, the melting on the glacier surface greatly affects the stability of these sources on the ice for the duration of the measurements. In the field, the material used were assembled and disassembled for each measurement site, which was time-consuming. In a glaciological context, it is probably advisable to upgrade the seismic equipment in order to increase

their efficiency during measurements. Pedestal geophones with a plate support (Fig. 28A), which can be protected from moisture and frost by impermeable covers (Fig. 28B), could be interesting in terms of time saving, as well as ease of installation and protection. A bluetooth system is an interesting compromise in the future to limit the restrictive use of cables.

5.4.   Limitations related to the processing

The measures were taken when the glacier surface was melting, which created noises visible on the processed data set, not allowing significant till or bedrock detection in the subglacial glacier part. Thanks to the quality of the refracted waves, it was possible to model the P-wave velocities of the glacier near-surface on two sites in the study area. Why was the quality of the reflection data not satisfactory? Why is there so much uncertainty in the determination of reflectors? Why was it ultimately not possible to determine the till extent? Human, environmental, and technical factors are probably the answers.

Reflection processing has demonstrated challenges in the seismic data set linked to environmental factors. Ambient noise and incomplete geophone recording created trace blurring and/or vertical artefacts in the seismic profiles, covering potential reflectors and rendering the analysis complicated. These noises are mainly due to the perception of acoustic waves, external to the system, captured by the geophones. They can come from water flow in active supra glacial channels and moulins, from fine meltwater runoff on the surface, from wind action at the surface rubbing against the geophones, from precipitation and rainwater contact on the geophones and the glacier surface, or from any other artificial noise outside of the glacier, such as the sliding of a glacier table or landslide, the passage of hikers, planes, or helicopters at low altitude.

Two good reflectors could be identified on CDPs stacking (Fig. 29): (1) on site 4 (red arrows) between approx. 70 ms (at 10 m distance) to 80 ms (at 80 m distance) and (2) on site 6 (yellow arrows) between approx. 80 ms (at 5 m distance) to 100 ms (at 90 m distance). It is difficult to know whether or not these reflectors are related to the reflection of till, bedrock, or deeper geological surfaces. What is interesting, however, is that between these two sites there is about 200 m distance and there is a gap forming like a continuity in the reflection, and those while site 6 is higher than site 4, bringing coherence to these reflectors. In order to be more certain about what these reflectors represent, a more in-depth analysis of the P-wave propagation velocity in the ice and an AVA analysis would be required. Probable diffractions identified (Fig. 29) were recurrent in data processing. They are omnipresent on all the sites and make all trace legible very delicate. The topography of the bed of the Glacier d'Otemma, in this study area, could be sufficiently steep to induce this event in the profile. To a lesser extent, it could be related to the presence of water inclusions, such as water lenses, or glacial channels (Navarro et al., 2005). These features affect influencing the geometric position of reflectors (Murray et al., 2007). Finally, it is also possible to observe large wave amplitudes at the surface of seismic profiles, mainly for the ElViS profiles. This could be a component mainly related to Rayleigh (or pseudo-Rayleigh) type surface waves (Hameg, 2007; Eisen et al., 2015). These high-energy waves are common when vibroseis is used in P-wave prospecting (Polom et al., 2014).
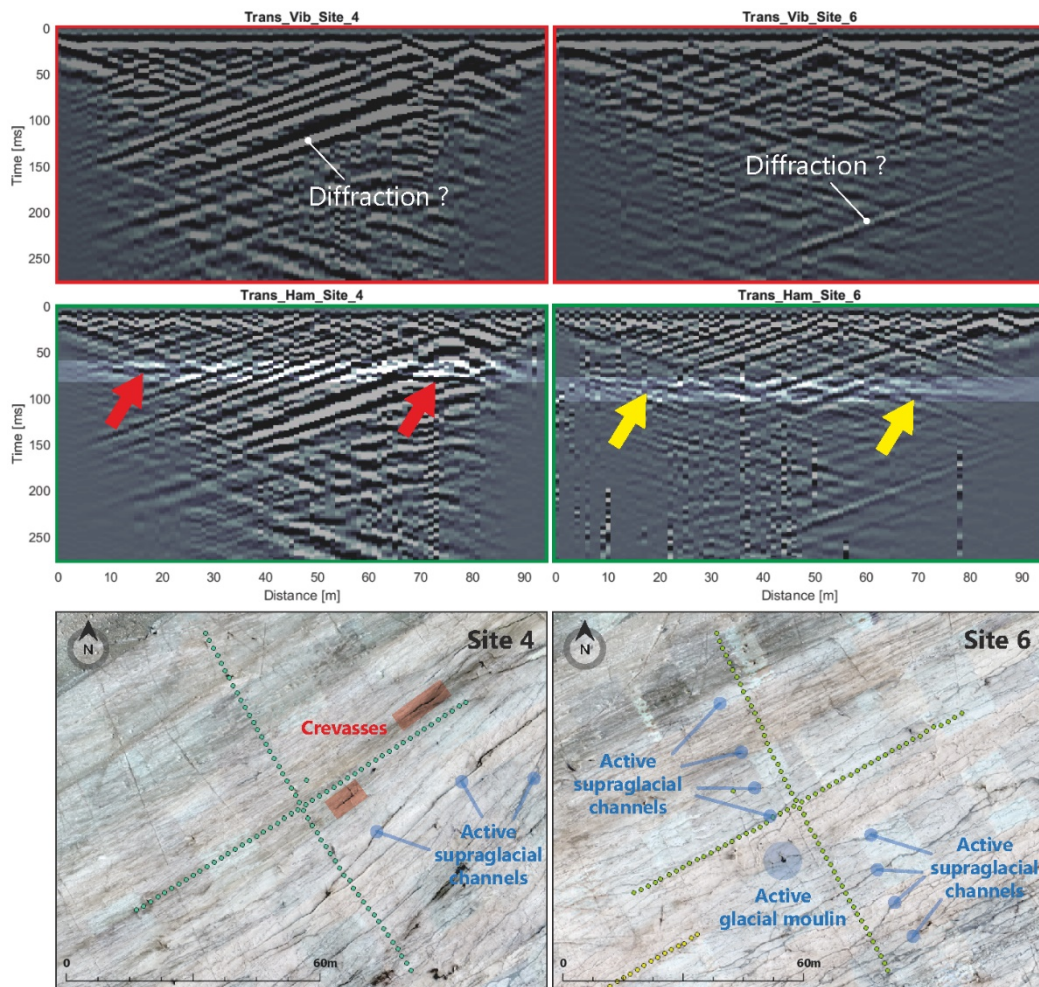
Figure 29. Reflection CDPs stacking from the transversal sections of the site 4 and 6 data set

CDPs stacking representation, showing propagation time (ms) in relation to the distance (m) for the transversal profiles, at site 4 and 6. The black part represents the non-exploitable parts. Stacked diffractions has been indicated, but others remain. The red arrows represent a reflector on site 4 and the yellow arrows a reflector on site 6. Site DEM is proposed with the geophones position during the field measurements, as well as the supra glacial forms present and visible in the field. Not all of these forms are always represented in order to make the content of the image more legible. The vibroseis stacks (red box) could not be analysed in contrast to the sledgehammer stacks (green box). Only the sledgehammer data will be used for refraction processing.

Seismic wave propagation in the ice seems to have a greater amplitude when measured by the ElViS, probably due that this source is stronger than the sledgehammer and perhaps because it does not seem to be adapted to the ice crystal conditions of the glacier. The ice properties probably also interfered with the processed data quality. Seismic data comparison from the Glacier d'Otemma with those from the Colle Gnifetti (Polom et al., 2014), or the Kongsvegen (Smith et al., in press), show many differences in their data. The mineral organisation of the crystal, in the polar glaciers, limits the interstices within the crystals themselves, favouring relative permeability and thus limiting crystal deformation (Raymond & Harrison, 1975; Duval, 1977, 1979, Duval et al., 1983). Quite marked variations in seismic wave propagation rates can be attributed to different types of structural crystal levels within the glacier (Fountain and Walder, 1998; Murray et al., 2000, 2007; Gusmeroli et al., 2008). For temperate glaciers, there are levels where the ice is permeable, undergoing crystalline deformation, with marked laminar percolations. These permeability levels (sometimes called "piezometric" levels), consisting of a water proportion higher than the glacier average water content and a base where the ice is impermeable, allow

water to flow by capillarisation towards larger subglacial channel networks (Fountain and Walder, 1998). These structural variations are highly dependent on the melting season, precipitation, and inflow from outside the glacier.
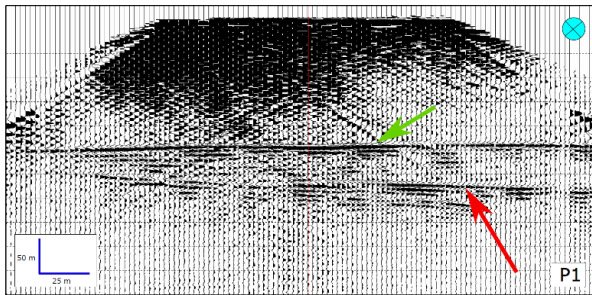
Figure 30. Vibratory power of the ElViS
P-wave reflection seismic section was carried out in April 2019, on the Kongsvegen (Svalbard), using an ElViS. The red arrow represents the glacier bed and in green a probable subglacial sediment package.
Source: *Smith et al., in press.*

Smith et al. (in press) carried out seismic measurements with an ElViS modulated to be adapted to a snow-covered surface. The stacked seismic section (Fig. 30) showed marked P-wave reflections level on the glacier bed at 220 m deep (green arrow) and the reflectors appearance on at 60 m lower, interpreted as subglacial sediment (red arrow). Their parameters used vary in four aspects: (1) 5 m geophone interval, (2) 0.05 ms sample interval, (3) 30 - 360Hz source frequency range, and (4) 10 s sweep recording. These parameters allowed observation of the first hundred meters of reflection amplitudes reflecting the vibratory power potential that ElViS can provide. Given the assumed depth close to 100 m, at the first two sites (site 1 and 2), at the study area's highest point, a longer listening time might have been a better option to hope to detect the bedrock of the glacier.

Human errors cannot be ruled out in the near-surface refraction processing phase, particularly in the picking step. The irregular and wide spacing between some of inverted curve of the picked refracted wave on the two sites (Fig. 21A and 22A) suggests possible error of assessment during picking. Insufficient data resolution does not allow a detailed legibility of reflections on the glacier bed, probably due to an unsuitable frequency range content. To solve this problem, the seismic experiment must be such that sufficient energy can propagate to the glacier bed, be reflected, and propagate back to the surface, assuming that the waves will be attenuated along the way. These faults are attributable to a poor appreciation of the environmental factors and the measurement period, mentioned above. Near-surface refraction processing showed that the picking process step depends on the ability and experience of the picking operator. With this tomographic representation, requiring picking, there may be differences in the interpretation of what is observed by the person carrying out the picking, which may sometimes lead to proposing data that are not always unanimously accepted in terms of selection. The seismic data includes sometimes too much background noise, making the first arrivals selection difficult and unreliable, especially for someone with little experience.

5.5.   Potential for near-surface refraction studies

Refraction data proved to be particularly interesting for the legibility and understanding of ice properties close to the glacier surface dynamics, and more specifically the near-surface ice properties. The results obtained by travel time tomographic inversion (Fig. 31) showed propagation velocities increasing with depth. Two layered-system of velocities can be distinguished through this tomography: (1) between the surface (0 m) to approx. 3 m deep, and (2) between approx. 3 m to 5 m deep. For the upper layer, the

velocities are lower than the reference P-wave propagation velocities for temperate glacier ice, i.e. less than approx. 3500 m/s. For the lower layer, the propagation velocities are within the reference averages, i.e. more than approx. 3500 m/s. As a reminder, our velocity references are based on numerous studies (Paterson, 1981; Cuffey & Paterson, 2010; Kim et al., 2010; Bradford et al., 2013; Christianson et al., 2014; Hofstede et al., 2018) which show average P-wave propagation velocities in temperate glacier ice between 3470 m/s and 3795 m/s. However, the travel time tomography model, such as this one, cannot be subject to interpretations of actual velocities, as represented in this work. Further investigations are necessary to confirm the veracity of such results. We will mainly retain these differentiations in two layered-system from a qualitative point of view.

By observing the site 4 and 6 DEM (Fig. 31), many supraglacial structures (not all represented on the DEM) are visible, numerous, and quite abundant in meltwater (field observations). A natural factor explaining the presence of these "streaks" on the travel time tomography, close to the P-waves propagation velocities in liquid water (i.e. between 1400 and 1600 m/s), seems very unlikely. However, these "streaks" positions coincide quasi-accidentally with the presence of active supraglacial channels, along the geophones of the transversal line on the DEM, which, at first glance, could easily lead to confusion in terms of interpretation, especially for a person with little experience.
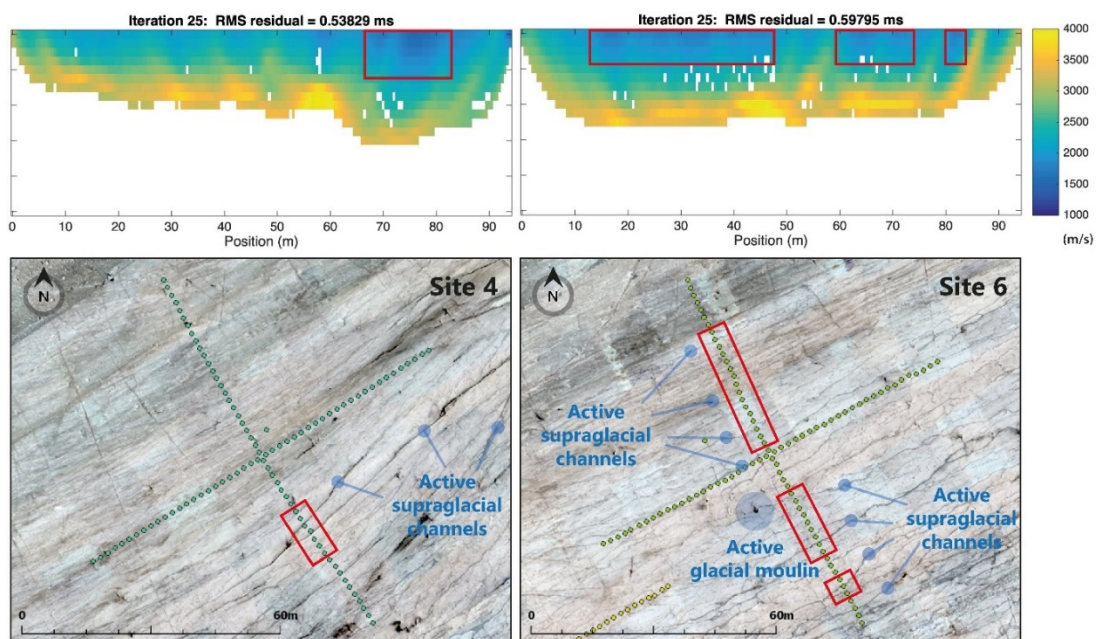
Figure 31. Analysis of the travel time tomographic inversion, from the transversal sections, for sites 4 and 6
Representation of the slowness model 25th iteration, showing modelled inverted velocities (m/s) for the site 4 and 6, from the transversal profiles. The white parts represent no data. The red boxes represent the geophones position in relation to the travel time tomographic inversion. A site DEM is proposed with the geophones position during the field measurements, as well as the surface glaciological forms present and visible in the field. Not all of these forms are always represented in order to make the content of the image more legible.

A temperate glacier can have a water content between 0.1 and 3% (Gusmeroli et al., 2008), up to 4% (Greve & Blatter, 2009; Gusmeroli et al., 2010). Such a high water content on this glacier due to the crystal decohesion by heat transfer, with an ice temperature close to the melting point and a high air content ice, effectively lowers the velocity of propagation of seismic waves (Gusmeroli et al., 2013). The

ice temperature at the near-surface, the crystalline properties in the ice and the near-surface ice low density of a temperate glacier (Diez et al., 2014; Cooper et al., 2017), influence the P-wave propagation velocity at the glacier surface. The most likely hypothesis, in view of the results obtained from the travel time tomographic model, is that the P-wave propagation velocities observed on the glacier surface could indicate a probable variability in the ice properties. It is therefore possible to put forward the idea that this gradual increase in velocity could be due to changes in the ice properties towards the deepest parts of the glacier. The variability in the ice properties of the near-surface could justify these variations in term of velocity, between these two-layered system of velocities, and influence the propagation of P-waves in this part of the glacier. Meltwater laminar percolation/capillarisation, natural phenomenon on the surface of an ablation zone of a temperate glacier during the melting period, does not justify these variation in propagation velocities. It is therefore not possible to state that these variations in propagation velocites are directly related to the meltwater flows impact on the supraglacial dynamics. Moreover, the presence of air in the ice is a much more influential factor than water content, in reducing P-wave propagation velocities. This air content impact on propagation velocities further reinforces the fact that the ice properties is probably a key factor justifying both the weakness, but also variations, in propagation velocities over the first five metres of the glacier near-surface. This statement also justifies how the ice properties may have interacted with the measurements and influenced the reflection data previously carried out and analysed.

Finally, as one goes deeper into the glacier, the ice density increases rapidly in the glacier upper layers due to the progressive air compression included. The ice density is not the only factor that can justify the variation in propagation velocities at the glacier near-surface, but its contribution is not to be neglected. In general, seismic attenuation is minimal when the propagation of the seismic wave is parallel to the primary axis of anisotropy (Best et al., 2007; Chinchinina et al., 2009; Peters et al., 2012). Seismic attenuation has a strong dependence on ice temperature, especially as the attenuation medium approaches its bulk melting point (Peters et al., 2012). Furthermore, with regard to the equation for calculating P-wave velocity (Equ. 3; Schlegel et al., 2019), and without taking into account shear modulus and bulk modulus, low ice density should theoretically increase P-wave velocity. The influence of the value of shear modulus and bulk modulus in the calculation of P-wave velocity cannot therefore be excluded. A decrease in the value of one, or both, of these two moduli, could greatly influence a decrease in the P-wave velocity in the near-surface ice. This would then further justify the low P-wave velocity on the near-surface of the Glacier d'Otemma.

Conclusion

Conclusion
Inevitable disappearance

The Otemma Glacier formed this steep, chiselled, and unstable circular front from the collapse of a subglacial cavity in the summer of 2018.
Boris Ouvry – August 16th, 2019

6. Conclusions

In view of the results obtained in this experiment, the use of a small vibroseis on a glacier, such as the Glacier d'Otemma, showed us that ElViS was probably not adapted for Alpine temperate glaciers, and more specifically their ablations zone. This is due to their ice properties and crystal structure, the proximity to the melting point, and also supra and subglacial meltwater during the melting period, which greatly influences the measurements. Moreover, the seismic survey area and his planning probably played a non-negligible role in these data approximations. It is not impossible to affirm that a similar study on the glacier plateau could have given different and much more conclusive results. It is also likely that measurements during the autumn freeze-up or winter period would have given better results. An interesting approach would have been to also compare the reflection processing results obtained with a simulation modeling, to determine whether the results related to the seismic methods are consistent, and relevant, to the prediction offered by a model. The seismic reflection, via the ElViS, did not meet the first objective of this work, which was to determine the subglacial till present at the tongue of the Glacier d'Otemma. Noises and binding use of this source and inexperience may have reduced the reliability of the seismic reflection data, and thus the difficulty of performing the AVA method as planned. An ultimately simple source, such as the sledgehammer, is quite appropriate and perhaps even the source to be preferred, in comparison with the ElViS. Due to the lack of concrete evidence in this work, it is not possible to assert that the seismic reflection method could detect till cover at bedrock level, thus explaining the influence of subglacial sediment transport mechanisms and the evolution of the subglacial drainage system during the melting season. The seismic refraction, and the results obtained, demonstrated changes in the P-wave propagation velocities as a function of depth, via the travel time tomographic inversion, and to highlight the likely ice properties impact on the P-wave propagation velocity at the near-surface. The identification of two layer systems with variable P-wave propagation velocities was observed, making it possible to assume a probable influence of ice properties on P-wave propagation on the near-surface glacier, in the ablation zone of an Alpine temperate glacier. This conclusion also justifies how the ice properties may have interacted with the measurements and influenced the reflection data. This track could be confirmed by placing high-resolution electronic piezometers on the glacier surface to clearly delineate and identify the density of each layer. Compared to other scientific articles, having carried out glaciological research using active seismic methods, there are applications and conditions that would them reliable, relevant, and appropriate.

Walter et al. (2020) proposes Distributed Acoustic Sensing (DAS) using fibre optics. This innovative method is closely related to passive seismics, as it detects signal disturbances during seismic events (decompressions, falls, various tremors) and could fill certain gaps related to glaciological seismogenic processes. These measurements would have three main advantages: (1) an extension of the seismic acquisition coverage, (2) a better resolution of the data and (3) a greater ease of implementation. Cryoseismology thus remains a field in constant evolution, with ever more innovative technologies making research work more comfortable, constructive, and productive, and perhaps these future technologies will make the measuring source used in this study literally obsolete.

7. Bibliography

Anandakrishnan, S. (2003). Dilatant till layer near the onset of streaming flow of Ice Stream C, West Antarctica, determined by AVO (amplitude vs offset) analysis. *Annals of Glaciology*, 36, 283-286.

Anwer, H. M., Alves, T. M., & Ali, A. (2017). Effects of sand-shale anisotropy on amplitude variation with angle (AVA) modelling: The Sawan gas field (Pakistan) as a key case-study for South Asia's sedimentary basins. *Journal of Asian Earth Sciences*, *147*, 516-531.

Benjumea, B., Macheret, Y. Y., Navarro, F. J., & Teixidó, T. (2003). Estimation of water content in a temperate glacier from radar and seismic sounding data. *Annals of Glaciology*, *37*, 317-324.

Best, A. I., Sothcott, J., & McCann, C. (2007). A laboratory study of seismic velocity and attenuation anisotropy in near-surface sedimentary rocks. *Geophysical Prospecting*, *55*(5), 609-625.

Bitri, A., Perrin, J. & Beauce A. (1996). Rapport du Bureau de Recherches Géologiques et Minières (BRGM). Dans Rap. BRGM R 39220, *La sismique réflexion haute résolution : principes et applications* (pp. 1-59). Orléans : BRGM.

Bouasse, H. (1927). Reflexion et refraction, seismes et sismographes, Delagrave, Paris, 72-89.

Bose, R. N., Dutta, N. P., & Lahiri, S. M. (1971). Refraction seismic investigation at Zemu glacier, Sikkim. J*ournal of Glaciology, 10*(58), 113-119.

Bradford, J. H., Nichols, J., Harper, J. T., & Meierbachtol, T. (2013). Compressional and EM wave velocity anisotropy in a temperate glacier due to basal crevasses, and implications for water content estimation. *Annals of Glaciology*, *54*(64), 168-178.

Brandt, R. E., & Warren, S. G. (1993). Solar-heating rates and temperature profiles in Antarctic snow and ice. *Journal of Glaciology*, *39*(131), 99-110.

Buteau, S., Fortier, R., Delisle, G., & Allard, M. (2004). Numerical simulation of the impacts of climate warming on a permafrost mound. *Permafrost and Periglacial Processes, 15*(1), 41-57.

Chichinina, T. I., Obolentseva, I. R., & Ronquillo-Jarillo, G. (2009). Anisotropy of seismic attenuation in fractured media: theory and ultrasonic experiment. Transport in Porous Media, 79(1), 1-14.

Christianson, K., Peters, L. E., Alley, R. B., Anandakrishnan, S., Jacobel, R. W., Riverman, K. L., ... & Keisling, B. A. (2014). Dilatant till facilitates ice-stream flow in northeast Greenland. *Earth and Planetary Science Letters*, *401*, 57-69.

Church, G., Bauder, A., Grab, M., Rabenstein, L., Singh, S., & Maurer, H. (2019). Detecting and characterising an englacial conduit network within a temperate Swiss glacier using active seismic, ground penetrating radar and borehole analysis. *Annals of Glaciology*, 1-13.

Clarke, T. S., & Echelmeyer, K. (1996). Seismic-reflection evidence for a deep subglacial trough beneath Jakobshavns Isbræ, West Greenland. *Journal of Glaciology, 42*(141), 219-232.

Clason, C., Mair, D. W., Burgess, D. O., & Nienow, P. W. (2012). Modelling the delivery of supraglacial meltwater to the ice/bed interface: application to southwest Devon Ice Cap, Nunavut, Canada. *Journal of Glaciology*, *58*(208), 361-374.

Consortium for Research in Elastic Wave Exploration Seismology – CREWES (2020). *About CREWES*. Available on: https://www.crewes.org/About_CREWES/ (consulted the February 3rd, 2020)

Cooper, M. G., Smith, L. C., Rennermalm, A. K., Miège, C., Ryan, J., Pitcher, L. H., ... & Muthyala, R. (2017). Near surface meltwater storage in low-density bare ice of the Greenland ice sheet ablation zone. *AGUFM*, *2017*, C13F-1011.

Cuffey, K. M., & Paterson, W. S. B. (2010). *The physics of glaciers*. Academic Press.

Dana, J. D., & Salisbury, E. (1944). *The Systems of Mineralogy of James Dwight Dana and Edward Salisbury Dana, Yale University, 1837-1892*. Wiley.

Diez, A., Eisen, O., Hofstede, C., Bohleber, P., & Polom, U. (2013). Joint interpretation of explosive and vibroseismic surveys on cold firn for the investigation of ice properties. *Annals of Glaciology, 54*(64), 201-210.

Diez, A., Eisen, O., Weikusat, I., Eichler, J., Hofstede, C., Bohleber, P., ... & Polom, U. (2014). Influence of ice crystal anisotropy on seismic velocity analysis. *Annals of Glaciology*, *55*(67), 97-106.

Doell, R. R., & Cox, A. (1962). Determination of the magnetic polarity of rock samples in the field. *US Geological Survey Research*, *450*, 105-8.

Dragoset, B. (2005). A historical reflection on reflections. *The Leading Edge, 24*(Supplement), S46-S71.

Duval, P. (1977). The role of the water content on the creep rate of polycrystalline ice. *IAHS Publ, 118*, 29-33.

Duval, P. (1979). Creep and recrystallization of polycrystalline ice. *Bulletin de Minéralogie, 102*(2), 80-85.

Duval, P., Ashby, M. F., & Anderman, I. (1983). Rate-controlling processes in the creep of polycrystalline ice. *The Journal of Physical Chemistry*, *87*(21), 4066-4074.

Egli, P. E., Lane, S. N. & Irving, J. (2020). *Characterization of ice marginal channels using 3D ground penetrating radar*. Unpublished article, University of Lausanne, Faculty of geosciences, Suisse.

Eiken, O., Degutsch, M., Riste, P., & Rød, K. (1989). Snowstreamer: An efficient tool in seismic acquisition. *First Break, 7*(9), 374-378.

Eisen, O., Hofstede, C., Miller, H., Kristoffersen, Y., Blenkner, R., Lambrecht, A., & Mayer, C. (2010). A new approach for exploring ice sheets and sub-ice geology. *EOS, Transactions american geophysical union, 91*(46), 429-430.

Eisen, O., Hofstede, C., Diez, A., Kristoffersen, Y., Lambrecht, A., Mayer, C., ... & Hilmarsson, S. (2015). On-ice vibroseis and snowstreamer systems for geoscientific research. *Polar Science, 9*(1), 51-65.

Feagin, F. J. (1981). Seismic data display and reflection perceptibility. *Geophysics*, *46*(2), 106-120.

Fountain, A. G., & Jacobel, R. W. (1997). Advances in ice radar studies of a temperate alpine glacier, South Cascade Glacier, Washington, USA. *Annals of Glaciology*, *24*, 303-308.

Fountain, A. G., & Walder, J. S. (1998). Water flow through temperate glaciers. *Reviews of Geophysics*, *36*(3), 299-328.

Fountain, A. G., Jacobel, R. W., Schlichting, R., & Jansson, P. (2005). Fractures as the main pathways of water flow in temperate glaciers. *Nature*, *433*(7026), 618-621.

Gabbud, C., & Lane, S. N. (2016). Ecosystem impacts of Alpine water intakes for hydropower: the challenge of sediment management. *Wiley Interdisciplinary Reviews: Water*, *3*(1), 41-61.

Gabbi, J., Farinotti, D., Bauder, A., & Maurer, H. (2012). Ice volume distribution and implications on runoff projections in a glacierized catchment. *Hydrology and Earth System Sciences, 16*(12), 4543–4556. https://doi.org/10.5194/hess-16-4543-2012

Geometrics. (2018). *Geode Exploration Seismograph*. Available on : https://www.geometrics.com/product/geode-exploration-seismograph/ (consulted the January 6th, 2020)

Geosym. (2019). *Seismic Vibrator Source ElViS*. Available on: http://www.geosym.de/geophysicalmeasurement-systems/seismic-vibrator-source-elvis/ (consulted the October 22nd, 2019)

Greve, R., & Blatter, H. (2009). *Dynamics of ice sheets and glaciers*. Springer Science & Business Media.

Gusmeroli, A., Murray, T., Barrett, B., Clark, R., & Booth, A. (2008). Estimates of water content in glacier ice using vertical radar profiles: A modified interpretation for the temperate glacier Falljökull, Iceland. *Journal of Glaciology*, *54*(188), 939-942.

Gusmeroli, A., Clark, R. A., Murray, T., Booth, A. D., Kulessa, B., & Barrett, B. E. (2010). Seismic wave attenuation in the uppermost glacier ice of Storglaciären, Sweden. *Journal of Glaciology, 56*(196), 249-256.

Gusmeroli, A., Murray, T., Clark, R. A., Kulessa, B., & Jansson, P. (2013). Vertical seismic profiling of glaciers: appraising multi-phase mixing models. *Annals of Glaciology*, *54*(64), 115-123.

Gutenberg, B., Wood, H. O., & Buwalda, J. P. (1932). Experiments testing seismographic methods for determining crustal structure. *Bulletin of the Seismological Society of America*, *22*(3), 185-246.Jeffreys, H. (1926). The reflexion and refraction of elastic waves. Geophysical Supplements to the Monthly Notices of the Royal Astronomical Society, 1(7), 321-334.

Gutenberg, B., & Richter, C. F. (1939). On seismic waves.

Halberstadt, A. R. W., Simkins, L. M., Anderson, J. B., Prothro, L. O., & Bart, P. J. (2018). Characteristics of the deforming bed: till properties on the deglaciated Antarctic continental shelf. *Journal of Glaciology*, *64*(248), 1014-1027.

Hameg, Z. B. (2007). *Nouvelles méthodes de séparation des champs d'ondes en sismique* (Doctoral dissertation).

Hamran, S., Aarholt, E., Hagen, J. O., & Mo, P. (1996). Estimation of relative water content in a sub-polar glacier using surface-penetration radar. *Journal of Glaciology*, *42*(142), 533-537.

Huang, H., Dennis, J. M., Wang, L., & Chen, P. (2013). A scalable parallel LSQR algorithm for solving large-scale linear system for tomographic problems: a case study in seismic tomography. *Procedia Computer Science*, *18*, 581-590.

Henry, G. (1997). *La sismique réflexion: principes et développements*. Editions Technip.

Herman, F., Beyssac, O., Brughelli, M., Lane, S. N., Leprince, S., Adatte, T., ... Cox, S. C. (2015). Erosion by an Alpine glacier. *Science, 350*(6257), 193–195. https://doi.org/10.1126/science .aab2386

Hilbich, C. (2010). Time-lapse refraction seismic tomography for the detection of ground ice degradation. *The Cryosphere*, *4*(3), 243.

Hobson, G. D. (1962). Seismic exploration in the Canadian Arctic islands. *Geophysics*, *27*(2), 253-273.

Hofstede, C., Eisen, O., Diez, A., Jansen, D., Kristoffersen, Y., Lambrecht, A., & Mayer, C. (2013). Investigating englacial reflections with vibro-and explosive-seismic surveys at Halvfarryggen ice dome, Antarctica. *Annals of Glaciology*, *54*(64), 189-200.

Hofstede, C., Christoffersen, P., Hubbard, B., Doyle, S. H., Young, T. J., Diez, A., ... & Hubbard, A. (2018). Physical conditions of fast glacier flow: 2. Variable extent of anisotropic ice and soft basal sediment from seismic reflection data acquired on Store Glacier, West Greenland. *Journal of Geophysical Research: Earth Surface*, *123*(2), 349-362.

Horgan, H. J., Anandakrishnan, S., Alley, R. B., Peters, L. E., Tsoflias, G. P., Voigt, D. E., & Winberry, J. P. (2008). Complex fabric development revealed by englacial seismic reflectivity: Jakobshavn Isbræ, Greenland. *Geophysical Research Letters*, *35*(10).

Huang, G., Zhou, B., Li, H., & Nobes, D. C. (2017). Seismic travel time inversion based on tomographic equation without integral terms. *Computers & Geosciences*, *104*, 29-34.

Hübscher, C., & Gohl, K. (2014). Reflection/Refraction seismology. Encycl. Mar. Geosciences.

Iken, A., Röthlisberger, H., Flotron, A., & Haeberli, W. (1983). The uplift of Unteraargletscher at the beginning of the melt season - a consequence of water storage at the bed? *Journal of Glaciology, 29*(101), 28-47. doi: 10.1017/S 0022143000005128.

Iverson, N. R. (2010). Shear resistance and continuity of subglacial till: hydrology rules. *Journal of Glaciology, 56*(200), 1104-1114.

Kearey, P., Brooks, M., & Hill, I. (2013). *An introduction to geophysical exploration*. John Wiley & Sons.

King, E. C., Smith, A. M., Murray, T., & Stuart, G. W. (2008). Glacier-bed characteristics of midtre Lovénbreen, Svalbard, from high-resolution seismic and radar surveying. *Journal of Glaciology*, *54*(184), 145-156.

Kirchner, J. F., & Bentley, C. R. (1979). Seismic short-refraction studies on the Ross Ice Shelf, Antarctica. *Journal of Glaciology*, *24*(90), 313-319.

Knott, C. G. (1899). III. Reflexion and refraction of elastic waves, with seismological applications. *The London, Edinburgh, and Dublin Philosophical Magazine and Journal of Science, 48*(290), 64-97.

Knott, C. G. (1920). XIV.—The Propagation of Earthquake Waves through the Earth and connected Problems. *Proceedings of the Royal Society of Edinburgh, 39*, 157-208.

Kohnen, H., & Bentley, C. R. (1973). Seismic refraction and reflection measurements at "Byrd" Station, Antarctica. *Journal of glaciology, 12*(64), 101-111.

Kohnen, H. (1974). The temperature dependence of seismic waves in ice. *Journal of Glaciology, 13*(67), 144-147.

Lane, S. N., Bakker, M., Gabbud, C., Micheletti, N., & Saugy, J. N. (2017). Sediment export, transient landscape response and catchment-scale connectivity following rapid climate warming and Alpine glacier recession. *Geomorphology*, 277, 210-227.

Lavergne, M. (1986). *Méthodes sismiques*. Editions Technip.

Liu, E. (2011). Seismic diffraction. *Encyclopedia of Solid Earth Geophysics. SpringerReference (www. springerreference. com). Springer, Berlin.*

Lumley, E. M., & Bowman, B. F. (1987). *Automatic gain control for seismic data* (No. US 4636993).

Machguth, H., Paul, F., Hoelzle, M., & Haeberli, W. (2006). Distributed glacier mass-balance modelling as an important component of modern multi-level glacier monitoring. *Annals of glaciology*, *43*, 335-343.

Magnin, O., & Bertrand, Y. (2005). Guide Sismique Réfraction. *Laboratoire Centrale des ponts et chaussées.*

Margrave, G. F. (2001). Numerical methods of exploration seismology with algorithms in Matlab: The University of Calgary.

Mari, J.-L. (2002). *Sismique de puits – Cours online de géophysique* (PDF). University of Lausanne, Institute of Geography, Switzerland.

McNaught, A. D. (1997). *Compendium of chemical terminology* (Vol. 1669). Oxford: Blackwell Science.

Meyer, C. R., Fernandes, M. C., Creyts, T. T., & Rice, J. R. (2016). Effects of ice deformation on Röthlisberger channels and implications for transitions in subglacial hydrology. *Journal of Glaciology, 62*(234), 750-762.

Mo, L. W., & Harris, J. M. (2002). Finite-difference calculation of direct-arrival travel times using the eikonal equation. *Geophysics, 67*(4), 1270-1274.

Mousa, W. A., & Al-Shuhail, A. A. (2011). Processing of seismic reflection data using MATLAB™. *Synthesis Lectures on Signal Processing, 5*(1), 1-97.

Murray, W. A. (1972). Numerical methods for unconstrained optimization.

Murray, T., Stuart, G. W., Fry, M., Gamble, N. H., & Crabtree, M. D. (2000). Englacial water distribution in a temperate glacier from surface and borehole radar velocity analysis. *Journal of Glaciology, 46*(154), 389-398.

Murray, T., Booth, A., & Rippin, D. M. (2007). Water-content of glacier-ice: limitations on estimates from velocity analysis of surface ground-penetrating radar surveys. *Journal of Environmental & Engineering Geophysics, 12*(1), 87-99.

Navarro, F. J., Macheret, Y. Y., & Benjumea, B. (2005). Application of radar and seismic methods for the investigation of temperate glaciers. *Journal of Applied Geophysics, 57*(3), 193-211.

NCCS (éd.) 2018 : CH2018 - scénarios climatiques pour la Suisse. National Centre for Climate Services, Zurich. 24 pages. Numéro ISBN 978-3-9525031-1-9.

Nolan, M., & Echelmeyer, K. (1999). Seismic detection of transient changes beneath Black Rapids Glacier, Alaska, USA: I. Techniques and observations. *Journal of Glaciology, 45*(149), 119-131.

Nowack, R. L. (1992). Wavefronts and solutions of the eikonal equation. *Geophysical Journal International, 110*(1), 55-62.

Onajite, E. (2013). *Seismic data analysis techniques in hydrocarbon exploration*. Elsevier.

Paterson, W. S. B. (1981). The physics of glaciers Second edition.

Perolo, P., Bakker, M., Gabbud, C., Moradi, G., Rennie, C., & Lane, S. N. (2019). Subglacial sediment production and snout marginal ice uplift during the late ablation season of a temperate valley glacier. *Earth Surface Processes and Landforms*.

Peters, L. E., Anandakrishnan, S., Alley, R. B., & Voigt, D. E. (2012). Seismic attenuation in glacial ice: A proxy for englacial temperature. Journal of Geophysical Research: Earth Surface, 117(F2).

Podolskiy, E. A., & Walter, F. (2016). Cryoseismology. *Reviews of geophysics, 54*(4), 708-758.

Pohjola, V. A. (1994). TV-video observations of englacial voids in Storglaciären, Sweden. *Journal of Glaciology, 40*(135), 231-240.

Polom, U., Hofstede, C., Diez, A., & Eisen, O. (2014). First glacier-vibroseismic experiment–results from cold firn of Colle Gnifetti. *Near Surface Geophysics*, *12*(4), 493-504.

Raymond, C. F., & Harrison, W. D. (1975). Some observations on the behavior of the liquid and gas phases in temperate glacier ice. *Journal of Glaciology*, *14*(71), 213-233.

Richards, M. A. (1988). Seismic evidence for a weak basal layer during the 1982 surge of Variegated Glacier, Alaska, USA. *Journal of Glaciology*, *34*(116), 111-120.

Rigsby, G. P. (1960). Crystal orientation in glacier and in experimentally deformed ice. *Journal of Glaciology*, *3*(27), 589-606.

Robertson, J. D., & Bentley, C. R. (1990). Seismic studies on the grid western half of the Ross Ice Shelf: RIGGS I and RIGGS II. *The Ross Ice Shelf: Glaciology and Geophysics*, *42*, 55-86.

Robin, S., & Vodar, B. (1953). Solubility in compressed gases. *Discussions of the Faraday Society*, *15*, 233-238.

Rocks.comparenature.com. (2015). *Compare rocks*. Available on: https://rocks.comparenature .com (consulted the May 26th, 2019)

Roden, R. (2005). The evolution of the interpreter's toolkit – past, present, and future. *The Leading Edge*, *24*, 72–78.

Röthlisberger, H. (1955). Studies on glacier physics on the penny ice cap, Baffin Island, 1953, part III: seismic soundings. *Journal of Glaciology, 18*, 539-552.

Röthlisberger, H. (1972). Water pressure in intra-and subglacial channels. *Journal of Glaciology, 11*(62), 177-203.

Sala, M. (2019). *Le potentiel du Ground Penetrating Radar en trois dimensions pour l'étude des structures sous-glaciaires d'un glacier alpin tempéré* (Unpublished master thesis). University of Lausanne, Faculty of geosciences, Suisse.

Scapozza, C., Lambiel, C., Gex, P., & Reynard, E. (2011). Prospection géophysique multi-méthodes du pergélisol alpin dans le sud des Alpes suisses. *Géomorphologie: relief, processus, environnement, 17*(1), 15-32.

Schlegel, R., Diez, A., Löwe, H., Mayer, C., Lambrecht, A., Freitag, J., ... & Eisen, O. (2019). Comparison of elastic moduli from seismic diving-wave and ice-core microstructure analysis in Antarctic polar firn. *Annals of Glaciology*, *60*(79), 220-230.

Senkaya, M., & Karsli, H. (2011, October). First arrival picking in seismic refraction data by cross-corelation technique. In *6th Congress of the Balkan Geophysical Society* (pp. cp-262). European Association of Geoscientists & Engineers.

Shan, T. J., & Kailath, T. (1988). Adaptive algorithms with an automatic gain control feature. *IEEE Transactions on circuits and systems, 35*(1), 122-127.

Shanno, D. F. (1970). Conditioning of quasi-Newton methods for function minimization. *Mathematics of computation*, *24*(111), 647-656.

Sicart, J. E., Hock, R., & Six, D. (2008). Glacier melt, air temperature, and energy balance in different climates: The Bolivian Tropics, the French Alps, and northern Sweden. *Journal of Geophysical Research: Atmospheres*, *113*(D24).

Sieberg, A. H., & Gutenberg, B. (1923). Geologische, physikalische und angewandte Erdbebenkunde. G. Fischer.

Smith, E. C., Diez, A., Eisen, O., Hofstede, C., & Kohler, J. (2020, May 4-8). *Basal conditions of Kongsvegen at the onset of surge - revealed using seismic vibroseis surveys* [webpage presentation]. EGU General Assembly 2020: Session CR1.2, online. https://doi.org/10.5194/egusphere-egu2020-7185.

Stevens, I. T., Irvine-Fynn, T. D., Porter, P. R., Cook, J. M., Edwards, A., Smart, M., ... & Mitchell, A. C. (2018). Near-surface hydraulic conductivity of northern hemisphere glaciers. *Hydrological Processes*, *32*(7), 850-865.

Tarantola, A. (2005). *Inverse problem theory and methods for model parameter estimation*. Society for Industrial and Applied Mathematics.

Thorsteinsson, T., & Raymond, C. F. (2000). Sliding versus till deformation in the fast motion of an ice stream over a viscous till. *Journal of Glaciology, 46*(155), 633-640.

Thyssen, F. (1968). Determination of temperature on ice caps by seismic methods. *Journal of Glaciology, 7*(50), 333-335.

Truffer, M., Echelmeyer, K. A., & Harrison, W. D. (2001). Implications of till deformation on glacier dynamics. *Journal of Glaciology, 47*(156), 123-134.

Turrin, J., Forster, R., Sauber, J., Hall, D. K., & Bruhn, R. (2013). Effects of Bedrock Lithology and Subglacial Till on the Motion of Ruth Glacier, Alaska, Deduced from Five Pulses from 1973-2012.

VanWormer, D., & Berg, E. (1973). Seismic evidence for glacier motion. *Journal of Glaciology*, *12*(65), 259-265

Verney, P. (2009). *Interprétation géologique de données sismiques par une méthode supervisée basée sur la vision cognitive* (Doctoral dissertation).

Walter, F., Gräff, D., Lindner, F., Paitz, P., Köpfli, M., Chmiel, M., & Fichtner, A. (2020). Distributed Acoustic Sensing of Microseismic Sources and Wave Propagation in Glaciated Terrain.

Weisstein, E. W. (2004). Jacobian Conjecture. Available on: *https://mathworld. wolfram.com/ (*consulted the December 3rd, 2020)

Widess, M. B. (1973). How thin is a thin bed? *Geophysics, 38*(6), 1176–1180.

Wiechert, E. (1920). Die Gravitation als elektrodynamische Erscheinung. *Annalen der Physik, 368*(20), 301-381.

Xie, C. G. (2015). Applications of tomography in oil-gas industry–Part 1. In *Industrial Tomography* (pp. 591-632). Woodhead Publishing.

Yilamz, O. (2001). Seismic data analysis. Processing, inversion and interpretation of seismic data, volumes 1 and 2. Society of Exploration Geophysics, Tulsa, OK.

Young Kim, K., Lee, J., Ho Hong, M., Kuk Hong, J., Keun Jin, Y., & Shon, H. (2010). Seismic and radar investigations of Fourcade Glacier on King George Island, Antarctica. *Polar Research, 29*(3), 298-310.

Zechmann, J. M., Booth, A. D., Truffer, M., Gusmeroli, A., Amundson, J. M., & Larsen, C. F. (2018). Active seismic studies in valley glacier settings: strategies and limitations. *Journal of Glaciology, 64*(247), 796-810.

Zhang, J., ten Brink, U. S., & Toksöz, M. N. (1998). Nonlinear refraction and reflection travel time tomography. *Journal of Geophysical Research: Solid Earth*, *103*(B12), 29743-29757.

8. Appendix

Appendix 1. Evolution of the Glacier d'Otemma

Tracing what the Glacier d'Otemma probably represented at (A) the Little Ice Age (LIA) end, in the middle of the 19th century, via 1855 Dufour Map; (B) the beginning of the 20th century, via Siegfried Map 1899; (C) the middle of the 20th century; (D) between 1970 – 1980; (E) around the 2000s; (F) currently. The national map proposed by Swisstopo© in digital form was used to make this image. Contours of the Glacier d'Otemma represented on the map were used to be transcribed approximately on this satellite image.
Source : *Google Earth© (background), 2013; Swisstopo© (content), 2013 - October 26, 2017.*

	Ablation rod (cm) - Otemma July 2019								
Rod n°	18.07	19.07	21.07	23.07	25.07	27.07	29.07	**Ave/day**	**Tot. ave.**
4.1	76.3	83.5	99.3	119	131.8	146.9	163.2	**7.6**	
4.2	78.1	84	96.2	116.4	129.5	142.5	155	**6.9**	
4.3	98	105.4	115.5	134.2	146.4	158.2	164.5	**6.2**	
4.4	76.5	84.1	95.7	117.4	130.2	145.4	160.1	**7.4**	
4.5	102.2	109.5	123.4	146.8	159.5	175.3	186.4	**7.4**	
4.6	73.1	80.1	92.3	108.2	121.4	136.3	147.9	**6.8**	**7.0**
4.8	102.9	111.2	124.6	144.1	158.2	172.3	182.5	**7.3**	
4.9	106.2	112.5	125.6	140.9	152.8	166.2	183.8	**6.8**	
4.10	105.2	109.5	121.5	141.2	156.7	172.3	180.1	**6.8**	
4.11	114.2	120.7	134.7	158.1	173.2	189.7	189.7	**6.9**	
7.12	79.8	86.9	100.4	122.4	136.5	151.2	162.4	**7.4**	

	Ablation rod (cm) - Otemma August 2019									
Rod n°	29.07	01.08	03.08	05.08	07.08	10.08	13.08	15.08	17.08	**Ave/day**	**Tot. ave.**
4.1	32.2	45.4	64.9	84.6	94.2	118.2	130.1	142.3	150.5	**5.9**	
4.2	26.6	38.6	62.1	74.7	88.3	108.8	123.1	133.3	146.1	**6.0**	
4.3	58.9	76.4	88	98.4	117.6	131.4	143.1	153.5	161.2	**5.1**	
4.4	28.5	48.3	62.1	75.8	94.8	114.6	130.7	144.2	162.6	**6.7**	
4.5	58.8	78.9	94.8	100.1	122	143.7	152.2	159.6	166.8	**5.2**	
4.6	29.7	38.3	62.6	72.2	87.4	104.3	115.1	125.1	132.6	**5.2**	**5.7**
4.8	58.1	88	95.6	106.8	127.2	145.9	160.3	173.2	186.4	**6.2**	
4.9	55.9	87.1	91.6	101.2	124.6	147.1	160	170.2	182.5	**6.0**	
4.10	55.9	75.4	87.1	97.4	108.3	129	145.6	153.6	164.4	**5.3**	
4.11	92.7	127.7	135.6	143.1	158.4	178.3	193.5	200.6		**5.6**	
7.12	56.1	80.2	89.8	98.7	113.2	135.4	152.7	162.1		**5.7**	

*Appendix 2. **Ablation measurements on the Glacier d'Otemma in July and August 2019.***
Measurements results made on the Glacier d'Otemma (in cm), by stem, from the glacier surface, via a metal plate to standardize measurements, at the upper end of the stem. The daily average per stem (Ave/day) and the total daily average (Tot. ave.) are also calculated for July (11 days) and August (19 days). Over measurement 30 days, the surface melting of the Glacier d'Otemma was about 1.85m. The ablation measurements were carried out at sites 10 and 9.
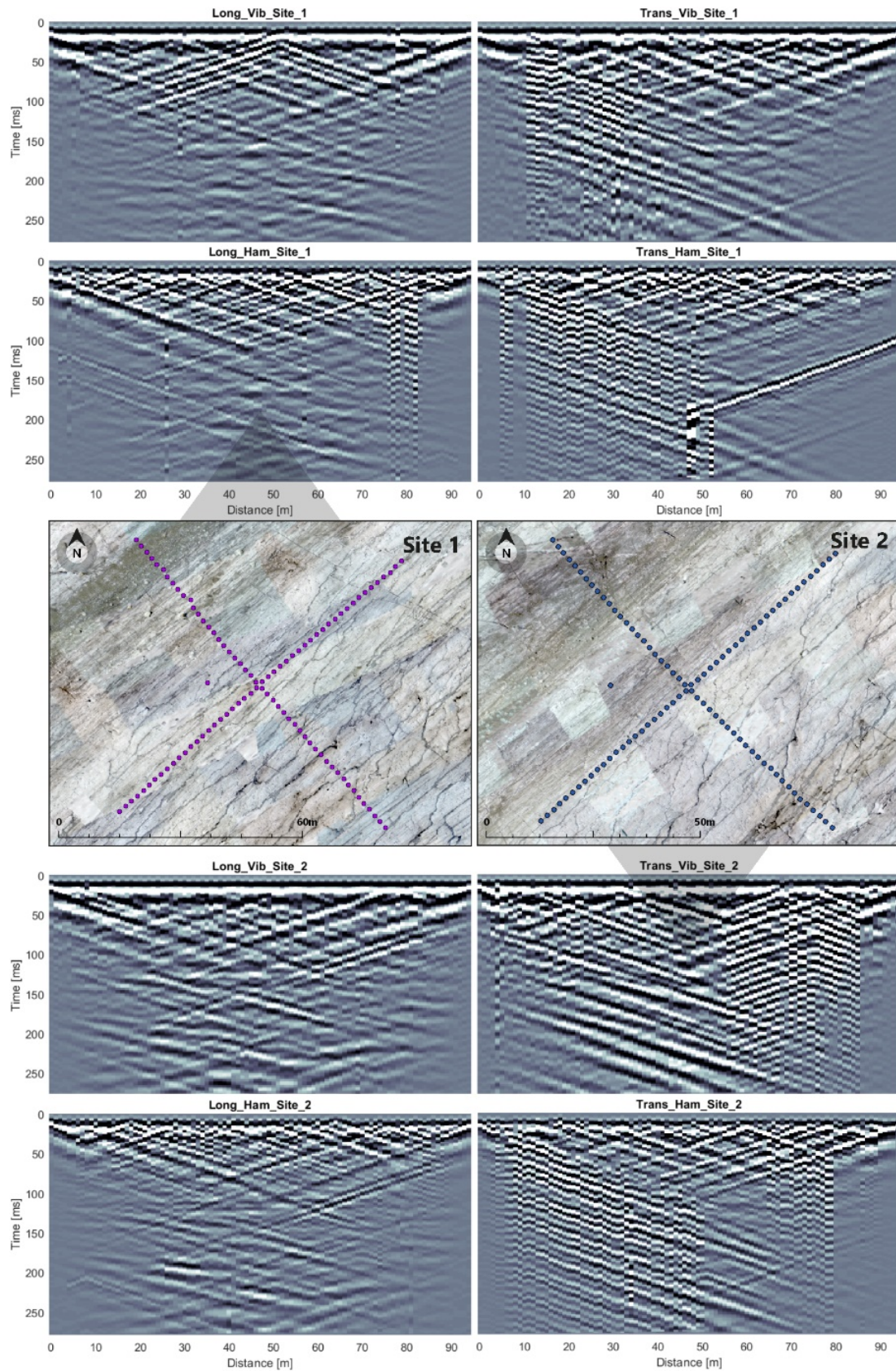
Appendix 3. CDPs stacking from the site 1 (upwards) and the site 2 (below) data set
Transversal (Trans_), as well as longitudinal (Long_) seismic profiles representation, between ElViS (Vib_) and sledgehammer (Ham_), with 3300 m/s NMO velocity. The CDPs stacks is the relationship between time (ms) and the distance (m). A DEM at the analysed site level is proposed in order to have a view of the site situation in the field and the surface glaciological forms that can be observed, but also interfere in the measurements.
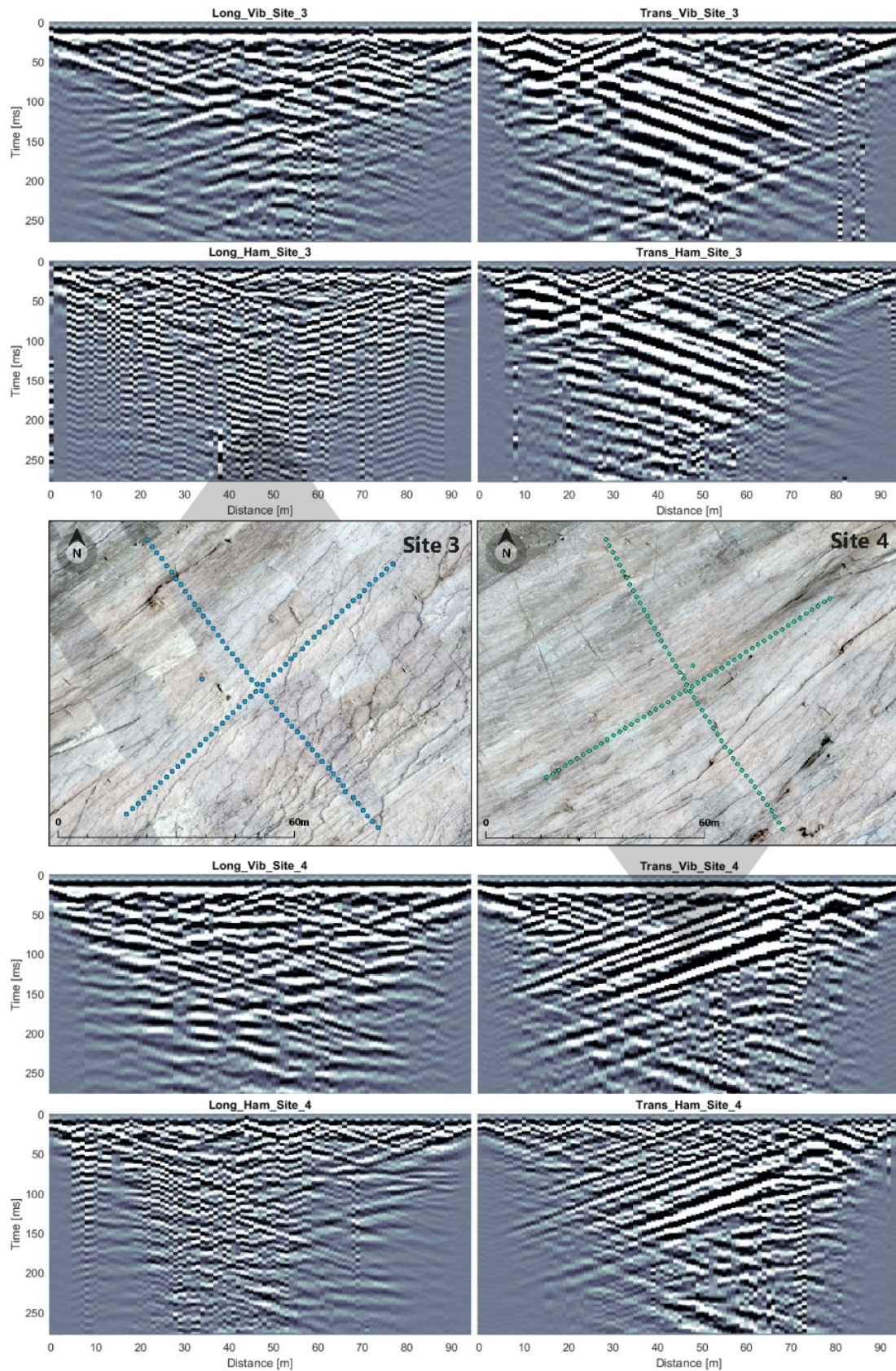
Appendix 4. CDPs stacking from the site 3 (upwards) and the site 4 (below) data set
*Transversal (Trans_), as well as longitudinal (Long_) seismic profiles representation, between ElViS (Vib_) and sledgehammer (Ham_),
with 3300 m/s NMO velocity. The CDPs stacks is the relationship between time (ms) and the distance (m). A DEM at the analysed site
level is proposed in order to have a view of the site situation in the field and the surface glaciological forms that can be observed, but
also interfere in the measurements.*
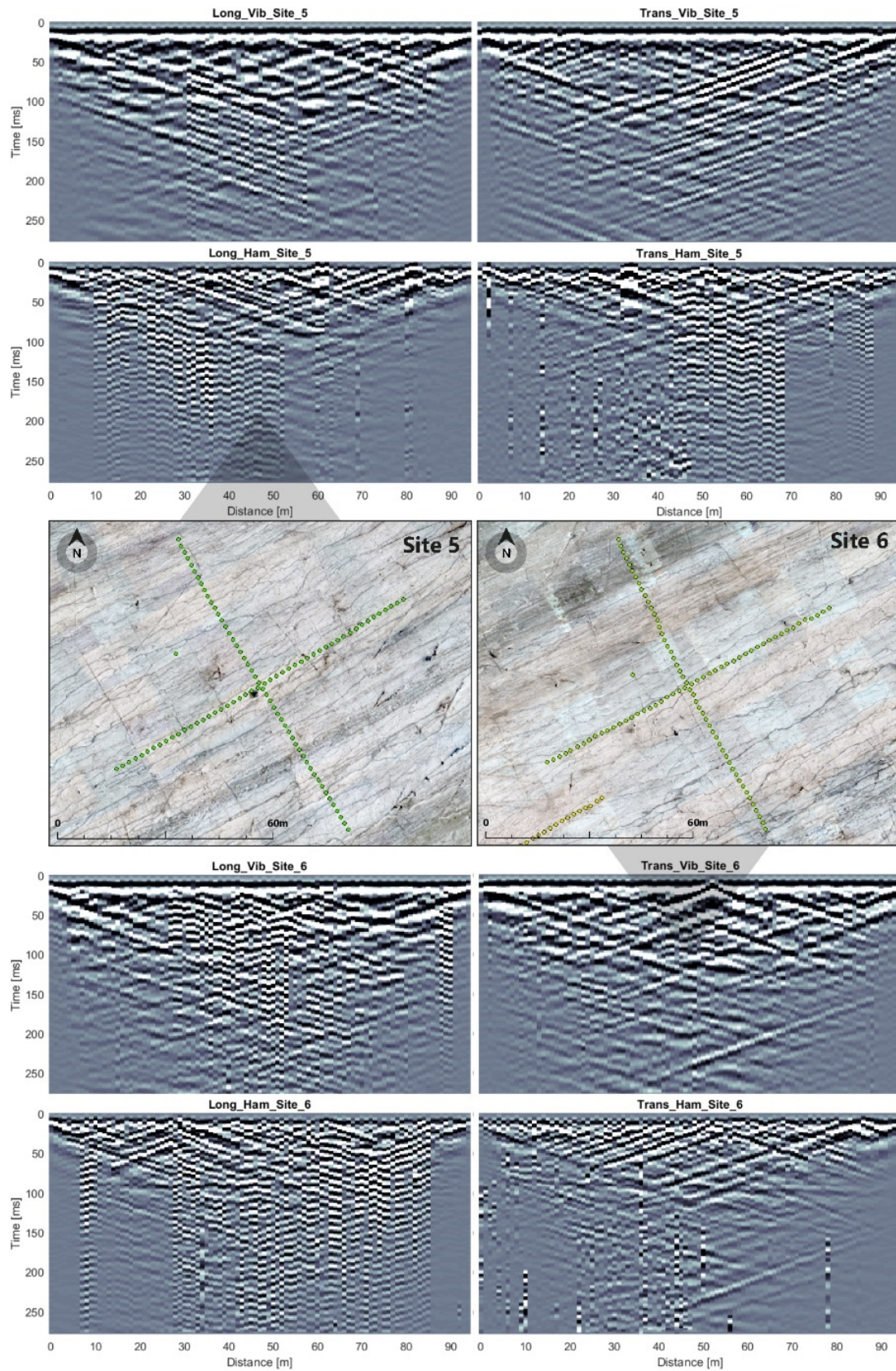
Appendix 5. CDPs stacking from the site 5 (upwards) and the site 6 (below) data set

Transversal (Trans_), as well as longitudinal (Long_) seismic profiles representation, between ElViS (Vib_) and sledgehammer (Ham_), with 3300 m/s NMO velocity. The CDPs stacks is the relationship between time (ms) and the distance (m). A DEM at the analysed site level is proposed in order to have a view of the site situation in the field and the surface glaciological forms that can be observed, but also interfere in the measurements.
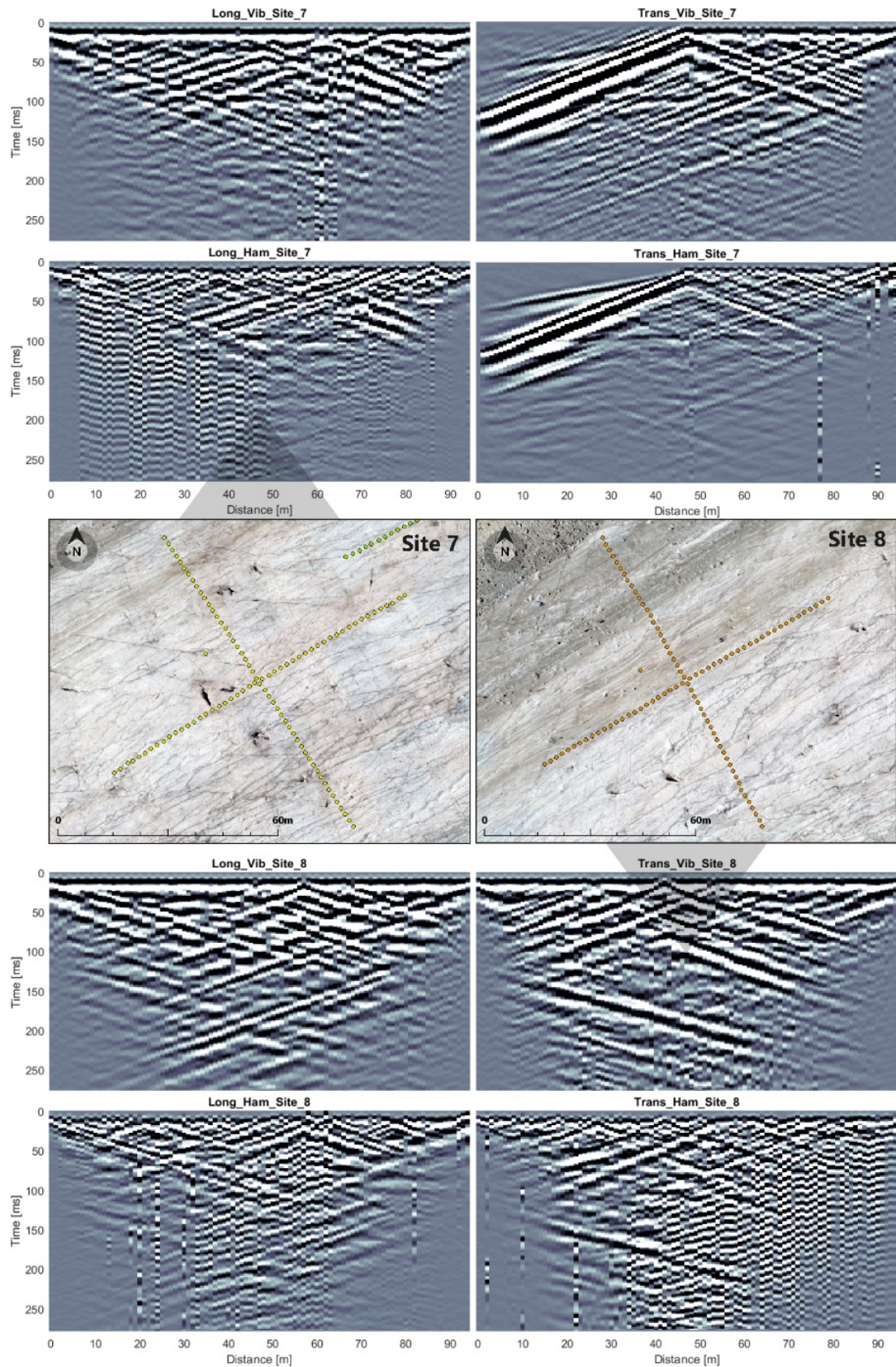
Appendix 6. CDPs stacking from the site 7 (upwards) and the site 8 (below) data set
Transversal (Trans_), as well as longitudinal (Long_) seismic profiles representation, between ElViS (Vib_) and sledgehammer (Ham_), with 3300 m/s NMO velocity. The CDPs stacks is the relationship between time (ms) and the distance (m). A DEM at the analysed site level is proposed in order to have a view of the site situation in the field and the surface glaciological forms that can be observed, but also interfere in the measurements. Please note a technical malfunction for site 7, which makes this site unusable.
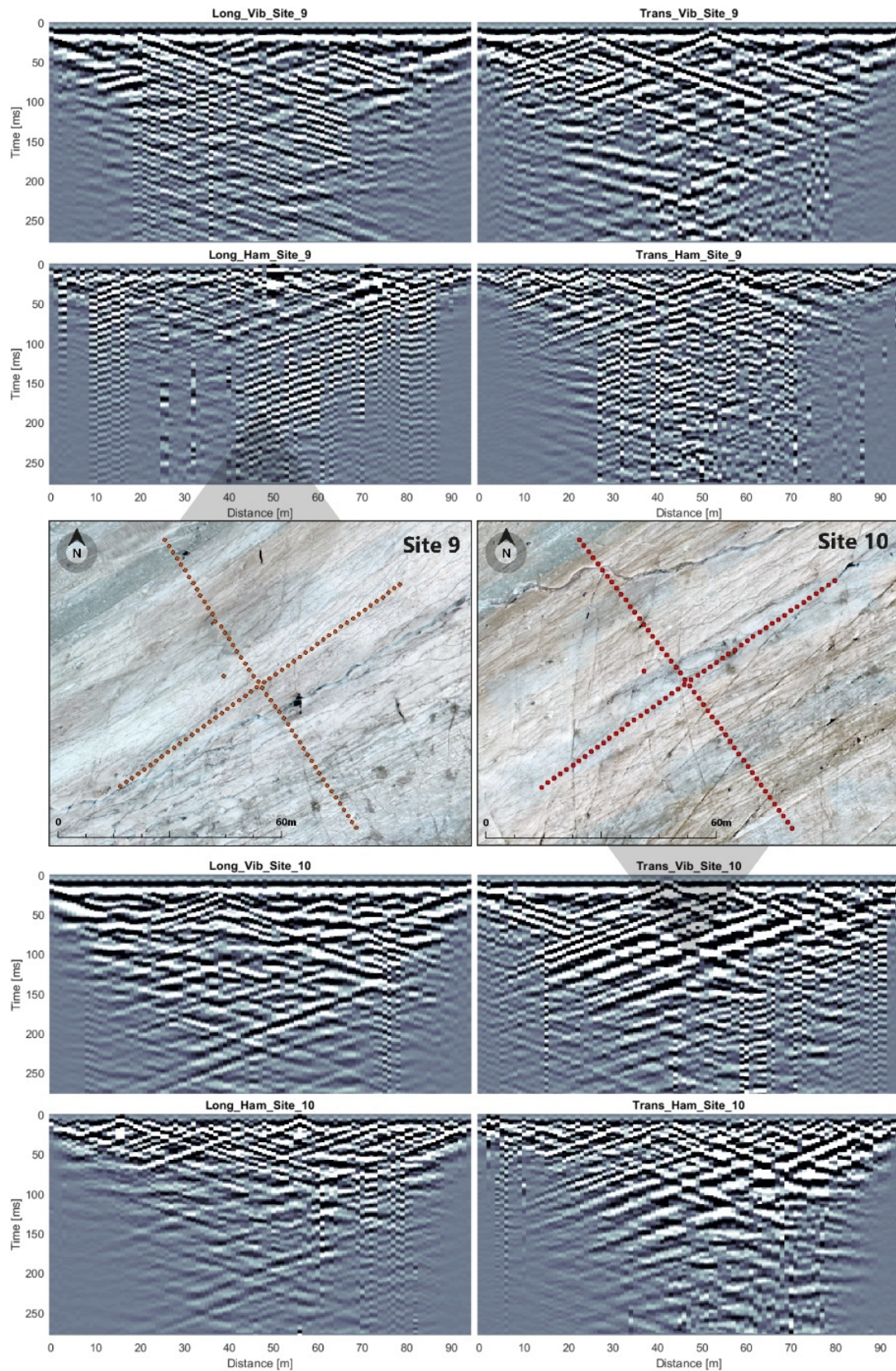
Appendix 7. CDPs stacking from the site 9 (upwards) and the site 10 (below) data set

Transversal (Trans_), as well as longitudinal (Long_) seismic profiles representation, between ElViS (Vib_) and sledgehammer (Ham_), with 3300 m/s NMO velocity. The CDPs stacks is the relationship between time (ms) and the distance (m). A DEM at the analysed site level is proposed in order to have a view of the site situation in the field and the surface glaciological forms that can be observed, but also interfere in the measurements.